

**Strong light-matter interactions and nonlinear
dynamics in coherently-driven optical
resonators**

Ph.D. Thesis, University of Amsterdam, June 2022

Strong light-matter interactions and nonlinear dynamics in coherently-driven optical resonators

Zhoumuyan Geng

The work described in this thesis was performed at
AMOLF, Science Park 104, 1098XG, Amsterdam, The Netherlands.

This work is part of the Netherlands Organization for Scientific Research (NWO).

A digital version of this thesis can be downloaded from
<http://amolf.nl>

Strong light-matter interactions and nonlinear dynamics in coherently-driven optical resonators

ACADEMISCH PROEFSCHRIFT

ter verkrijging van de graad van doctor
aan de Universiteit van Amsterdam
op gezag van de Rector Magnificus
prof. dr. ir. K.I.J. Maex
ten overstaan van een door het College voor Promoties ingestelde commissie,
in het openbaar te verdedigen in de Agnietenkapel
op donderdag 2 juni 2022, te 16.00 uur

door

Zhoumuyan Geng

geboren te Henan

Promotiecommissie

Promotor: prof. dr. A. F. Koenderink Universiteit van Amsterdam

Copromotor: dr. S. R. K. Rodriguez AMOLF

Overige leden: prof. dr. E.C. Garnett Universiteit van Amsterdam
dr. J. van de Groep Universiteit van Amsterdam
prof. dr. F.E. Schreck Universiteit van Amsterdam
prof. dr. W.L. Barnes University of Exeter
dr. J.A. Klärs Universiteit Twente

Faculteit der Natuurwetenschappen, Wiskunde en Informatica

Contents

| | | |
|----------|---|-----------|
| 1 | Introduction | 7 |
| 1.1 | Motivation | 7 |
| 1.2 | Optical bistability of a single-mode nonlinear cavity | 10 |
| 1.2.1 | Steady-state analysis | 11 |
| 1.3 | Approaches to realize optical nonlinearity and bistability | 13 |
| 1.4 | Overview of this thesis | 15 |
| 2 | Universal scaling of the dynamic optical hysteresis of a tunable cavity with non-instantaneous nonlinearity | 17 |
| 2.1 | Introduction | 18 |
| 2.2 | Experimental setup | 19 |
| 2.3 | Optical bistability and steady-state analysis | 20 |
| 2.4 | Dynamic hysteresis with non-instantaneous nonlinearity | 22 |
| 2.5 | Universal scaling of the dynamic hysteresis area | 25 |
| 2.6 | Memory effects due to the thermo-optical nonlinearity | 26 |
| 2.7 | Conclusion | 27 |
| 2.8 | Appendices | 28 |
| 2.8.1 | Temperature rise in the oil-filled cavity | 28 |
| 2.8.2 | Calculation details | 30 |
| 2.8.3 | Residence time analysis | 32 |
| 2.8.4 | Dynamic hysteresis influenced by fluctuations | 33 |
| 3 | Observation of optical bistability and spontaneous symmetry breaking in a plasmonic grating inside a nonlinear waveguide | 35 |
| 3.1 | Introduction | 36 |
| 3.2 | Sample and linear response | 37 |
| 3.3 | Laser diffraction measurements in the linear regime | 40 |
| 3.4 | Setup for measuring intensity-dependent transmission and diffraction | 44 |
| 3.5 | Optical bistability and emergent spatial patterns | 45 |
| 3.6 | Dynamics of (a)symmetric diffraction efficiency of a nonlinear grating | 49 |
| 3.7 | Spontaneous oscillations | 55 |
| 3.8 | Conclusion | 58 |
| 3.9 | Appendices | 60 |
| 3.9.1 | Details on the algorithm for calculating cross- and auto-correlation functions | 60 |

| | |
|---|------------|
| 4 Fano lineshapes and mode splittings: Can they be artificially generated or obscured by the numerical aperture? | 61 |
| 4.1 Introduction | 62 |
| 4.1.1 Exciton-polaritons in a cavity with CsPbBr ₃ | 62 |
| 4.1.2 Fano resonance and Rabi splitting | 62 |
| 4.2 Artificially generated Fano lineshape and Rabi splitting by a moderately large <i>NA</i> | 63 |
| 4.3 Empty cavity transmittance measurements and transfer matrix calculations | 67 |
| 4.4 Obscured Rabi splitting by a moderately large <i>NA</i> | 69 |
| 4.5 Conclusion | 72 |
| 4.6 Appendices | 73 |
| 4.6.1 Details on transfer matrix calculation | 73 |
| 5 Open access tunable cavity in a closed-cycle cryostat | 75 |
| 5.1 Introduction | 76 |
| 5.2 Open-access tunable cavity in a closed-cycle cryostat | 78 |
| 5.3 Characterization of the cavity mechanical stability | 80 |
| 5.3.1 Approach | 80 |
| 5.3.2 Results | 81 |
| 5.3.3 Transmittance measurement of a CsPbBr ₃ -cavity system at cryogenic temperature | 85 |
| 5.4 Optical bistability in a cavity with CsPbBr ₃ at cryogenic temperature . | 86 |
| 5.5 Conclusion | 88 |
| Summary | 111 |
| Samenvatting | 113 |
| List of Publications | 115 |

Chapter 1

Introduction

1.1 Motivation

The manipulation of light, and electromagnetic waves in general, is key to many information and communication technologies. However, the absence of mutual interactions between photons in linear systems [1] limits the type of operations one can perform with light. For instance, in the absence of photon-photon interactions one cannot steer or route light using light. To overcome this and related issues, and broaden the class of operations that can be achieved with light, nonlinear optical media are required [1–7]. Such media can mediate effective photon-photon interactions and thereby enable light-by-light control. Nonetheless, realizing nonlinear effects is challenging because nonlinear light-matter interactions are weak in most materials [8–12].

One way to enhance light-matter interactions is to confine light within an optical microcavity [13–18]. The enhanced spatial overlap between light and the intra-cavity matter, combined with a longer interaction time due to the storage of light in the cavity, can reduce the power threshold for observing nonlinear optical effects. The particular nonlinear effect we are concerned with in this thesis is an intensity-dependent refractive index. This effect is sometimes called the “Kerr effect”, or “Kerr nonlinearity” [2]. However, we note that in the literature, the term “Kerr nonlinearity” is sometimes reserved for situations where the nonlinear response is of electronic origin and is effectively instantaneous. This contrasts with, for example, situations where an intensity-dependent refractive index emerges from a slow (e.g., thermal) process. With this distinction in mind and for simplicity, in the rest of this introduction chapter we will refer to all nonlinearities associated with an intensity-dependent refractive index as a “Kerr-type nonlinearity” regardless of their physical origins.

Optical cavities with Kerr-type nonlinearities have become a subject of great interest in both experimental and theoretical physics since the 1970s [19, 20]. Kerr-type

nonlinearities have been studied in planar cavities [21–26], single-mode cavities [27–37], cavity arrays [38–42], and fiber cavities [43, 44]. The simplest of these systems is the single-mode Kerr nonlinear cavity. We will therefore focus on this system in this introduction chapter.

Within a classical framework, the main and most-widely studied feature of single-mode cavities with Kerr-type nonlinearity is optical bistability: two stable steady states at a single driving condition [45]. Bistable optical cavities have been proposed to realize all-optical switching [46–51], flip-flop memories [52–54], and as building blocks for logic gates [55–59]. However, it has been challenging to make (and even more so to cascade) such devices in an energy-efficient, compact, and reliable manner [60]. Within a quantum framework, single-mode Kerr nonlinear cavities (with a strong focus on electronic Kerr-type nonlinearities) have also drawn great interest [29, 35–37, 61, 62]. If the Kerr nonlinearity is strong at the single-photon level, such a cavity can transform coherent light (i.e., a laser) into a single-photon source via the photon blockade effect [1, 36, 37, 63].

Beyond their fundamental physics relevance, single-mode Kerr nonlinear cavities are also relevant because they are the building blocks of cavity arrays. Such nonlinear cavity arrays have recently drawn attention as platforms for quantum simulation or emulation [1, 64, 65], i.e., simulating or emulating the behavior of complex quantum systems using a more controllable system in the lab. For instance, nonlinear cavity arrays have been proposed/fabricated to simulate the physics of the Bose-Hubbard model [66–69] and various spin models [70–73]. Furthermore, applications of cavity arrays with Kerr-type nonlinearity have also been proposed. For instance, such an array can be used to solve hard optimization problems [42]. This approach relies on the mapping of an array of bistable optical cavities to an Ising model [41], which in turn can be mapped to a wide range of optimization problems [74]. Alternatively, nonlinear cavity arrays can also be used for all-optical neuromorphic computing [75].

In view of the above exciting ideas and developments, this thesis aims to further develop and deepen our understanding of optical cavities, or resonators in general, containing materials with Kerr-type nonlinearities. The most commonly used optical systems in this context are monolithic semiconductor cavities [22–25, 27, 38, 39, 76–79]. Despite the tremendous success of such cavities, and the fact that they can be more amenable for some technological applications by virtue of being ‘on-chip’, they have their drawbacks. The most obvious drawback is that they generally lack (or have a very limited) spectral tunability. The more subtle and important drawback, especially in these times when new materials are constantly being discovered, is that it is often difficult (if not impossible) to integrate new materials in the monolithic cavity. For monolithic semiconductor samples, lattice matching constraints and fabrication procedures prevent integration of the vast majority of materials once the mirror materials have been defined. This is a major obstacle in the road towards realizing optical cavities with stronger, or new types of, nonlinearities. Therefore, in this thesis we choose to mostly work with open-access tunable cavities which can incorporate any material inside [36, 37, 80–91].

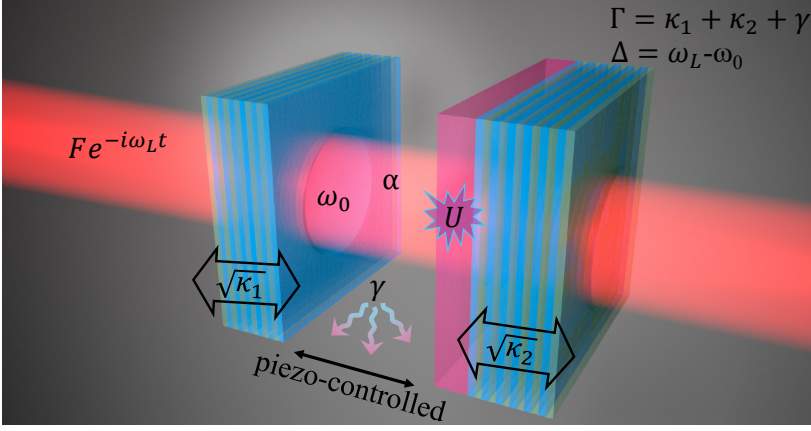


Figure 1.1: Schematic of an open-access tunable cavity. The cavity is made of one concave and one planar distributed Bragg reflector (DBR). The Kerr nonlinearity is provided by the material (red layer) attached to the planar mirror. Each mirror is mounted on a piezoelectric actuator for alignment and controlling the cavity length. Typically, we probe nonlinear effects in this system via resonant excitation with a continuous-wave laser (red beam). All shown symbols correspond to the model discussed in Section 1.2.

Figure 1.1 shows a schematic of the typical experimental setup used in this thesis: a Fabry–Pérot cavity made of one concave and one planar distributed Bragg reflector (DBR). The concave mirrors used in this thesis have been fabricated in the group of Jason Smith at the University of Oxford, using focused-ion beam milling as described in Ref. [92]. Meanwhile, the DBR coatings were all outsourced to an external company (LAYERTEC GmbH). In this system, the nonlinear response is due to a thin material layer attached to the planar DBR. The two mirrors are mounted on piezoelectric actuators, allowing to scan the cavity length at wish. Thanks to the high mirror reflectivity and the curvature of the concave mirror, optical modes are confined in three dimensions. Moreover, their frequency separation can be much larger than the linewidths, thereby allowing us to probe a single optical mode across a relatively large range of cavity lengths. In the next section, we introduce the model for such a single-mode cavity with Kerr-type nonlinearity. In the section after, we describe the approaches used in this thesis to obtain Kerr-type nonlinearity. Finally, we give an outline for this thesis.

1.2 Optical bistability of a single-mode nonlinear cavity

Within a classical framework, the light field α in a single-mode cavity with Kerr-type nonlinearity, driven by a coherent field with frequency ω_L and amplitude F , satisfies the following equation:

$$i\dot{\alpha} = \left(-\Delta - i\frac{\Gamma}{2} + U|\alpha|^2 \right) \alpha + i\sqrt{\kappa_1}F. \quad (1.1)$$

Equation (1.1) is written in a frame rotating at the driving frequency ω_L . Therefore, the relevant frequency is given by the laser-cavity detuning $\Delta = \omega_L - \omega_0$. $\Gamma = \gamma + \kappa_1 + \kappa_2$ is the total loss rate, with $\kappa_{1,2}$ the leakage rates through the mirrors and γ the intrinsic loss rate due to absorption of the intra-cavity medium. U is the Kerr nonlinearity strength, or the single-photon interaction constant. All model parameters are displayed in Fig. 1.1, so that their meaning can be easily recognized.

Equation (1.1) can be derived or understood in various ways, depending on the starting viewpoint. Starting from a quantum mechanical Hamiltonian in terms of boson operators and the equation of motion for the density matrix, Eq. (1.1) is derived by applying the mean-field approximation and neglecting quantum correlations [93, 94]. The mean-field approximation is valid when the single-photon nonlinearity is weak, i.e., $U \ll \Gamma$; this is the limit relevant to all results in this thesis. Alternatively, the linear part of Eq. (1.1), obtained by setting $U = 0$, can be derived starting from a classical description of a *LC* circuit. This is the simplest model for a resonator in electrical engineering. In that case, the field α in Eq. (1.1) represents the superposition of the voltage and current in the circuit [95]. Yet another perspective on Eq. (1.1) is obtained by realizing that it is essentially a zero-dimensional version of Gross-Pitaevskii equation, or nonlinear Schrodinger equation, widely used in atomic physics [96, 97]. By zero dimensional we mean that the spatial dependence for α is neglected, and the kinetic and potential energy terms are replaced by a single energy value. Note, however, that in contrast to the Gross-Pitaevskii equation describing conservative systems, our equation includes coherent driving and dissipation to account for the input laser and photon loss from the cavity. Finally, to give yet another perspective, we note that Eq. (1.1) somewhat resembles the equation of motion for a Duffing oscillator pioneered in the context of mechanical systems [98]. However, please note that while the cubic nonlinearity is of the same form in the two equations, there are important differences. The Duffing equation describes a real-valued variable and is of second order in time [99, 100]. In contrast, Eq. (1.1) describes a complex-valued variable (necessary to describe the light field's amplitude and phase) and is of first order in time. While the spectral response of these two systems is practically identical in the linear regime, in the nonlinear regime there are very important differences as highlighted in a recent work by Peters and Rodriguez [33].

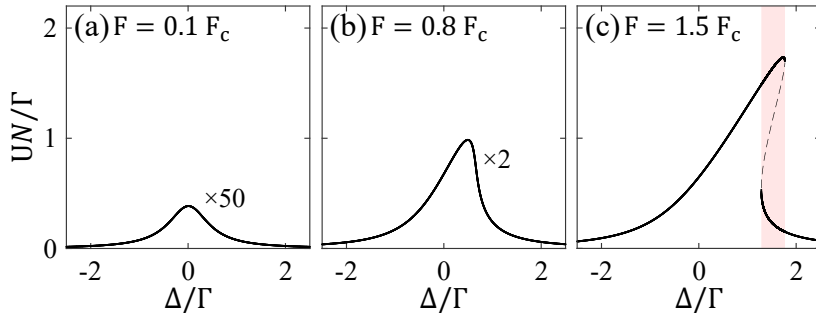


Figure 1.2: Steady state solutions for a single-mode cavity with Kerr nonlinearity at three different driving amplitudes (a) $F = 0.1F_c$, (b) $F = 0.8F_c$, and (c) $F = 1.5F_c$, with F_c the critical driving amplitude for the onset of optical bistability. For clarity, multiplying factors of 50 and 2 are used for data in (a) and (b), respectively. The red-shaded area in (c) indicates the bistable region. For the calculation, we set $\kappa_1 = \kappa_2 = 0.2\Gamma$ and $U = 0.1\Gamma$.

1.2.1 Steady-state analysis

In this subsection we calculate the steady states of our Kerr nonlinear cavity. This is done by setting $\dot{\alpha} = 0$. Multiplying the right-hand side of Eq. (1.1) with its complex conjugate and reorganizing the remaining terms, we end up with an algebraic equation for the photon number $N = |\alpha|^2$ to the third order:

$$\kappa_1 |F|^2 = U^2 N^3 - 2\Delta U N^2 + \left(\Delta^2 + \frac{\Gamma^2}{4} \right) N. \quad (1.2)$$

To calculate the steady states, we can calculate the roots of the above polynomial which is cubic in N . Therefore, mathematically we expect three steady state solutions always. However, physics imposes that N must be real and non-negative, which excludes some solutions of Eq. (1.2) for certain parameter regimes.

Let us first calculate N as a function of Δ for constant F . The result is shown in Fig. 1.2. The vertical axis shows UN/Γ , since this quantity determines whether the system is in the linear or nonlinear regime. All the parameters used for the calculation are given in the caption of Fig. 1.2 in dimensionless form. Most quantities are referenced to Γ since all the physics scales with Γ . The driving amplitudes are referenced to a critical value $F_c = 3^{-3/4}[\Gamma^3/(\kappa_1 U)]^{1/2}$ for bistability [42]. Notice that U enters the expression for F_c . Consequently, the choice of U/Γ does not affect the plotted results in Fig. 1.2.

Figure 1.2 shows that, when $F \ll F_c$, the response is like for a linear Lorentzian oscillator. In this linear regime, $UN \ll \Gamma$. For $F = 0.8F_c$, where $UN/\Gamma \sim 0.5$ maximally, the nonlinear interaction leads to a noticeable tilting of the resonance profile

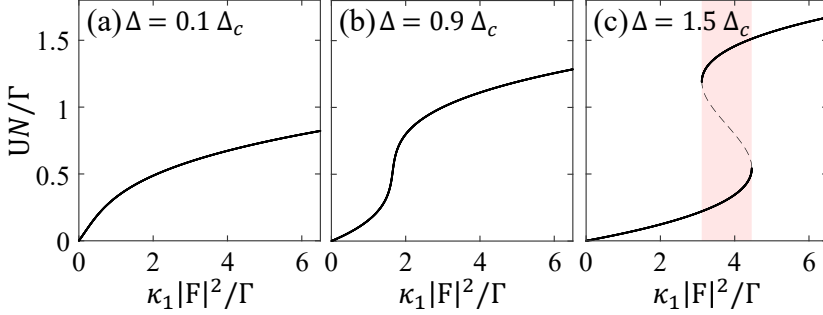


Figure 1.3: Steady state solutions for a single-mode cavity with Kerr nonlinearity at three different detunings: (a) $\Delta = 0.1\Delta_c$, (b) $\Delta = 0.9\Delta_c$, and (c) $\Delta = 1.5\Delta_c$, with Δ_c the critical detuning for the onset of optical bistability $\Delta_c = \sqrt{3}\Gamma/2$. The red-shaded area in (c) indicates the bistable region. All other model parameters are the same as in Fig. 1.2.

towards positive Δ [99]. The direction of the tilting is determined by the sign of U , here chosen to be positive to model repulsive photon-photon interactions. For this driving amplitude, the system has just entered the nonlinear regime. For $F = 1.5F_c$, the nonlinearity dramatically modifies the resonance profile. This results in a region of Δ where three steady-state solutions can be obtained [red shaded region in Fig. 1.2(c)] at a single driving frequency. Through a linear stability analysis [101], one finds that at most two solutions are stable at a given Δ ; this is the so-called optical bistability. Note that optical bistability occurs when the nonlinear interaction energy is comparable to the linewidth of the cavity, i.e., $UN \sim \Gamma$. Experimentally, the nonlinear resonance profile can be probed by dynamically modulating the detuning while measuring the transmitted intensity (e.g., Fabry–Pérot cavity) or scattered light (e.g., photonic crystal), which relate to the intra-cavity photon number N via input-output theory [61, 102, 103]. For the forward (backward) modulation branch, the system will stay in the up (down) branch until the end of the bistable region when the system must switch down (up) to the other state. As a result, a dynamic hysteresis area appears when plotting signals for both modulation directions as a function of detuning. In this thesis, we will demonstrate this manifestation of optical bistability in Chapters 2 and 5.

Next, we fix Δ and calculate N as a function of driving power $|F|^2$ in Fig. 1.3. Figure 1.3(a) shows N as a function of driving power $|F|^2$ for $\Delta = 0.1\Delta_c$. In contrast to a linear Lorentzian oscillator where N always increases linearly with $|F|^2$ for any given detuning, the dependence of N in Fig. 1.3(a) shows a slope change asymptotically to a lower value. This deviation from the initial slope, which corresponds to the linear response of the system at low driving powers, means that the transmittance of the cavity decreases with increased driving power. Therefore, this phenomenon is referred to as the optical limiting effect [101, 104]. For $\Delta = 0.9\Delta_c$, the nonlinear

interaction energy distorts the profile. This distorting trend continues when increasing the driving power, until an S-like curve emerges [2, 95, 99] as shown for $\Delta = 1.2\Delta_c$ in Fig. 1.3(c). This manifestation of optical bistability also has been observed in the form of dynamic hysteresis in many experiments via modulating the driving power up and down [19, 20, 29, 105, 106]. In Chapter 3 of this thesis, we will show this type of optical bistability in a nonlinear grating system. As the model introduced here pertains to a single-mode Kerr nonlinear cavity while our experiment involves a much more complex multimode system (dispersive grating), the experimental results in Chapter 3 cannot be quantitatively reproduced by the current model. Nonetheless, the simple model here still sheds light onto some features. Overall, Fig. 1.3 also shows that for a single-mode Kerr nonlinear cavity there exists a minimum detuning ($\Delta_c = \sqrt{3}\Gamma/2$) for optical bistability to emerge.

1.3 Approaches to realize optical nonlinearity and bistability

The effect of the nonlinear interaction is to shift the resonance frequency by the quantity UN , with U the nonlinearity strength and N the intra-cavity photon number. This shift is described by a linear refractive index change due to the intra-cavity intensity I : $n = n_0 + n_2I$, with n_0 the linear refractive index in absence of light, and n_2 a nonlinear refractive index constant. In nonlinear optics, the mechanism responsible for this intensity-dependent refractive index is referred to as the Kerr effect, quantified by the third-order nonlinear susceptibility $\chi^{(3)}$ [2]. However, a similar intensity-dependence for the material refractive index can also stem from various other mechanisms which do not have an electronic origin.

The work presented in this thesis is based on two different approaches to realize the intensity-dependent refractive index. The first approach is to harness the thermo-optical effect as summarized in Fig. 1.4(a). In this context, the nonlinearity is due to the temperature-dependent refractive index of the medium: $n = n_0 + \frac{dn}{dT}\delta T$, with $\frac{dn}{dT}$ a material constant, and δT the temperature variation of the medium due to light absorption. Historically, interest in this type of nonlinearity is due to various reasons. On one hand, thermo-optical nonlinearity has been studied as an undesired effect concurrent with desired nonlinear effects [107–109]. On the other hand, this type of nonlinearity has been employed to realize various applications such as wavelength tunability for an optical cavity [110, 111], and all-optical switching [46, 112]. In contrast to most previous works where the thermo-optical nonlinearity occurs in a solid-state materials [46, 105–107, 113–116], in this thesis we use olive and cinnamon oils as thermal nonlinear media. This is possible thanks to the type of system (open-access cavity) we investigate, which allows to easily incorporate such inexpensive and easily-accessible oils that have a strong nonlinear response. A schematic of a typical system we use is shown in Fig. 1.4(a). The figure shows a Fabry–Pérot cavity filled with a drop

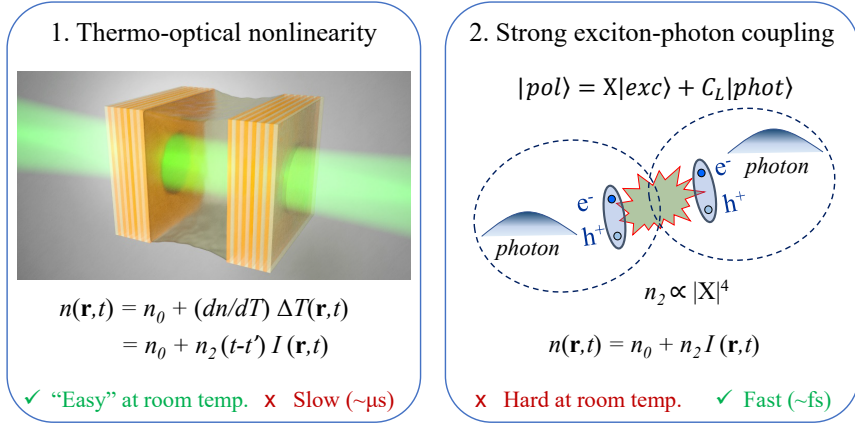


Figure 1.4: Two approaches for realizing Kerr-type nonlinearity in optical cavities: (a) through thermo-optical nonlinearity; (b) through strong exciton-photon coupling and the resultant polaritonic nonlinearity.

of such oil. Oils have been reported to possess a large temperature-dependent refractive index through Z-scan [117–119] or thermal lensing measurements [120, 121] at room temperature. Due to their fluid nature, they also have the advantage to be resistant to strong heating that can potentially damage solid-state thermal nonlinear materials. However, due to its thermal origin, the nonlinearity from oils is relatively slow (tens of microseconds). Although a slow nonlinearity is not desired in many applications that value fast operations, we will show in Chapters 2 and 3 that intriguing nonlinear dynamical phenomena can emerge because of this slow nonlinearity.

Figure 1.4(b) displays the second approach we explore in this thesis to realize an intensity-dependent refractive index. This approach involves strongly coupling cavity photons to semiconductor excitons. The resultant exciton-polaritons mutually interact via the underlying excitons [26, 29, 61, 88, 122–125]. The strength of these polariton-polariton interactions, quantified by the constant U in Eq. (1.1), corresponds to the magnitude of the nonlinear refractive index in the wave picture of light.

Typically, the polaritonic nonlinearity being of electronic origin is much faster than the thermo-optical nonlinearity. Such a fast nonlinearity is desirable for applications where high speed is important. However, realizing strong polariton-polariton interactions at room temperature and under continuous-wave driving is extremely challenging. In fact, to the best of our knowledge, optical bistability as usually probed with a continuous-wave laser has never been realized in any solid-state room-temperature polariton system. The reason is that the strength of the nonlinearity (exciton Bohr radius) is inversely proportional to the exciton binding energy. Therefore, excitons with large binding energies that are robust at room temperature generally have a weak

nonlinearity and viceversa. As a result, strong continuous-wave nonlinearities (as needed to observe optical bistability) have only been observed in cryogenically cooled semiconductors hosting excitons with small binding energies [29, 126]. We note that strong nonlinearities have been realized at room-temperature [127, 128], but only under pulsed excitation since otherwise materials degrade.

In this thesis, we will present our efforts on employing the tunable cavity system to explore CsPbBr₃ perovskite, a newly emerged excitonic material, for achieving optical bistability. Although only this particular material is considered in this thesis, as mentioned in Section 1.1, the setup we built is a generic platform for investigating more novel materials in the future.

1.4 Overview of this thesis

This thesis is organized as follows. Chapters 2 and 3 present experiments involving two different resonant systems with thermo-optical nonlinearity due to an oil layer. In both cases, the resonators are driven by a continuous-wave laser. In Chapter 2, we study the dynamics of light in an oil-filled tunable microcavity. We scan the cavity length across the resonance at different speeds, and find signatures of memory effects in the nonlinear optical response due to the oil. In particular, we discover a universal scaling law for the dynamic optical hysteresis of the cavity as a function of the driving speed. We explain our results by modifying the standard Kerr nonlinear model [Eq. (1.1)] to account for the thermal relaxation time of the nonlinearity. We also show, theoretically, a new regime of non-Markovian dynamics emerging from the interplay of nonlinear memory effects and white noise.

In Chapter 3, we present experiments on a one-dimensional metallic grating covered by oil. We demonstrate optical bistability in the transmitted laser intensity, and a series of novel dynamical effects in the diffracted intensities. In particular, we observe spontaneous symmetry breaking in the intensities radiated by the +1 and -1 diffraction orders. Finally, we also discover a dynamical regime wherein the grating transmission spontaneously begins to oscillate, and the diffracted intensities display a series of spikes reminiscent of the firing of neurons and other excitable systems.

In Chapters 4 and 5, we investigate optical microcavities with perovskite semiconductor crystals. Chapter 4 presents our first experiment in this direction, aimed at realizing strong coupling between cavity photons and excitons in a CsPbBr₃ perovskite crystal at room temperature. We performed measurements with objectives of different numerical apertures (NA), evidencing spectral features resembling Fano resonances and Rabi splittings — signatures of strong light-matter coupling — but which are neither. These features are artificially generated by the NA . Through transfer matrix modelling, we show that these spectral artefacts are due to the incoherent sum of intensities collected by the NA . We conclude the chapter by providing guidelines to avoid pitfalls in the characterization of dispersive optical systems.

In Chapter 5, we describe the construction and characterization of a tunable optical

cavity in a novel closed-cycle cryostat. We characterize the mechanical stability of our cavity in two situations: cryo-cooler OFF and ON. We find sub-atomic stability in the former case, but a rather poor stability in the latter case. Nonetheless, by performing fast measurements (compared to the characteristic time scale of mechanical fluctuations), our tunable cavity can still be used to reveal nonlinear light-matter interactions. In this way, we demonstrate optical bistability in a cavity with perovskite semiconductor for the first time.

Chapter 2

Universal scaling of the dynamic optical hysteresis of a tunable cavity with non-instantaneous nonlinearity

We investigate, experimentally and theoretically, the dynamics of a laser-driven cavity with non-instantaneous effective photon-photon interactions. Scanning the laser-cavity frequency detuning at different speeds across an optical bistability, we find a hysteresis area that is a non-monotonic function of the speed. In the limit of fast scans comparable to the memory time of the interactions, we demonstrate that the hysteresis area decays following a universal power law with scaling exponent -1 . We further demonstrate a regime of non-Markovian dynamics emerging from white noise. This regime is evidenced by peaked distributions of residence times in the metastable states of our system. Our results offer new perspectives for exploring the physics of scaling, universality, and metastability, in non-Markovian regimes using arrays of bistable optical cavities with low quality factors, driven by low laser powers, and at room temperature.

2.1 Introduction

Photons in a nonlinear cavity can undergo phase transitions akin to condensed matter systems. Since the seminal works by Graham and Haken [129], Roy and Mandel [130], and Scully [131], lasers have inspired numerous studies of phase transitions of light. Recently, coherently driven cavities supporting mean-field bistability — two steady-states at a single driving condition — have taken a central role in studies of photonic phase transitions [29, 30, 35, 40, 41, 67, 68, 132–138]. Progress in this field has been recently accelerated by three developments. First, various nonlinear photonic resonators, and novel methods to probe their dynamics, are becoming available [29, 35, 134, 135, 137]. Second, fresh insights coupled to novel theoretical methods have revealed intriguing non-equilibrium phases of nonlinear cavities [40, 41, 64, 67, 136, 139–141]. Third, there is increasing interest in performing optimization [42, 142, 143] and computation [75] with bistable cavity arrays.

Descriptions of bistable cavities commonly assume instantaneous effective photon-photon interactions [61]. In the mean-field equation of motion for the intracavity field α , this assumption manifests as a Kerr nonlinearity of the form $|\alpha|^2\alpha$ [93]. The same cubic nonlinearity is found in the Gross-Pitaevskii equation employed in atomic physics [96, 97, 144], in the Ginsburg-Landau theory of superconductivity [145], in the Lugiato-Lefever equation of nonlinear optics [146], and in the force derived from Goldstone’s Mexican hat potential $V = -|\phi|^2 + |\phi|^4$ for the scalar field ϕ at the heart of the Higgs mechanism [147]. In optics, strong Kerr nonlinearities arise in semiconductor cavities where exciton-exciton interactions are effectively instantaneous [61]. A drawback of those cavities is that optical bistability based on Kerr nonlinearities is typically only observed at cryogenic temperatures. In contrast, several optical resonators with slow but strong thermal nonlinearities have routinely displayed bistability at room temperature [46, 105, 107, 148–151]. As bona fide bistable systems, thermo-optical resonators may open up new perspectives for classical Hamiltonian simulation and computation [42, 75, 142, 143, 152]. However, the influence of the thermal relaxation time on the hysteretic and stochastic dynamics of bistable cavities remains to be addressed.

In this chapter, we demonstrate signatures of scaling, universality, and memory, in the dynamics of a laser-driven cavity with thermo-optical nonlinearity. This nonlinearity is associated with non-instantaneous effective photon-photon interactions, and it results in room-temperature optical bistability at low laser powers $P \sim 70 \mu\text{W}$. Scanning the laser-cavity detuning, we observe an optical hysteresis influenced by the ratio of the scanning time to the memory time of the interactions. In contrast to previous reports of dynamic hysteresis in resonators with effectively instantaneous interactions [28, 29, 153, 154], we find a hysteresis area that is a non-monotonic function of the scanning speed. Moreover, we discover a universal scaling of the hysteresis area in the limit of fast scans. Our results elucidate how the hysteretic behavior characterizing first-order phase transitions, and the boundary between phases, dynamically vanish when the

nonlinearity has a finite memory time. Furthermore, we evidence a new regime of non-Markovian dynamics characterized by peaked distributions of residence times in metastable states. Interestingly, this new non-Markovian regime emerges under the influence of white noise.

2.2 Experimental setup

Figure 2.1(a) illustrates our system: a tunable Fabry-Pérot cavity driven by a 532 nm continuous-wave laser. The cavity is made by a concave and a planar mirror, each comprising a distributed Bragg reflector (DBR) on a glass substrate. The mirrors have a peak reflectance of 99.9% at 530 nm, which is the center of the stop-band. The concave mirror, with a diameter of 7 μm and a radius of curvature of 12 μm , was fabricated by milling a glass substrate with a focused-ion beam prior to the deposition of the DBR [92]. An image of the sample containing concave mirrors of various sizes is shown in Fig. 2.1(c). The dashed circle indicates the one used in our experiment. Single-mode operation is ensured by the strong lateral confinement and high reflectivity of the mirrors.

The cavity mirrors are aligned parallel to each other by controlling all three translational (rotational) degrees of freedom of the concave mirror with nanometer (micro-degree) precision using a nanopositioner. The planar mirror is mounted on a linear actuator used to scan the cavity length, and is kept still during the alignment process. We monitor the cavity alignment by illuminating the cavity with a collimated 635 nm light beam while imaging the resultant Fabry-Pérot fringes across the cavity plane [155]. The symmetry and the spacing of the fringes are used as a reference to guide the cavity alignment. With this method, an uncertainty of ~ 3 milli-degree is achieved.

To study the optical response of our cavity, we measured the transmitted intensity of a laser while modulating the laser-cavity detuning. An optical setup was built as sketched in Fig. 2.1(b). We used a single-mode 532 nm continuous-wave laser to drive the cavity. Excitation and collection were achieved through $10\times$ microscope objectives with numerical aperture $NA = 0.25$. In all measurements, we drove the fundamental transverse mode of the 9th measurable longitudinal mode of the cavity. Taking into account the electric field penetration into the DBRs, the effective cavity length is $\sim 3 \mu\text{m}$. To exclude multi-mode interference effects, we optimized the in-coupling efficiency of the laser into the desired mode by finely adjusting the position of the concave mirror relative to the laser beam. Finally, the transmitted laser signal was measured by a photodetector.

The laser-cavity detuning was modulated by scanning the cavity length via the linear actuator that supported the planar mirror. This actuator is in closed-loop configuration that enables us to specify the modulation waveform, travel range and frequency through software. In all measurements, we specified a symmetric triangular waveform with a travel range of 350 nm, and only varied the frequency. For modulation frequencies above ~ 50 Hz, we suspected that the actual travel range of the actuator differed from

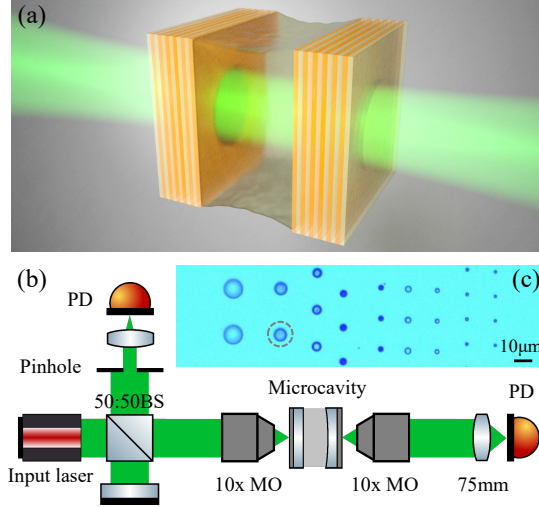


Figure 2.1: (a) Schematic of a plano-concave cavity filled with oil, as in our experiments. (b) Schematic of the experimental setup. MO is microscope objective, PD is photodetector. (c) Microscope image of a sample containing concave mirrors of different sizes. The encircled concave mirror, which has a radius of curvature of $12 \mu\text{m}$, is used in our experiments.

the specified one. Therefore, we used a Michelson interferometer in the input path of the setup [see Fig. 2.1(b)] to characterize the mirror displacement. In particular, we measured the time-dependent intensity of a small section of the interferogram while the cavity length was being modulated. Next, we fitted the measured intensity with a two-beam interference equation. Through this analysis, we obtained the actual ranges travelled by our mirror at different frequencies, based on which we could calculate the scanning speeds along the horizontal axis for Fig. 2.4. Once this calibration was finished, the beam splitter for the Michelson interferometer was removed in order to avoid unwanted reflections that could disturb the hysteresis measurements.

2.3 Optical bistability and steady-state analysis

To endow the cavity with a nonlinear optical response, we place olive oil inside the cavity [117, 118, 156]. Through z-scan measurements we estimated the nonlinear refractive index n_2 of our oil to be $\sim -5 \times 10^{-8} \text{ cm}^2/\text{W}$ at 532 nm, consistent with Ref. [118]. Figure 2.2 shows the laser transmitted intensity through our oil-filled cavity averaged over 70 modulation cycles and at three laser powers. Green and black data points correspond to opening and closing the cavity, respectively. For low powers

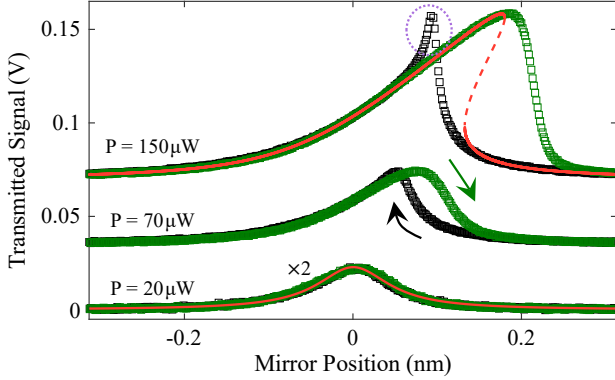


Figure 2.2: Average hysteresis measured by scanning Δ/Γ [see Eq. (2.1)] at constant speed for three driving powers P . Green (black) curves correspond to opening (closing) the cavity. The overshoot enclosed by the dotted circle emerges from non-instantaneous effective photon-photon interactions. For clarity, we multiplied the measurements for $P = 20 \mu\text{W}$ by 2 and vertically displaced the other measurements. Red curves are calculations with Eq. (2.1) as explained in the text.

$P \lesssim 20 \mu\text{W}$, the cavity response is linear. The red curve over the measurements for $P = 20 \mu\text{W}$ is a Lorentzian fit, yielding a resonance linewidth of $0.104 \pm 0.001 \text{ nm}$. For $P = 70 \mu\text{W}$, the transmission displays hysteresis (see arrows in Fig. 2.2) and bistability around a mirror position of 0.1 nm. The power needed for bistability in our cavity is similar to that in state-of-the-art monolithic semiconductor cavities [29, 35, 157], but at conveniently lower quality factors (by a factor of ~ 10) and operating at room-temperature instead of $\sim 5 \text{ K}$. For $P = 150 \mu\text{W}$, the bistability and hysteresis range enlarge as expected. In Appendix 2.8.1, we estimate the laser-induced temperature rise in our cavity based on the temperature-dependent refractive index of olive oil [158].

All measurements in Fig. 2.2 correspond to linear ramps of the cavity length at $1.75 \mu\text{m/s}$. Already for this slow scan, an overshoot followed by a slow decay of the transmitted intensity arises when closing the cavity in the nonlinear regime. This overshoot is due to the finite thermal relaxation time of the oil-filled cavity, which is absent in the standard Kerr nonlinearity [107]. The standard Kerr model for the intra-cavity mean-field α in a frame rotating at the driving frequency ω is

$$i\dot{\alpha} = \left(-\Delta - i\frac{\Gamma}{2} + U|\alpha|^2 \right) \alpha + i\sqrt{\kappa_1}F. \quad (2.1)$$

Here $\Delta = \omega - \omega_0$ is the laser-cavity detuning, with ω_0 the resonance frequency of the cavity. U is the effective photon-photon interaction strength mediated by the nonlinear medium [61]. F is the driving amplitude. The total loss rate $\Gamma = \kappa_1 + \kappa_2 + \gamma$ is the sum

of the input-output leakage rates through the two mirrors, $\kappa_{1,2}$, and the intrinsic cavity loss rate γ due to absorption. The steady-states follow from setting $\dot{\alpha} = 0$ in Eq. (2.1).

We attempted to fit the steady-state photon density $|\alpha|^2$ calculated with Eq. (2.1) to the measurements for $P = 150 \mu\text{W}$ in Fig. 2.2, with F as the only relevant adjustable parameter. Γ is fixed by the measured linewidth in the linear regime. Furthermore, since Eq. (2.1) is a mean-field model, the absolute values of $|\alpha|^2$ and U are irrelevant; the spectral lineshape is determined by the ratio $U|\alpha|^2/\Gamma$. Various lineshapes can be obtained by varying F for fixed U and Γ . Thus, we adjusted F until obtaining the red curve plotted over the measurements for $P = 150 \mu\text{W}$. Solid and dashed curves represent stable and unstable states, respectively. Stability was analyzed as in Refs. [32, 93]. The fit is good far from resonance, but deviates from the data near the bistability. This deviation increases with the scanning speed, as shown next.

2.4 Dynamic hysteresis with non-instantaneous nonlinearity

We performed hysteresis measurements for $P = 150 \mu\text{W}$ and various scanning speeds. A laser power far above the bistability threshold limits the influence of noise on our measurements. Figure 2.3(a) shows average hysteresis measurements for three speeds. Top to bottom, the speeds are v , $7v$, and $49v$, with $v = 0.74 \mu\text{m/s}$. The transmitted intensity is shown versus Δ/Γ , determined by the mirror position and resonance linewidth in Fig. 2.2. Figure 2.3(a) shows how the hysteresis cycle changes with the scanning speed. Increasing the speed from v to $7v$ makes the overshoot broader and the hysteresis wider. Interestingly, further increasing the speed to $49v$ makes the overshoot broader but the hysteresis narrower. At $49v$ the lineshape for both scanning directions resembles a Lorentzian, which suggests approximately linear response for fast scans regardless of the power.

The behavior in Fig. 2.3(a) can be explained by considering the finite heating and cooling time of our oil-filled cavity; this makes effective photon-photon interactions non-instantaneous. Therefore, we modify Eq. (2.1) by letting

$$U|\alpha(t)|^2 \rightarrow \int_0^t ds K(t-s)|\alpha(s)|^2 \equiv w(t), \quad (2.2)$$

with the kernel function defined as $K(t) = \frac{U}{\tau} e^{-t/\tau}$. The memory time of the interactions, τ , corresponds to the thermal relaxation time of our cavity. Here we have followed the prescription of Mori [159] and Hänggi [160] for dealing with finite-time interactions. However, whereas Mori-type equations involve non-instantaneous dissipation, we introduced non-instantaneous nonlinearity.

Making the substitution Eq. (2.2) in Eq. (2.1) yields an integro-differential equation, which can be conveniently (for numerical simulation) written as two coupled differential

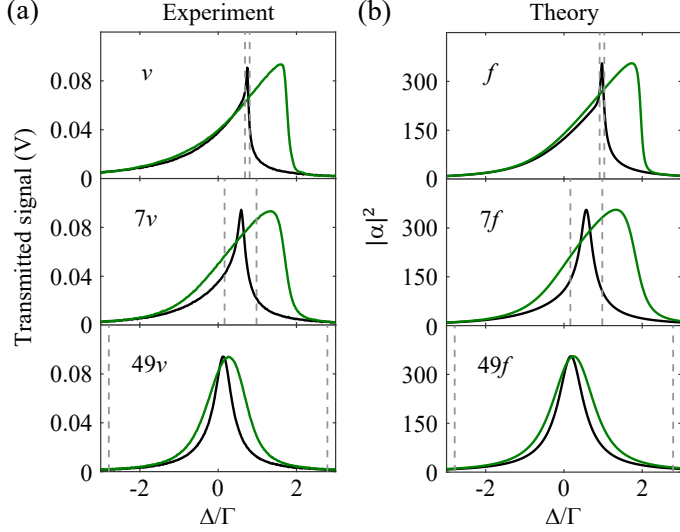


Figure 2.3: (a) Measurements and (b) calculations of average hysteresis when Δ/Γ is scanned at three different speeds and constant power. The slowest scanning speed is $v = 0.74 \mu\text{m/s}$ in (a), and $f = 5.97 \times 10^{-6} \Gamma^2$ in (b). The power is $P = 150 \mu\text{W}$ in (a) and $F = 1.52F_c$ in (b), with F_c the critical amplitude needed for bistability (see Appendix 2.8.1); the power in (a) also corresponds to $F = 1.52F_c$. Measurements are averaged over 70 realizations. Dashed lines indicate the range of Δ/Γ corresponding to the thermal relaxation time τ .

equations:

$$i\dot{\alpha}(t) = \left(-\Delta - i\frac{\Gamma}{2} + w(t) \right) \alpha(t) + i\sqrt{\kappa_1}F, \quad (2.3a)$$

$$\dot{w}(t) = [U|\alpha(t)|^2 - w(t)]/\tau. \quad (2.3b)$$

Equation. (2.2) and Eq. (2.3) imply that the state of the system depends on its entire past, weighted by the memory kernel $K(t)$. Thus, interactions are non-local in time. Note that when $\alpha(t)$ is constant and can be taken out of the integral in Eq. (2.2), we recover Eq. (2.1). Hence, steady states are unchanged by $K(t)$.

Figure 2.3(b) shows dynamic hysteresis calculations using Eqs. (2.3), with the same parameter values used for the steady-state calculations in Fig. 2.2. As for the experiments, we show scanning speeds a factor of 7 apart. The model reproduces all features observed in experiments. In the calculations, we set the memory time to $\tau = 10^4 \Gamma^{-1}$ and the slowest scanning speed to $f = 5.97 \times 10^{-6} \Gamma^2$. Relative to the experiments, the value of τ is smaller (details ahead) and the speed is larger. We rescaled timescales to avoid unnecessarily long and memory-expensive calculations.

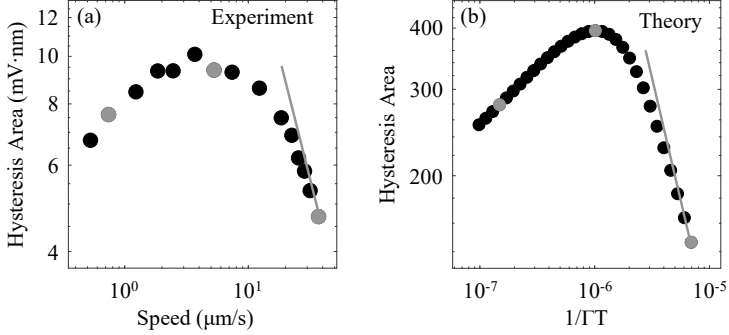


Figure 2.4: (a) Measured and (b) calculated hysteresis area versus scanning speed, in the same dynamic range. Measurements are averaged over 70 realizations. Gray data points indicate the speeds presented in Fig. 2.3. Gray lines are power laws with exponent -1 .

Our mean-field calculations can be directly compared to experiments, because we respect the hierarchy of timescales in experiments: $\Gamma^{-1} \ll \tau \lesssim T_b$, with T_b the scanning time across the bistability. Moreover, the ratio T_b/τ is similar for experiments and calculations.

Now we can estimate the experimental thermal relaxation time by comparing hysteresis cycles in Fig. 2.3. Since in theory we set τ and the scanning speed for Δ/Γ , we can convert τ to a range of Δ/Γ and viceversa. In Fig. 2.3(b) we indicate the Δ/Γ range corresponding to τ by dashed lines. As expected, the Δ/Γ range corresponding to τ increases with the speed. For the lowest speed f , $T_b \gg \tau$ and the overshoot observed when Δ decreases is the main feature unanticipated by the standard Kerr model. For $7f$, $T_b \sim \tau$ and the overshoot is almost as wide as the bistability. For $49f$, $T_b < \tau$ and we have a close-to-linear response. Experiments in Fig. 2.3(a) display similar behavior as calculations in Fig. 2.3(b). Hence, in the same fashion we also indicate the Δ/Γ range corresponding to τ by dashed lines in Fig. 2.3(a). Based on this range of Δ/Γ and our knowledge of the experimental scanning speed, all three measurements in Fig. 2.3(a) are consistent with a relaxation time $\tau = 16 \pm 1 \mu\text{s}$.

In Fig. 2.4(a) we plot the experimental average hysteresis area $A = \int_0^T |I_{\Delta\uparrow} - I_{\Delta\downarrow}| dt$, with $I_{\Delta\uparrow}$ and $I_{\Delta\downarrow}$ the transmitted intensity when Δ increases and decreases, respectively. T is the driving period, which exceeds T_b . Figure 2.4(b) shows the corresponding calculations based on Eqs. (2.3). In both measurements and calculations, A peaks at a scanning speed corresponding to the cross-over between two regimes. For slow scans, A increases with the speed because the cavity cannot adiabatically follow $\Delta(t)$. This regime of dynamic hysteresis and the corresponding scaling laws for A have been previously explored [28, 29, 153, 161]. The second and new regime we investigate comprises speeds above the value for which A peaks. Therein, A decays with increasing

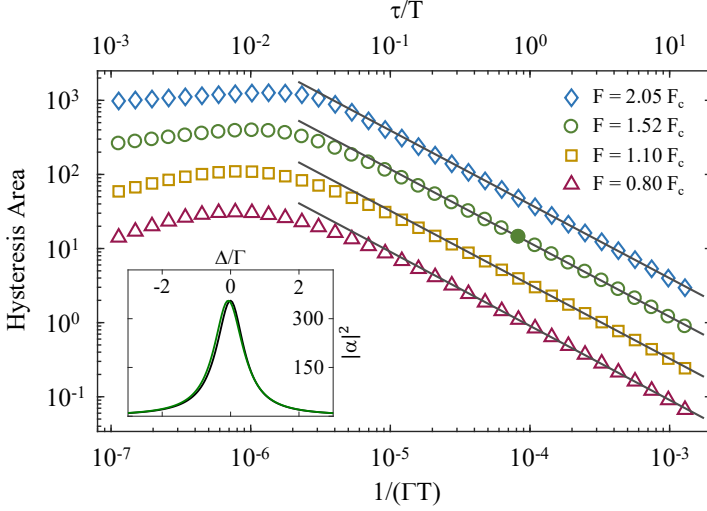


Figure 2.5: Calculated hysteresis area versus the inverse of scanning period. Each symbol corresponds to a different driving amplitude F relative to the critical amplitude needed for bistability F_c . Gray lines are power law with exponent -1 . Inset: Intracavity photon number $|\alpha|^2$ versus Δ/Γ for the period indicated by the filled circle in the main panel.

speed, because the nonlinearity does not have time to build up during the scan. At high speeds, the dynamics of the system transition from nonlinear to linear. The number of attractors changes from two to one.

Our measurements are limited to scanning speeds between $\sim 0.5 \mu\text{m/s}$ and $\sim 40 \mu\text{m/s}$. The upper speed limit is determined by the resonance frequency of our piezoelectric actuator. On the other end, we limited our measurements to speeds above $0.5 \mu\text{m/s}$ to avoid low-frequency mechanical noise in our setup. Despite these limitations, the good agreement between experiments and calculations encourages us to use our model to interpret the physics over an extended speed range.

2.5 Universal scaling of the dynamic hysteresis area

In Fig. 2.5 we calculate A versus the scanning speed for different F . At low speeds, the driving conditions determine the scaling of A [29]. At high speeds, A decays following a power law with scaling exponent -1 (gray lines). Interestingly, this scaling behavior is universal; i.e., the slope of the gray lines fitted to the data in Fig. 2.5 is independent of the system parameters. To assess whether our experiments display such scaling behavior, in Fig. 2.4(a) we plot a power law with exponent -1 over our high-speed

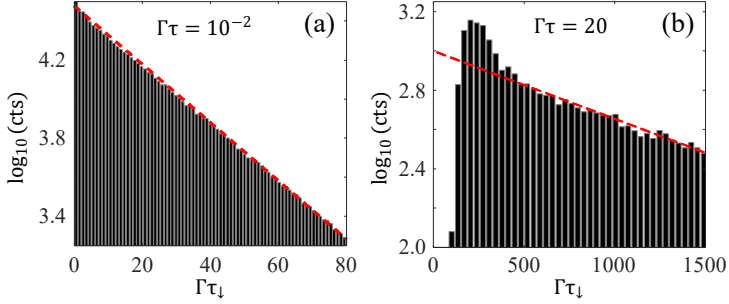


Figure 2.6: Residence time distributions in the lower metastable state for different τ . Dashed lines are exponential fits. The peaked distribution in (b) is indicative of non-Markovian dynamics.

data points. The fit suggests that we reached the onset of the -1 power law regime. For comparison, we plot a -1 power law on top of the corresponding calculations in Fig. 2.4(b). In this case, the power law was fitted to the calculations in Fig. 2.5 over an extended range. As in experiments, we observe the onset of the -1 power law within the restricted speed range in Fig. 2.4(b).

Recent calculations [28] and experiments [29] on hysteretic cavities with instantaneous interactions observed a universal scaling of A at low speeds due to quantum fluctuations. Coincidentally, the scaling exponent found in Refs. [28, 29] is also -1 , as in the present work. However, the scaling behavior here reported has an entirely different origin (i.e., due to non-instantaneous interactions and unrelated to fluctuations) and arises in the opposite regime of fast scans.

2.6 Memory effects due to the thermo-optical nonlinearity

Next, we demonstrate a new regime of non-Markovian dynamics emerging from the interplay of non-instantaneous effective photon-photon interactions and white noise in the laser amplitude and phase. For fixed F and Δ/Γ within the bistability, $|\alpha|^2$ randomly switches between metastable states as shown in Appendix 2.8.3. Based on many long trajectories $|\alpha(t)|^2$, we calculate residence time distributions (RTDs) in the metastable states. For example, Fig. 2.6 show RTDs in the lower metastable state for two different τ . For $\tau \ll \Gamma^{-1}$, the dynamics is Markovian and RTDs decay exponentially as in Fig. 2.6(a). For $\tau > \Gamma^{-1}$, RTDs become increasingly peaked with increasing τ . The deviation from exponential decay [see the poorly fitting line in Fig. 2.6(b), for $\Gamma\tau < 500$] evidences non-Markovian dynamics [162]. Non-Markovian dynamics are usually associated with non-instantaneous system-environment interactions (dissipa-

tion), and with colored noise in the driving force according to the fluctuation-dissipation relation [159, 160, 163–166]. In contrast, we demonstrate non-Markovian dynamics emerging from non-instantaneous effective photon-photon interactions, which suppress fast switchings between metastable states regardless of the noise spectrum. Experimentally, our system also experiences colored noise in Δ due to mechanical fluctuations of our mirrors with high-frequency cutoff. In Appendix 2.8.4, we show how this noise influences single-shot dynamic hysteresis measurements.

2.7 Conclusion

In summary, we have demonstrated signatures of scaling, universality, and non-Markovianity, in the dynamics of a laser-driven cavity with thermo-optical nonlinearity. Because of non-instantaneous effective photon-photon interactions, the optical hysteresis area is maximized at a finite scanning speed. At high speeds, we discovered a universal scaling behavior through which the hysteresis characterizing first-order phase transitions vanishes. Our findings suggest that oil-filled cavities are promising for exploring critical phenomena and new universality classes in systems with memory [167, 168]. For slow or fixed driving conditions, our system exhibits peaked RTDs and non-Markovian dynamic hysteresis. This suggests that our system could be used to test theorems of non-equilibrium fluctuations [169], entropy production [170], and speed limits [171] in non-Markovian regimes. Beyond single-cavity physics, our observation of optical bistability in oil-filled cavities paves the way for realizing bistable coupled cavities [172] and cavity arrays at room-temperature. Such arrays could be used to probe Ising-type phase transitions [41] or to solve combinatorial optimization problems [42, 142, 143].

2.8 Appendices

2.8.1 Temperature rise in the oil-filled cavity

Here we estimate the temperature rise of our oil-filled cavity in the nonlinear regime. To this end, let us first consider the mean-field equation of motion for the coherent field α in a driven-dissipative Kerr nonlinear cavity, i.e., Eq. (2.1). Calculating the steady-state solutions to Eq. (2.1), one finds that the number of photons in the cavity $N = |\alpha|^2$ satisfies:

$$N = \frac{\kappa_1 |F|^2}{\tilde{\Delta}^2 + (\Gamma/2)^2}. \quad (2.4)$$

As described before, Γ is the total loss rate, U is the effective photon-photon interaction strength, κ_1 is the input-output leakage rate, and F is the driving amplitude. In addition, we have defined the quantity

$$\tilde{\Delta} = \Delta - UN, \quad (2.5)$$

with $\Delta = \omega_L - \omega_0$ the laser-cavity detuning, and UN the total interaction energy associated with a population of N photons.

In Eq. (2.4), N appears as a Lorentzian function of the effective detuning $\tilde{\Delta}$. However, since N also enters into the right hand side of Eq. (2.4) via $\tilde{\Delta}$, N is a multi-valued function of the driving parameters F and Δ . Indeed, Eq. (2.4) corresponds to a third order polynomial in N . This means that, in general, three steady-state solutions exist for a single driving condition. Of these three solutions, at most two are stable; this is known as bistability. The critical driving amplitude for observing bistability is $F_c = 3^{-3/4} \sqrt{\Gamma^3 / (\kappa_1 U)}$ [42].

Next, we analyze the resonant response of our oil-filled cavity. The cavity resonance frequency is

$$\omega_0 = \frac{qc\pi}{nL}, \quad (2.6)$$

with c the speed of light, q the longitudinal mode number, n the linear refractive index of the oil at ambient temperature, and L the cavity length. When the cavity length is scanned under laser illumination, the resonance frequency changes to

$$\tilde{\omega}_0 = \pi qc \frac{1}{(n + \delta n)} \frac{1}{(L + \delta L)}, \quad (2.7)$$

with δn the refractive index change due to laser-induced heating of the oil, and δL the change in cavity length due to the scan. Next, we give an approximate expression for Eq. (2.7) based on two observations: (i) As Fig. 2.2 shows, the hysteresis range spans less than 0.2 nm in mirror displacement even for the highest laser power used in our experiment. Meanwhile, the initial cavity length is $\sim 3 \mu\text{m}$. Hence, $\delta L \ll L$.

(ii) δn is on the order of 10^{-4} [158]. Thus, we have $\delta n \ll n$. Based on the above two inequalities,

$$\tilde{\omega}_0 \approx \frac{\pi qc}{nL} \left(1 - \frac{\delta n}{n} - \frac{\delta L}{L} \right). \quad (2.8)$$

Next, we insert Eq. (2.8) into Eq. (2.5). For convenience and without losing generality, we set the center of the modulated cavity length (L_c) to match the laser driving frequency ω_L , i.e., $qc/(2nL_c) = \omega_L$. Consequently, we obtain

$$\tilde{\Delta} = \omega_L \frac{\delta L}{L_c} + \omega_L \frac{\delta n}{n}. \quad (2.9)$$

The first term on the right hand side of Eq. (2.9) corresponds to the detuning Δ in Eq. (2.5). The second term corresponds to the interaction energy, which is proportional to the intensity-induced refractive index change δn .

For our oil-filled cavity with thermo-optical nonlinearity, δn is given by

$$\delta n = \frac{dn}{dT} \delta T, \quad (2.10)$$

with dn/dT a material constant and $\delta T = T - T_0$ the temperature change of the oil due to the light intensity stored inside the cavity.

Next, we estimate δT based on energy conservation arguments, similar to Ref. [107]. δT is related to the heat that goes inside and outside the cavity, i.e., q_{in} and q_{out} , via

$$C\dot{\delta T} = \dot{q}_{in} - \dot{q}_{out}, \quad (2.11)$$

with C the heat capacity of the oil. Next, we assume that $\dot{q}_{in} = RN$, with N the number of photons in the cavity and R a constant describing the conversion of absorbed photons into heat. Furthermore, we assume that $\dot{q}_{out} = S\delta T$, with S a constant describing heat dissipation into the environment. Hence, Eq. (2.11) becomes

$$C\dot{\delta T} = RN - S\delta T. \quad (2.12)$$

Therefore in steady state ($\dot{\delta T} = 0$), the temperature rise δT is proportional to the photon number N :

$$\delta T = \frac{R}{S}N. \quad (2.13)$$

Combining Eq. (2.9), Eq. (2.10), and Eq. (2.13), we find expressions for the effective detuning $\tilde{\Delta}$, the linear detuning Δ , and the thermo-optically induced interaction constant U_T :

$$\tilde{\Delta} = \Delta - U_T N, \quad (2.14a)$$

$$\Delta = \omega_L \frac{\delta L}{L_c}, \quad (2.14b)$$

$$U_T = -\omega_L \frac{1}{n} \frac{dn}{dT} \frac{R}{S}. \quad (2.14c)$$

Based on the above analysis, we can estimate the temperature rise in the measurement of $P = 150 \mu\text{W}$ shown in Fig. 2.2. Eq. (2.13) states that the highest temperature in the measurement corresponds to the largest N . From Eq. 2.4 the largest N corresponds to $\tilde{\Delta} = 0$. Using Eq. (2.9) and Eq. (2.10), we obtain

$$\tilde{\Delta} = \omega_L \frac{\delta L}{L_c} + \omega_L \frac{1}{n} \frac{dn}{dT} \delta T = 0. \quad (2.15)$$

We solve the above expression for δT , and insert the parameter values corresponding to our experiment with a driving power of $150 \mu\text{W}$. In Fig. 2.2 we observe $\delta L = 0.177 \text{ nm}$. The cavity length is $L \sim 3 \mu\text{m}$, and the linear refractive index of our oil at $\lambda = 532 \text{ nm}$ is $n \approx 1.45$. In addition, based on Ref. [158] we estimate $dn/dT \sim -4 \times 10^{-4} \text{ }^\circ\text{C}^{-1}$. Inserting these numbers in Eq. (2.15), we find the greatest temperature rise in Fig. 2.2 is $\delta T = 0.2 \text{ }^\circ\text{C}$.

Finally, we show that the above analysis is consistent with our description based on a non-instantaneous nonlinearity as presented in Section 2.4. Note that Eq. (2.12) couples to the equation of motion for the cavity field α via δT , which appears in $\tilde{\Delta}$ through δn :

$$i\dot{\alpha} = \left(-\Delta - i\frac{\Gamma}{2} - \omega_L \frac{1}{n} \frac{dn}{dT} \delta T \right) \alpha + i\sqrt{\kappa_1} F. \quad (2.16)$$

Using Eq. (2.14c) and setting $w \equiv U_T \frac{\delta}{R} \delta T$ and $\tau \equiv \frac{C}{S}$ (note $\frac{C}{S}$ has unit of time), the new form of the coupled equations of motion read:

$$i\dot{\alpha} = \left(-\Delta - i\frac{\Gamma}{2} + w \right) \alpha + i\sqrt{\kappa_1} F, \quad (2.17a)$$

$$\dot{w} = [U_T N - w] / \tau. \quad (2.17b)$$

This new form is identical to Eqs. (2.3). Therefore, we can conclude that the model proposed in this Appendix, derived by inspecting coupled dynamics of the oil temperature and light field, is mathematically identical to our model in terms of a non-instantaneous nonlinearity with exponential memory kernel.

2.8.2 Calculation details

Here we provide further details about the calculations, and we explain how parameter values were determined or selected. Let us first consider the steady-state calculations based on Eq. (2.1) and presented in Fig. 2.2. In particular, we fitted the steady-state photon number $|\alpha|^2$ to the experimental transmitted signal ($\propto |\alpha|^2$) for a laser power $P = 150 \mu\text{W}$. The model parameters are the photon-photon interaction strength U , the

total loss rate Γ , the driving amplitude F , and the input-output leakage rates $\kappa_{1,2}$. At first sight, it may seem that these five parameters can be freely adjusted in order to fit the measured lineshape. However, as explained next, we do not have this freedom due to several considerations and constraints.

The starting point of our analysis is the realization that Eq. (2.2) is a mean-field model neglecting quantum fluctuations. Hence, the value of each parameter individually, or of $|\alpha|^2$, is irrelevant. The spectral lineshape is entirely determined by the ratio $U|\alpha|^2/\Gamma$. In particular, the linear regime is characterized by $U|\alpha|^2 \ll \Gamma$. Bistability emerges for $U|\alpha|^2 \gtrsim \Gamma$.

Next, we explain how the model parameters relevant to the fit in Fig. 2.2 are set. First, the value of Γ is determined by fitting a Lorentzian function to the measured lineshape in the linear regime ($P = 20 \mu\text{W}$). Second, note that κ_1 is just a multiplicative factor for F . In fact, we could have defined an effective driving amplitude $F' = \sqrt{\kappa_1}F$ in Eq. (2.1) and not introduced κ_1 at all. We include $\kappa_{1,2}$ in our model for consistency with standard input-output theory, and to have the right units for F . Therefore, we set $\kappa_1 = \gamma/2$ without this choice having any impact on our analysis. Furthermore, the value of κ_2 and γ do not need to be specified in the calculation at all. Only Γ needs to be specified. Third, we set $U = 0.005 \Gamma$. This choice determines the number of photons $|\alpha|^2$ involved in the bistability and the critical driving amplitude F_c needed to reach the bistable regime. Note, however, that any spectral lineshape can be attained for any value of U by scaling F (which determines $|\alpha|^2$) accordingly. Therefore, our choice of U does not impact our analysis. Based on the above considerations and the choice of U , we are left with F as the only adjustable parameter used to fit the calculated lineshape to the measured lineshape. At this point, we would like to note an additional constraint related to the critical driving amplitude F_c for which bistability emerges. In particular, for $F = F_c$ we have $U|\alpha|^2 \sim \Gamma$. Experimentally, we can estimate F_c by performing dynamic hysteresis measurements at different powers. F_c then corresponds to the minimum laser amplitude for which bistability is observed. Consequently, any laser amplitude can be referenced to F_c . In this way, we find that the value $F/F_c = 1.52$ (as obtained from the calculations) giving the best fit to the experimental data is fully consistent with our experimental estimate of $F/F_c \approx 1.5$. Finally, we note that the fact that F/F_c is the relevant way to express the driving amplitude in our mean-field model, combined with the fact that κ_1 determines F_c , further supports the statement that the value of κ_1 we selected is irrelevant to our analysis of the spectral lineshape.

For dynamic hysteresis calculations based on Eqs. (2.3), we use the same parameter values as mentioned above. In addition, we set the thermal relaxation time to be $\tau = 10^4 \Gamma^{-1}$. Our choice of the value of τ , which is somewhat shorter than the experimental one as explained in Section 2.4, is based on two considerations. First, calculations using the experimental value of τ will be extremely long and memory-expensive. Second, as long as $\tau \gg \Gamma^{-1}$, the physics of dynamic hysteresis in our single-mode cavity remains qualitatively the same. A longer τ will simply shift the maximum hysteresis area to slower scans speeds, and will not change the shape of

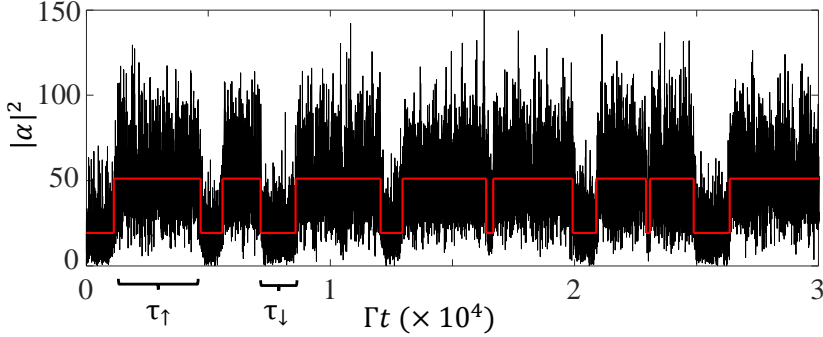


Figure 2.7: The black curve is a simulated trajectory of the photon density $|\alpha|^2$ as a function of time. The red line indicates switching events between the two meta-stable states. τ_{\uparrow} and τ_{\downarrow} are the residence times in the high and the low density state, respectively. For the calculations, we set $\Gamma = 1$, $\gamma = \Gamma/6$, $\kappa_1 = \Gamma/2$, $F = 5\sqrt{\Gamma}$, $\Delta = 1.216 \Gamma$, $U = \Gamma/40$, $\tau = 20/\Gamma$, $D = 2 \Gamma$, and $\beta = 3 \times 10^4$.

the hysteresis area curve as a function of the scanning speed. Therefore, we select a sufficiently large value of τ that still allows us to perform the calculations within a reasonable (\sim days) time.

The scans we performed to calculate the hysteresis area consist of varying the detuning Δ in a linear and symmetric way from -20Γ to 20Γ . Finally, since the equations of motion are deterministic, it is sufficient to calculate the response for only one period for each T .

2.8.3 Residence time analysis

Here we explain how the residence time distributions (RTDs) in Fig. 2.6 are calculated. We consider the influence of white noise in the laser amplitude and phase by adding two stochastic terms to the right-hand side of Eq. (2.3a). Thus, the equations of motion become:

$$i\dot{\alpha}(t) = \left(-\Delta - i\frac{\Gamma}{2} + w(t) \right) \alpha(t) + i\sqrt{\kappa_1}F + D\zeta(t), \quad (2.18a)$$

$$\dot{w}(t) = [U|\alpha(t)|^2 - w(t)]/\tau. \quad (2.18b)$$

D is the standard deviation of the noise. $\zeta(t) = (\zeta_1(t) + i\zeta_2(t))/\sqrt{2}$ accounts for noise in amplitude and phase. Here, ζ_1 and ζ_2 are both Gaussian white noise with zero mean and unit variance, i.e., $\langle \zeta_i(t) \rangle = 0$ and $\langle \zeta_i(t)\zeta_i(t') \rangle = \delta(t-t')$. In Fig. 2.7, we show a typical trajectory of the photon density $|\alpha|^2$, obtained by simulating Eqs. (2.18) using a fourth order Runge-Kutta algorithm. F and Δ are fixed in the bistable regime. As

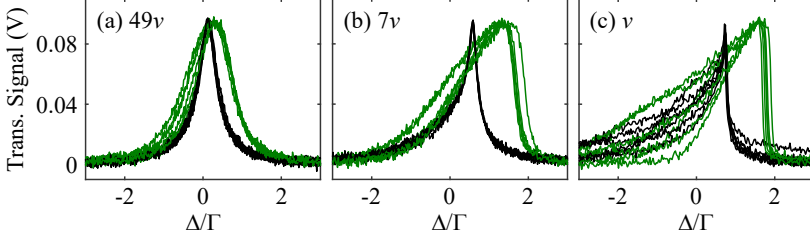


Figure 2.8: Single-shot measurements of dynamic hysteresis when Δ/Γ is scanned at a constant power $P = 150 \mu\text{W}$ and three different speeds: (a) $49v$, (b) $7v$, and (c) v . The slowest scanning speed is $v = 0.74 \mu\text{m/s}$. The driving conditions are the same as in Fig. 2.2.

indicated by the red line, the mean value of $|\alpha|^2$ randomly switches between two metastable states. The switching times are determined using a standard Matlab function. Given a trajectory x_1, x_2, \dots, x_N containing K changepoints, the function finds the set of $\{x_k\}$ changepoints that minimizes the cost function

$$J(K) = \sum_{r=0}^{K-1} \sum_{i=k_r}^{k_{r+1}-1} \delta(x_i; \chi([x_{k_r} \dots x_{k_{r+1}-1}])) + \beta K. \quad (2.19)$$

Here, x_{k_r} is the r th changepoint in the signal and $\chi([x_{k_r} \dots x_{k_{r+1}-1}])$ is the empirical estimate of the desired statistical property, in our case the mean, for the subtrajectory $x_{k_r} \dots x_{k_{r+1}-1}$. Furthermore, δ measures the square of the difference between a point x_i and $\chi([x_{k_r} \dots x_{k_{r+1}-1}])$, and β is a fixed penalty.

To obtain a large number of switching events, we performed simulations for 240 different realizations of the noise and combined the residence time statistics. In each of these simulations, the system evolved over a time $\Gamma t = 10^6$. Simulations were performed for two values of the thermal relaxation time: $\Gamma\tau = 10^{-2}$ and $\Gamma\tau = 20$. In both cases, we obtained more than $\sim 10^6$ switching events in total, thereby ensuring good statistics.

The time intervals between the switching events are known as the residence times $\tau_{\uparrow, \downarrow}^{(i)}$. These are the time intervals in which the system resides in either the high or the low density state. Figure 2.6(a) and Fig. 2.6(b) show the residence time distribution (RTD) in the lower metastable state for $\Gamma\tau = 10^{-2}$ and $\Gamma\tau = 20$. These two values of the thermal relaxation time result in exponential and peaked RTDs, which correspond to Markovian and non-Markovian dynamics, respectively.

2.8.4 Dynamic hysteresis influenced by fluctuations

Here we show the influence of noise on our dynamic hysteresis measurements. In Fig. 2.8, we plot single-shot hysteresis scans for the same three scanning speeds

considered in Fig. 2.3(a). For fast scans, Fig. 2.8(a) shows that the hysteresis cycle is only marginally affected by the noise. For intermediate-speed scans, Fig. 2.8(b) shows some differences from shot-to-shot. Finally, Fig. 2.8(c) shows pronounced shot-to-shot differences for slow scans. Despite the large differences from shot-to-shot in slow scans, our mean-field model neglecting fluctuations [Eq. (2.3)] qualitatively captures the observed behaviour in average dynamic hysteresis scans. The success of the deterministic model is evidenced by the good agreement between experiments and theory in Fig. 2.3 and Fig. 2.4. However, as Fig. 2.8 suggests, for slow scans noise plays an increasingly dominant role. This is the reason for which we restricted the scanning speed in our experiments to the range plotted in Fig. 2.4. We believe that the shot-to-shot deviations we observed in the hysteresis cycle are mainly due to the influence of colored noise in the detuning Δ . This colored noise results from mechanical fluctuations of our mirrors which have a high-frequency cutoff. At high speeds, however, the mechanical noise strength is negligible and only the noise in the laser remains.

Chapter 3

Observation of optical bistability and spontaneous symmetry breaking in a plasmonic grating inside a nonlinear waveguide

We investigate the response of a laser-driven metallic grating embedded in an oil layer with thermo-optical nonlinearity. At sufficiently large powers the laser transmission becomes bistable and self-sustained oscillations emerge in the diffracted intensities by the grating. Diffracted intensities by the -1 and $+1$ diffraction orders start to oscillate in-phase, out-of-phase, or become uncorrelated, all upon a $\sim 1\%$ variation of the laser power. Since the system and illumination are mirror-symmetric, the termination and onset of regimes with equal intensity radiated by the -1 and $+1$ diffraction orders correspond to spontaneous symmetry-breaking and symmetry-restoration transitions. Finally, we also demonstrate a regime in which the diffracted intensities show periodic spikes while the transmitted laser intensity oscillates in synchrony; the spikes are reminiscent of the firing of neurons and other excitable systems.

3.1 Introduction

Metallic nanostructures support surface plasmon resonances due to the collective oscillation of conduction electrons driven by the electromagnetic field. At the resonance frequency, optical energy can be strongly concentrated in deep-subwavelength nanoscale volumes [173]. The resultant local field enhancements have drawn great interest in various fields, including nonlinear optics [8] and related applications to imaging and biology [174]. Indeed, it has been widely disseminated that nanostructured noble metals have some of the largest third-order nonlinear susceptibilities $\chi^{(3)}$ of all naturally occurring materials at optical frequencies [2]. The large $\chi^{(3)}$ response of noble metals has been evidenced in various experiments involving harmonic generation [175, 176], two-photon luminescence [177], and four-wave mixing [178], for example. However, the simplest and most universal feature of continuous-wave coherent nonlinear optics — optical bistability — has never been realized using the $\chi^{(3)}$ response of noble metals. The reason for this is simple: despite being highly nonlinear, metals are also very lossy. It turns out that the losses (Joule heating) of noble metals are so strong that, at large laser intensities needed for bistability, metallic nanostructures melt or even explode [179] before displaying nonlinearities under continuous-wave illumination. Recall that, as explained in Chapter 1, the threshold power for observing optical bistability is determined by the ratio of the losses to the nonlinearity strength. Thus, the large nonlinearity of noble metals has been offset by the larger losses, except under pulsed excitation. Indeed, all nonlinear optical phenomena of coherently-driven nanostructured metals to date have involved pulsed excitation. An ultrashort optical pulse can provide a sufficiently high intensity for a short time (e.g., ~ 100 fs), thereby driving the metal to the nonlinear regime at low average power. Afterwards, the metal can cool until the next high-energy pulse arrives. In contrast, under continuous-wave illumination, the constant heating of the metal at moderately large average powers leads to its degradation.

While optical nonlinearities under pulsed excitation are interesting and useful in various areas, there are many applications for which continuous-wave nonlinearities are needed. Beyond the well-known relevance of optical bistability to switching and memories, several other applications of nonlinear resonant nanostructures and arrays thereof have emerged in recent years. For example, nonlinear gratings can be used for non-reciprocal light transport [180], and complex nonlinear optical systems can be used as neural networks for pattern recognition and information processing in general [181]. In view of these exciting recent developments, we decided to pursue the realization of optical bistability in an array of metallic structures, starting with a simple 1D grating. For the reasons explained above, we could not rely on the nonlinearity of the metal alone to achieve this. Therefore, we investigated a grating covered by oil, which has a strong thermo-optical nonlinearity as discussed in the previous chapter. In this context, we note that, to date, we know of a single experimental report of optical bistability in a plasmonic system [182]; the nonlinearity in that experiment is due

to a polymer on top of a metallic grating, and it is induced by a control beam in a pump-probe type configuration. In the ~ 16 years that have followed that publication, there has been no other experimental report of optical bistability in any resonant plasmonic system, even though research related to optical bistability has flourished in various photonic platforms [29, 41, 46, 105, 126, 154, 183–186] and there have been many theoretical/numerical works on optical bistability in plasmonic systems [187–190]. Moreover, in our view, the results in Ref. [182] provide insufficient evidence of bistability. The presence of a pump-induced nonlinearity and dynamic hysteresis for a probe beam is clear. However, as it is well known in the nonlinear dynamics community, a system can display dynamic hysteresis without bistability [191]. Therefore, the work in this chapter was motivated by the desire to realize what is, in our view, a clear demonstration of optical bistability in a periodic metallic system that is coherently driven at a single frequency. We reckon this as a first and decisive step towards realizing more complex systems, like metasurfaces, where functionalities can be derived from the interplay of nonlinearity and geometry.

This chapter presents experimental results obtained on a nonlinear one-dimensional metal grating driven by a continuous-wave laser. To realize a highly nonlinear response, we cover the grating by cinnamon oil. Beyond observing optical bistability, we demonstrate a variety of fascinating dynamical effects emerging as the laser power is varied in the nonlinear regime. In particular, we observe stable limit cycle oscillations of the diffracted intensities by the grating. Surprisingly, in certain regimes, sections of the intensity patterns radiated by the -1 and $+1$ diffraction orders oscillate out of phase or display random (possibly chaotic) behaviors. These behaviors are clear manifestations of spontaneous symmetry breaking (SSB), where a symmetric system suddenly ends in an asymmetric state. To the best of our knowledge, this is the first demonstration of SSB in any plasmonic system or grating. Finally, exploring the response of our grating in another regime, we discover spontaneous emergence of periodic spikes in the diffracted intensities. This behavior is reminiscent of excitable systems such as neurons.

3.2 Sample and linear response

Figure 3.1(a) shows a scanning electron micrograph of the aluminum grating we investigate in this chapter. The grating stands on a glass substrate, and comprises rectangular wires with 70 nm width, 90 nm height, and 366 nm lattice constant. The wires are 300 μm long, such that the sample can be considered effectively infinite along that direction. We chose the transverse dimensions and lattice constant to get a strong and narrow linewidth (for plasmonic standards) optical resonance due to the first order diffraction around 532 nm. This is the wavelength of our laser, and for which we have characterized the nonlinear optical response of oils as discussed in the previous chapter. Our theory collaborators, Jaime Abad Arredondo, Antonio I. Fernández Domínguez, and Francisco García Vidal (Madrid), performed a series of COMSOL simulations

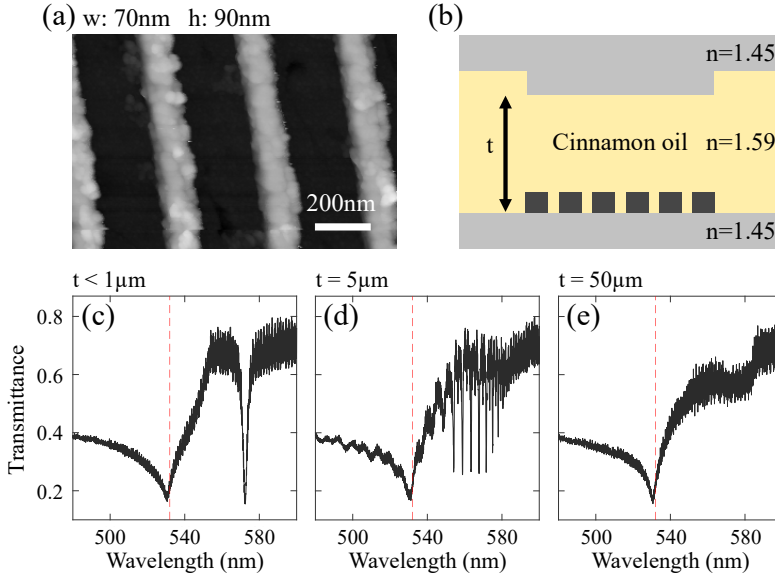


Figure 3.1: (a) Scanning electron micrograph of the aluminum grating on a glass substrate studied in this chapter. The grating’s wires have an average cross section that is 70 nm wide and 90 nm high. (b) Schematic of the plinth-oil-grating sample used for optical experiments, indicating the refractive indices of the various layers. (c,d,e) White light transmittance spectra for the grating in (a), covered by a layer of cinnamon oil with variable thickness t as indicated above each panel. The red dashed line in all three panels indicates the wavelength of the laser used in all nonlinear experiments discussed ahead.

which enabled us to determine these dimensions as optimal based on the desired spectral features and fabrication feasibility. The grating was subsequently fabricated by the AMOLF Nanolab technical staff using standard electron-beam lithography, electron-beam evaporation, and lift-off methods.

We covered the grating with a layer of oil to get a strong nonlinear optical response. We first used olive oil, as in the previous chapter. However, we found that the maximum power of our laser (~ 300 mW) was barely sufficient to reach optical bistability in our grating. We therefore replaced olive oil with cinnamon oil, since the latter has a stronger thermo-optical nonlinearity at 532 nm. The enhanced thermo-optical nonlinearity of cinnamon oil is mainly due to its stronger light absorption, which results in a greater temperature rise and refractive index change at a given laser power. This enhanced nonlinearity enabled us to reduce the threshold power for optical bistability by roughly a factor of two. The nonlinear refractive index of cinnamon oil is ~ 20 times larger than

that of olive oil, as estimated through measurements of nonlinear diffraction (not shown here) by other group members. However, the threshold for bistability is only reduced by a factor of ~ 2 in our experiments because the strong nonlinearity is associated with stronger absorption. Indeed, as explained in the introduction, the threshold power for bistability is determined by the ratio of the dissipation rate to the nonlinearity strength.

To keep the oil layer constant and control its thickness, we placed a glass plinth on top of the sample. The plinth has an area of $500 \times 500 \mu\text{m}^2$, which is larger than the grating area of $300 \times 300 \mu\text{m}^2$. A schematic of the full sample (substrate, grating, oil, and plinth) is shown in Fig. 3.1(b). We control the position and orientation of the plinth and grating using piezoelectric actuators. The actuators enable us to align the glass substrate and plinth parallel to each other, and to control the thickness t of the oil layer with nanometer precision.

We first discuss the linear response of our oil-covered grating. Figures 3.1(c-e) show linear transmittance spectra corresponding to three different thicknesses of the cinnamon oil layer. The sample is illuminated at normal incidence by a collimated white light beam from a halogen lamp. The incident light is linearly polarized perpendicular to the grating wires, i.e., parallel to the lattice vector. The transmittance is $T = (T_g - b)/(T_0 - b)$, with T_g the transmitted intensity through the full structure (substrate, grating, oil, and plinth), b the background intensity, and T_0 the transmitted intensity through the substrate, oil and plinth only. All intensities are wavelength dependent. We estimate the thickness t of the oil layer via the display of our calibrated closed-loop piezoelectric actuator, which we use to displace the grating along the optical axis. We define position ‘zero’ to be where the grating and plinth crash. This method is not very precise near the crashing point. Moreover, a tiny misalignment between the plinth and grating means that the layer thickness depends on the position in the plane of the grating. For these reasons, we can only specify an upper bound $t < 1 \mu\text{m}$ for the thinnest oil layer considered in Fig. 3.1(c). Moreover, the estimated values of t for thick waveguides ($t > 10 \mu\text{m}$) have an uncertainty of $\pm 3 \mu\text{m}$.

The transmittance dip observed around 530 nm for all three layer thicknesses in Figs. 3.1(c-e) corresponds to a lattice resonance. Its resonance wavelength is roughly given by the periodicity times the refractive index of the glass substrate, i.e., $366 \text{ nm} \times 1.45 = 531 \text{ nm}$. This suggests that the in-plane diffracted mode mainly resides in the glass substrate. While this is not ideal for maximizing the thermo-optical nonlinearity due to the oil, we will show that nonlinear optical effects still arise. Those effects are evidence of the finite overlap between the diffracted light field and the oil, since they never arise in the absence of oil. The resonances at longer wavelengths in Figs. 3.1(c-e) correspond to guided modes. These modes are confined to the oil layer, which has a larger refractive index of $n_{oil} \sim 1.59$ than the index $n_g \sim 1.45$ of the glass substrate and plinth. Light is in/out-coupled to these quasi-bound guided modes via diffraction from the grating.

Comparing Figs. 3.1(c-e) to each other reveals that the central wavelength, linewidth, and number of guided modes depends on t . This is the expected behavior

for guided modes. The trend in Figs. 3.1(c-e) shows that, as t increases, many narrow-linewidth guided modes are increasingly packed within the measured spectral range. The coupling efficiency into these modes progressively decreases as t increases, due to their decreasing overlap with the grating. For this reason, the magnitude of the corresponding transmission dips is reduced for the thickest waveguide in Fig. 3.1(e). Nonetheless, we note that many not-so-strong guided mode resonances still arise around the lattice resonance for the thicker waveguides.

3.3 Laser diffraction measurements in the linear regime

Apart from the transmittance spectrum, the guided modes are also observed in the reflection of a laser from the grating. Figures 3.2(a,b) show real and momentum space measurements, respectively, of the reflection of a 532 nm continuous-wave laser beam at normal incidence. The oil layer over the grating is 3 μm thick. The input laser power is ~ 10 mW, which is sufficiently low to ensure a linear response. We used a $20\times$ microscope objective with $NA = 0.4$ for excitation and collection. The collimated laser beam half-fills the back aperture of the objective and is focused onto the sample. We used a $f = 300$ mm Fourier lens and a $f = 1000$ mm tube lens for imaging in momentum and real space, respectively. Ahead, Fig. 3.4 illustrates a setup similar to the one used for these reflection measurements.

The real space measurements in Fig. 3.3(a) show two series of bright dots appearing symmetrically on the left and right sides of the direct reflection of the laser. We believe that the dots are guided modes which are outcoupled via diffraction from the grating. Our belief is based on two main observations. First, the role of diffraction is evident in that the bright dots are always aligned along the horizontal axis, i.e., parallel to the grating vector. No bright dots are ever observed in the vertical direction for our one-dimensional grating. Second, the horizontal positions of the dots in the camera depend on the waveguide thickness. In particular, a given pair of dots (at equal distance from the center) shifts towards the center of the image in synchrony when we gradually decrease the waveguide thickness. This is the expected behavior based on the dispersion relation of guided modes and the mirror symmetry of the diffraction grating.

While we cannot yet establish if each bright dot in Fig. 3.2(a) uniquely corresponds to a guided mode (or a superposition of modes), we can attribute with reasonable confidence *the series* of bright dots to the -1 and $+1$ diffraction orders. Figure 3.2(c) illustrates the mechanism by which we think the series of bright dots arise. The incident beam is diffracted by the grating into the oil layer at $\pm\theta$ angles. The diffraction angle is determined by the grating equation $\sin\theta = \lambda/(dn_{oil})$ where λ is laser wavelength, d is the grating constant, and n_{oil} is the cinnamon oil refractive index. The diffracted beams will traverse along the grating vector direction and reflect between two glass-oil interfaces. Each time they interact with the grating again, they will be out-coupled in

the normal direction and collected by the objective, resulting in a horizontally displaced set of bright dots imaged in real space.

Figure 3.2(b) shows the complementary measurement in momentum space, for the same system and laser power as in Fig. 3.2(a). Here, we observe vertical bright and dark bands on top of concentric circular fringes due to the reflected laser beam. The observed bands are actually conic sections, which only appear to be vertical because of the limited momentum range of our imaging apparatus. Figure 3.2(d) illustrates the physical mechanism by which these bands are formed. The figure shows cross-sections of the free-space, +1 diffraction, and -1 diffraction light cones, in glass and oil; these cross-sections are circles indicated by black curves. The location at which the cones are intersected, which determines the radius of the observed circles in Fig. 3.2(d), is taken at a frequency corresponding to our laser frequency. The guided modes are represented by the red circles residing in between the light cones in glass and oil. Based on a $3\ \mu\text{m}$ thickness for the oil layer, we plot 9 guided modes in Fig. 3.2(d). This number is consistent with our observation in Fig. 3.2(b). Due to Bloch's theorem, the periodicity of the grating results in a repeated pattern of the guided modes shifted by grating vectors \vec{G} in both positive and negative k_x directions. As a result, the guided modes become accessible to the numerical aperture of our objective, which is represented as the central black dashed line in Fig. 3.2(d). However, since the excitation laser beam half-fills the NA , we only excite the modes within the blue region. In this way, we can establish that indeed the stripes observed in Fig. 3.2(b) are the guided modes.

We note that our real and momentum space descriptions each only partially explain the observed phenomena. The real space description, based on treating the diffracted beams as rays, explains the horizontal displacement of bright dots in Fig. 3.2(a). However, it does not explain the relation between those dots and the guided modes in the oil layer. Conversely, the momentum space description in Fig. 3.2(d) relates the observed vertical bands in Fig. 3.2(b) to guided modes. However, the relation of those bands to the dots in real space is unclear. Detailed calculations or simulations accounting for all experimental conditions seem to be the only way to fully establish the origin of the various features. While this would be valuable, it is not crucial for the remainder of this chapter.

In the rest of this chapter, we focus on real space measurements for reasons that will become clear ahead. Moreover, we will investigate $30\ \mu\text{m}$ thick oil layer. For this thicker waveguide, the bright dots are further separated from the direct laser reflection. This will be convenient for nonlinear experiments presented ahead. In preparation for those results, Fig. 3.3 shows real space measurements like the one in Fig. 3.2(a) but now for the $30\ \mu\text{m}$ thick oil layer. Figures 3.3(a,b) show the two-dimensional reflected intensity distribution, and Figs. 3.3(c,d) show cuts of Figs. 3.3(a,b) integrated vertically within the region enclosed by the white dashed lines in Figs. 3.3(a,b). All these measurements were conducted using a laser power of 27 mW, which makes the system response approximately linear. Figures 3.3(a,c) and Figs. 3.3(b,d) are recorded 20 ms apart in time, under nominally identical conditions. We present two sets of

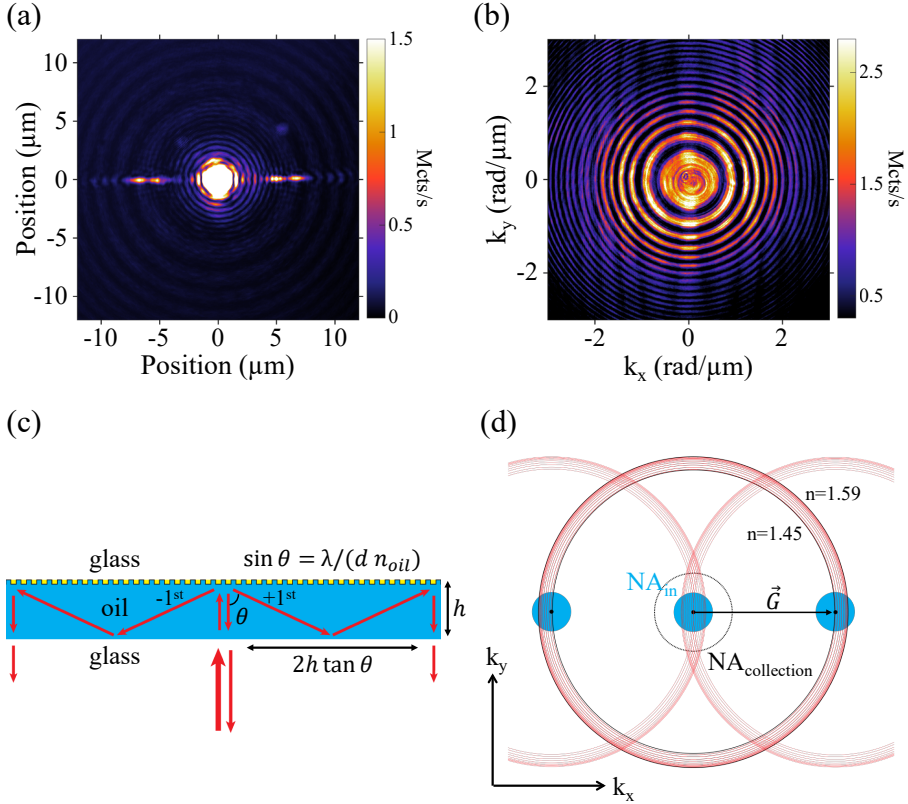


Figure 3.2: Reflection of a 532 nm continuous-wave laser beam normally incident on the oil-grating system, measured in (a) real image space and in (b) momentum space. The oil layer has 3 μm thickness. (c) Ray-tracing analysis to explain the displaced diffraction dots in (a). The angle θ is determined by the diffraction equation with λ the laser wavelength, d the grating constant, and n_{oil} the cinnamon oil index. (d) Momentum space calculation of guided modes in our oil layer and at our laser frequency. The red curves represent guided modes, which are bounded between the light cones in glass and oil. The center black dashed circle indicates the collection aperture of the objective NA . Blue circles indicate the excited momenta using our laser beam which half-fills the objectives.

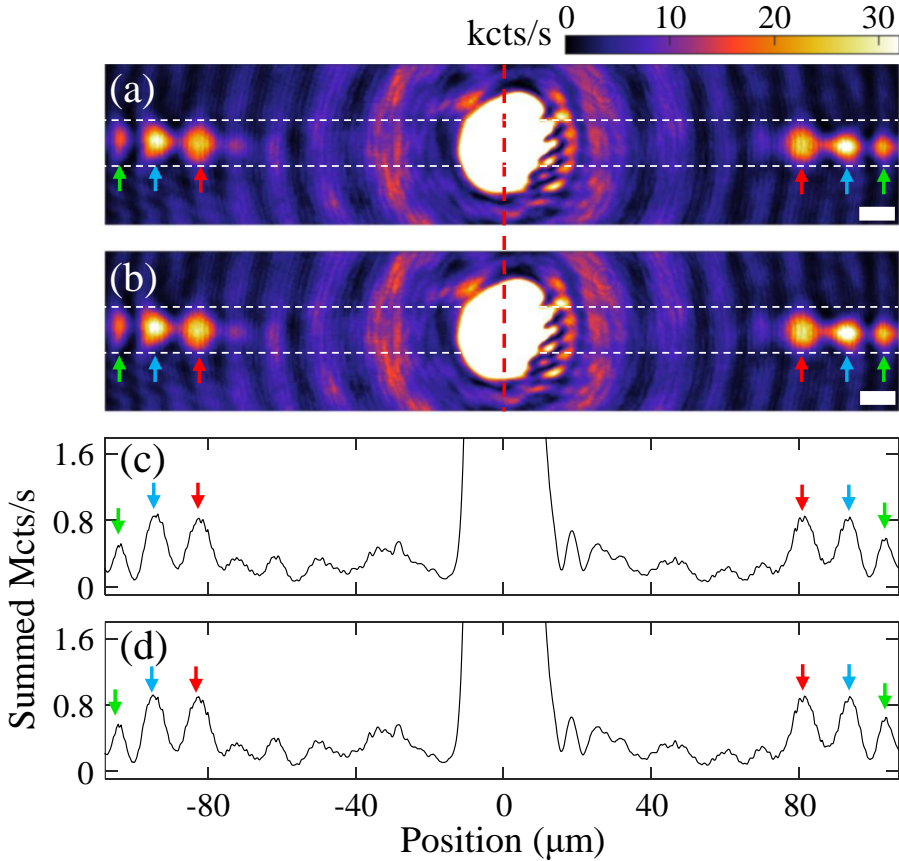


Figure 3.3: Measurements of the reflection of a 532 nm continuous-wave laser beam normally incident on the oil-grating system. The incident laser power is 27 mW, which is more than 5 times smaller than the threshold for bistability shown in Fig. 3.5. (a) and (b) are two reflected intensity distributions recorded 20 ms apart in time under nominally identical conditions. The white scale bars indicate 10 μm . (c) and (d) are obtained by integrating vertically the intensity within the regions enclosed by the white dashed lines in (a) and (b), respectively. The center bright spots in (a) and (b) correspond to the direct reflection of the laser beam. A series of bright dots positioned mirror-symmetrically around the central red dashed line are due to guided modes that are outcoupled via diffraction from the grating; see text for details on the interpretation of the dots. We use arrows of the same color (red, blue or green) to indicate pairs of dots located symmetrically about the mirror symmetry axis, indicated by red dashed lines in (a,b).

nominally identical measurements (instead of just one) to evidence the reproducibility of our results. While not shown here, we verified that the observed linear reflected intensity pattern is reproducible (within the limitations of the observed noise) across timescales of several minutes at least.

The measurements in Fig. 3.3 evidence the mirror symmetry of the reflected intensity pattern. The symmetry axis is indicated by the red dashed line in Figs. 3.3(a,b). Notice how the bright dots on the left and right side of the symmetry axis (e.g., the dots indicated by the colored arrows) have equal amplitudes and even mirror-symmetric shapes. In the next section, we will demonstrate how this mirror symmetry of the reflected intensity pattern can be spontaneously broken at sufficiently large laser powers. The data shown in Fig. 3.3 essentially serves as a reference to be compared with Fig. 3.6, where we will present a counterpart measurement in the nonlinear regime.

3.4 Setup for measuring intensity-dependent transmission and diffraction

Next we investigate the intensity-dependent transmission and diffraction of the 532 nm continuous-wave laser from our sample. For these experiments, we constructed the setup shown in Fig. 3.4. The laser intensity was time-modulated using a polarizing beam splitter and a half waveplate mounted on a motorized rotary stage. Another half waveplate was used to ensure that the incident light polarization was parallel to the grating vector. Two $10\times$ objectives ($NA = 0.25$) were employed for illuminating the sample with the laser and collecting the transmitted intensity. Before entering the objective, the laser beam had a diameter of 4 mm, which is less than the 10 mm aperture of the objective. Therefore, the laser beam was loosely focused onto the grating plane. The transmitted intensity was measured by a photodetector. In the reflection path, a flip mirror allowed to direct the reflected intensity into one of two different paths. One path led to a camera, used to obtain spatial information at a relatively low speed at 50 frames/second. This is the same camera used to acquire the measurements in Fig. 3.2 and Fig. 3.3. The other path led to a setup with two arms, each containing a photodetector for fast (up to 50 MHz) measurements. These photodetectors recorded the diffracted light intensity, which is similar to the bright dots in Fig. 3.2 and Fig. 3.3 but emerge in the nonlinear regime as will be described in the next section. To spatially isolate the dots, we create two intermediate image planes where we place two pinholes for signal selection. The area of the reflected intensity pattern selected by the pinholes is shown ahead.

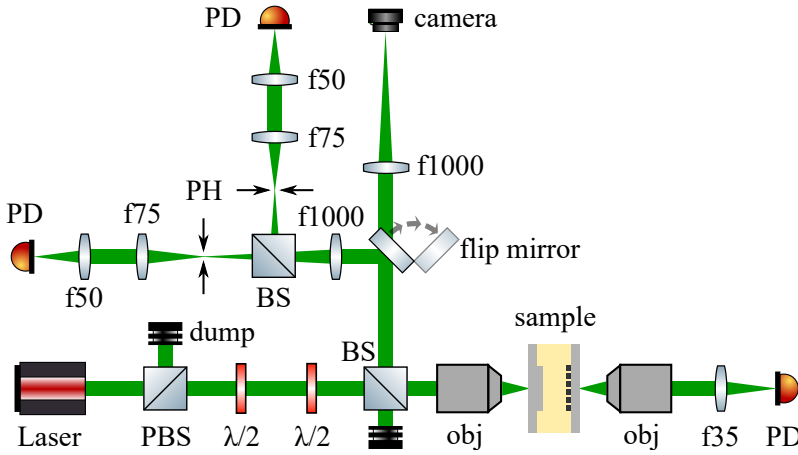


Figure 3.4: Schematic of the optical setup used to measure the intensity-dependent transmission and diffraction of laser light from our sample. PBS is polarizing beam splitter; BS is beam splitter; obj is objective; PH is pinhole; PD is photodetector; $\lambda/2$ is half waveplate. The laser intensity is modulated by the PBS and $\lambda/2$. Another $\lambda/2$ is used to ensure that the input laser is linearly polarized parallel to the grating vector before entering the objective. The laser transmission is measured by a PD. The flip mirror allows sending the reflected intensity either to a camera or to a two-arm setup with photodetectors.

3.5 Optical bistability and emergent spatial patterns

Figure 3.5 shows typical results obtained in transmission and reflection (using the camera) when scanning the laser power up and down within 5 seconds. The thickness of the oil layer is $30\ \mu\text{m}$. Figure 3.5(a) shows time traces of the input power and transmitted power, respectively. Notice the switch at 2.39 s from a high transmission state to a low transmission state. The abruptness of the switch indicates a sudden transition between two stable states (i.e., the existence of bistability), beyond the obvious existence of optical hysteresis. To show the bistability more clearly, in Fig. 3.5(c) we plot the transmittance versus the input power. Black and green curves correspond to increasing and decreasing the input power, respectively. Clearly, the transmittance switch leads to a wide bistability range and a large optical hysteresis when the input power is decreased. We also observe an overshoot right after the transmittance switch; see Fig. 3.5(b). The overshoot is due to the finite thermal relaxation time of the oil, as discussed in the previous chapter. The half width at half maximum of this overshoot ($60\ \mu\text{s}$) is longer than in the oil-filled micro-cavity ($16\ \mu\text{s}$), presumably because of the larger optical mode volume in the oil-covered grating system. The transmittance in Fig. 3.5(c) also

displays a weak modulation as a function of the input power, which is most visible at low input powers. We are unsure about the origin of this effect. However, since the frequency of this weak modulation increases with the thickness of the oil layer (measurements not shown here), we suspect that it is due to an etalon effect in the oil layer.

Figures 3.5(d,e) show real space reflection images observed right before and after the transmittance switch, displaying remarkable discrepancy. Before the switch, Fig. 3.5(d) shows a simple circular pattern due to the direct reflection of the laser beam; the bright dots from Fig. 3.3 are absent because they are positioned far from the direct reflection (center spot) due to the thick waveguide and are therefore outside of the field of view of the objective. After the switch, Fig. 3.5(e) shows a more complex pattern. The new pattern comprises a series of rings and bright dots, as before, symmetrically located on the left and right sides of the directly reflected beam. This complex pattern evolves as the laser power first increases and then decreases. However, the general structure (rings plus dots) remains the same until the end of the hysteresis loop at low powers, where the system transitions back to the initial state with high transmittance. As before, we attribute the newly emerged bright dots to guided modes which are outcoupled via diffraction from the grating.

Beyond the two snapshots of the reflected intensity pattern presented in Figs. 3.5(d,e), we recorded a series of reflection images throughout the full hysteresis cycle. The exposure time for each image was 20 ms, and the camera acquisition rate was 50 frames/seconds. In this series of measurements, we observed that the bright dots in the nonlinear regime blinked at various times after the high-to-low transmittance switch. The dots suddenly brightened or darkened, sometimes in unison and sometimes not, as the input power slowly changed. For example, Figs. 3.6(a,b) show two consecutive frames where the relative intensity of the same two dots changes abruptly. In Fig. 3.6(a) the two dots highlighted by the green arrows have roughly equal intensity. In contrast, in Fig. 3.6(b) the right dot is suppressed while the left dot remains practically the same. This abrupt change in relative intensity can also be seen in the cuts shown in Figs. 3.6(c,d). The green arrows, serving as reference, are at the same horizontal positions as in Figs. 3.6(a,b).

The large intensity difference between the two dots in Fig. 3.6 is surprising based on the symmetry of the illumination and of the grating. Based on the description in Fig. 3.2(c), we will refer the dots on the left and right sides of the direct reflection as the diffracted intensities by the -1 and $+1$ diffraction orders, respectively. The excitation momentum wavepacket is symmetric around $k_m = 0$. The grating wires have mirror symmetry, meaning that the grating is not blazed. Furthermore, the oil layer is translationally invariant in the plane of the grating. Hence, the power radiated at positive and negative momenta should be equal. Equal diffracted intensities by the -1 and $+1$ diffraction orders are indeed our observation in the linear regime (e.g., Fig. 3.3). A small difference between -1 and $+1$ diffracted intensities can still arise because of imperfections in the grating, misalignments (e.g., of the excitation beam

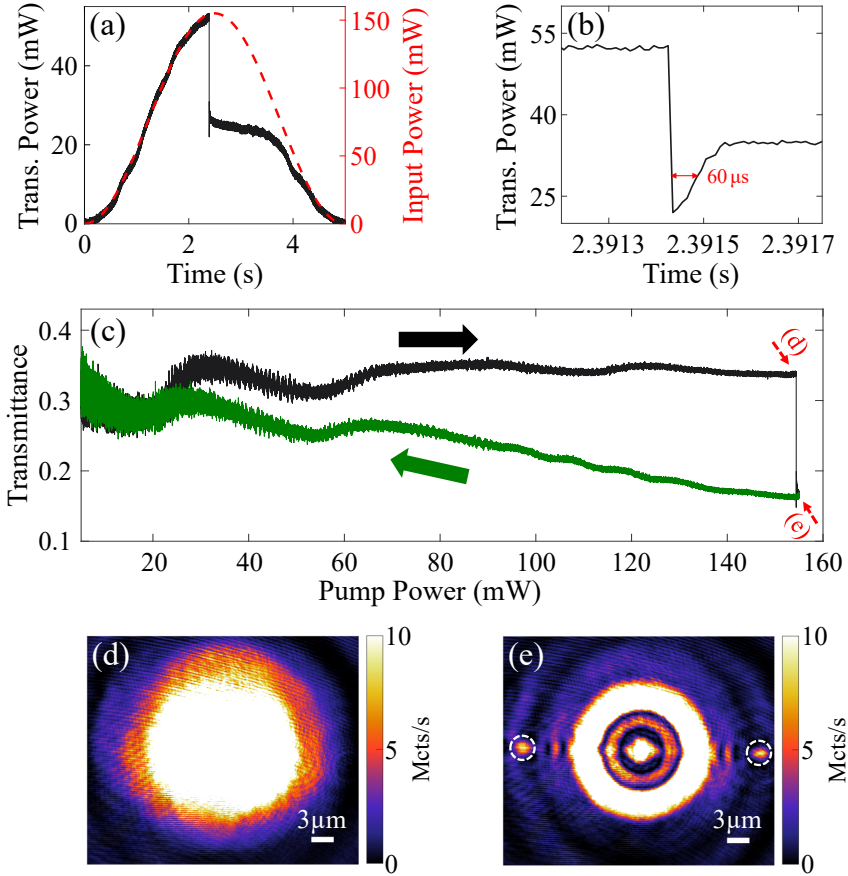


Figure 3.5: (a) Time traces of input and transmitted laser powers. The switch at ~ 2.39 s from a high to a low transmittance state leads to optical bistability and hysteresis when reversing the direction of the input power scan. (b) a zoom-in view of (a) right after the bistable switch around 2.3915 s, showing an overshoot of 60 μ s. (c) Transmittance as a function of the input power. Black and green curves correspond to increasing and decreasing the input power, respectively. (d) and (e) are reflection images recorded by a camera before (d) and after (e) the switch, as indicated in (c).

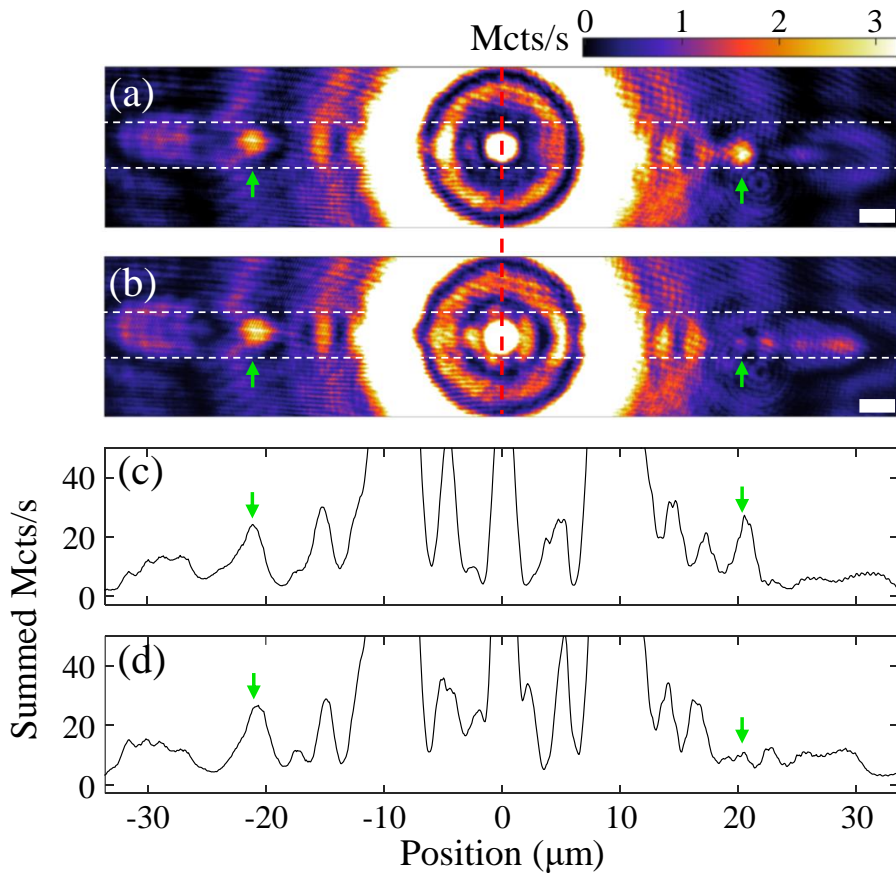


Figure 3.6: (a,b) Two consecutive measurements of the nonlinear reflected intensity pattern. The exposure time for each image is 20 ms, and the image in (b) is recorded immediately after the one in (a). The scalebars indicate 3 μm . (c) and (d) are obtained by vertically integrating the intensity within the region enclosed by the white dashed lines in (a) and (b), respectively. Green arrows serve as references for indicating the locations of bright dots.

or of the plinth), and/or differences between the optical paths. However, the mirror symmetry of our linear measurements in Fig. 3.3 demonstrates that such effects are marginal at most. Only in the nonlinear regime we observe major differences in the radiated power by the -1 and $+1$ diffraction orders. In particular, the mirror symmetry of the reflected intensity pattern is spontaneously broken as a function of the input power. In the following, we will show that the nonlinear grating-waveguide system actually undergoes a series of bifurcations where mirror symmetries are spontaneously broken and restored.

3.6 Dynamics of (a)symmetric diffraction efficiency of a nonlinear grating

The symmetry breaking observed in two consecutive frames in Fig. 3.6 suggests that the relevant dynamics are faster than the camera acquisition rate. For this reason, we constructed the two-arm setup shown in Fig. 3.4. To isolate the diffracted intensities from the two equivalent dots corresponding to the -1 and $+1$ diffraction orders, we first split and then imaged the reflected light at two different planes. At each image plane, we placed a $150\ \mu\text{m}$ diameter pinhole. The pinholes were co-centered with the intensity maxima of two dots. The correct locations of the pinholes were established and verified using additional flip mirrors and cameras not shown in Fig. 3.4. The dashed circles in Fig. 3.5(e) indicate the diameter of the pinholes at the aforementioned image planes. Since the dashed circles are only slightly wider than the intensity peaks inside, the signals of interest were well isolated from other signals. Finally, each arm in the setup ends in a 50 MHz photodetector. These allow to measure the optical dynamics a million times faster than with the camera used to record the images in the previous section.

Figure 3.7 shows the time trace of the transmittance as a black curve, and of the diffracted intensities by the -1 and $+1$ diffraction orders as purple and orange curves, respectively. The data in Fig. 3.7(a) is the same as in Fig. 3.5(c), but plotted as a function of time to ease comparison between Fig. 3.7(a) and Fig. 3.7(b). The upper curve in Fig. 3.7(b) is vertically displaced for clarity. Before the switch, when the grating is in the high transmittance state, the two diffracted intensities display qualitatively similar (not same) slow dynamical effects. We attribute the different ripples in the diffracted intensities between 1 s and 2 s to inhomogeneities in the oil layer induced by the laser absorption. Recall from Fig. 3.5(c) that the transmittance is weakly modulated at low laser powers. Based on our observations (not shown) for various thicknesses of the oil layer, we attribute that weak modulation to an intensity-dependent etalon effect. That modulation, coupled to tiny imperfections in the system (e.g., slightly tapered oil waveguide), results in slow density variations within the oil layer. These variations explicitly break the symmetry of the diffracted intensities by the -1 and $+1$ diffraction orders. An imperfect alignment of the pinholes and of the optics, i.e., explicit symmetry

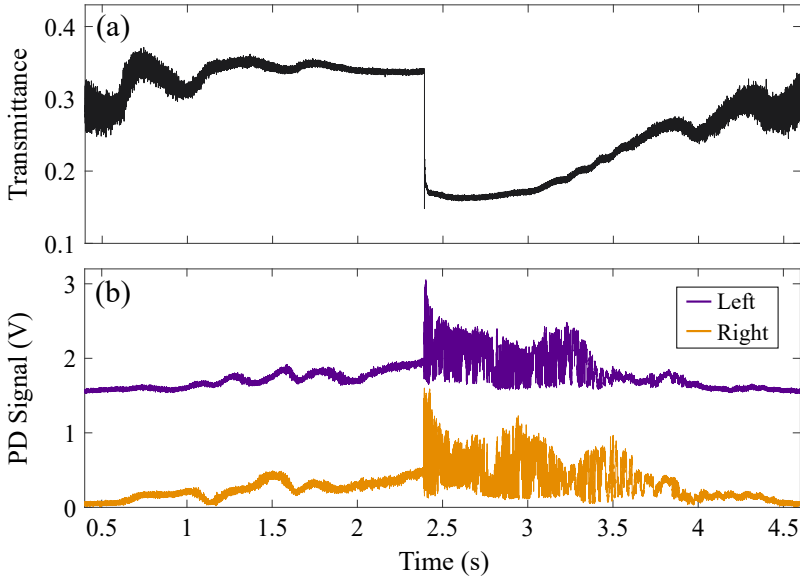


Figure 3.7: Time traces of the (a) transmittance, and (b) diffracted intensity by the -1 and $+1$ diffraction orders as purple and orange curves, respectively. All three time traces are recorded simultaneously. After the system switches to the low transmittance state, signals in (b) display fast dynamics with qualitative changes in behavior within short times. Figure 3.8 presents zoom-in view of three dynamical regimes after the transmittance switch.

breaking in the detection rather than in the system, could also explain the intensity differences observed in Fig. 3.7(b). However, below we evidence the nearly perfect mirror symmetry of the same system on short timescales using the same setup. This indicates that detection asymmetries due to the pinholes and/or optics are marginal at most, and that system asymmetries are very small and only relevant on long time (e.g. ~ 1 s) scales.

After the grating switches to the low transmission state, the two diffracted intensities display dramatically different dynamics. Figure 3.8 zooms into three representative time windows of the data in Fig. 3.7(b). Each time window is 15 ms, which is less than the inverse acquisition rate of the camera. Within these time windows, the average input power changes linearly with time by less than 0.3%, which is roughly equal to the standard deviation of the laser noise. Therefore, the average input power is effectively constant within each time window.

The three plots in Fig. 3.8 demonstrate qualitatively different regimes. Figures 3.8(a,c) display periodic oscillations of the diffracted intensities by the -1 and

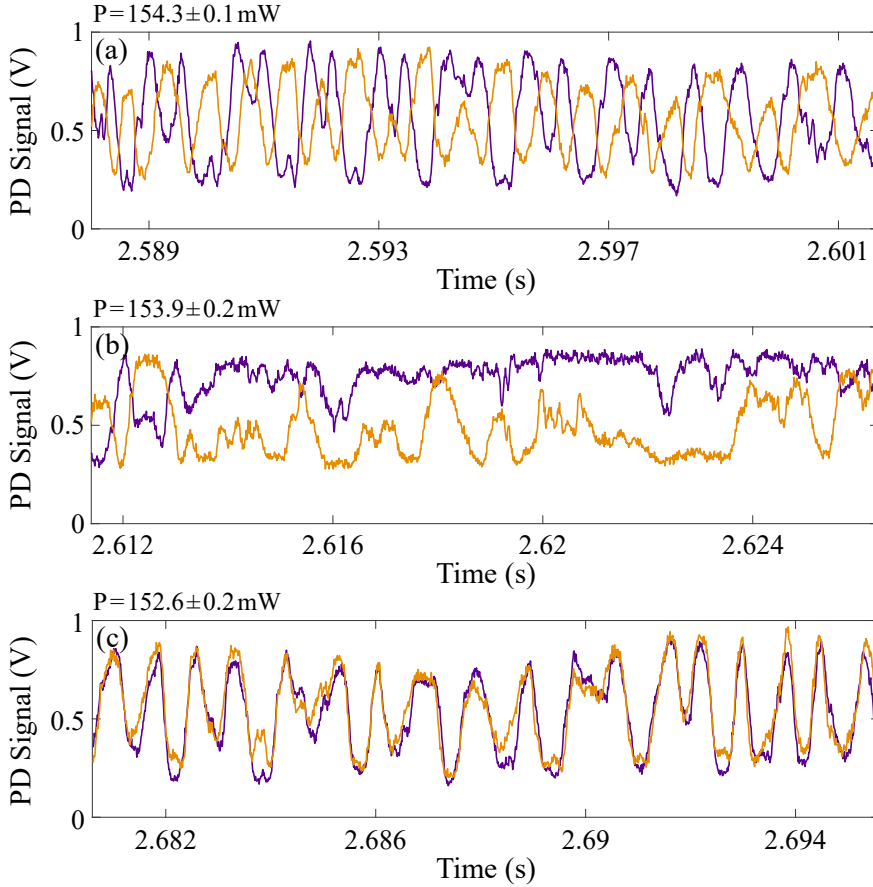


Figure 3.8: Zoom-in views of Fig. 3.7(b) at three time windows with equal time span (15 ms), showing distinct dynamical regimes for the diffracted intensities within the two dashed circles in Fig. 3.5(e) : (a) out-of-phase dynamics; (b) uncorrelated dynamics; (c) in-phase dynamics. The center power for each time window is labelled on the top-left of each panel. As we use a symmetric excitation scheme, (a) and (b) correspond to a symmetry-breaking regime, while (c) corresponds to a symmetry-preserving regime.

+1 diffraction orders. These types of oscillations are known as limit cycles. Since the laser power sustaining these oscillations is not modulated, they are called self-sustained oscillations. The oscillation period is associated with (but not equal to) an intrinsic time scale of the system, namely the thermal relaxation time. To the best of our knowledge, this is the first observation of limit-cycle oscillations in any plasmonic system.

The intensities at the two dots due to the -1 and $+1$ diffraction orders oscillate in phase in Fig. 3.8(a), but out of phase in Fig. 3.8(c). The former evidences a full synchronization of the diffracted intensities by the -1 and $+1$ diffraction orders. This synchronization, while non-trivial and its origin is not well understood, respects the mirror symmetry of the system as expected. Notice also that the two intensity curves practically overlap throughout the entire time window in Fig. 3.8(c). This evidences the good alignment of the setup and of the pinholes. Upon misalignment (not shown), the oscillation amplitudes are actually different.

Figure 3.8(c) shows the diffracted intensities by the -1 and $+1$ diffraction orders oscillating out of phase. Out-of-phase limit cycle oscillations do not respect the mirror symmetry of the system, illumination, and detection. Thus, their spontaneous emergence upon changing the input power is direct evidence of spontaneous symmetry breaking. To the best of our knowledge, this is the first observation of spontaneous symmetry breaking in any diffraction grating or plasmonic system. It is also noteworthy that the oscillation period in Fig. 3.8(a) is different from that in Fig. 3.8(c), the latter being roughly twice longer. This change of period is indicative of period-doubling and period-halving bifurcations of nonlinear dynamical systems [192]. At such bifurcations, a symmetry is broken or restored and the period of limit-cycle oscillations changes. Even simple, single optical mode, nonlinear dynamical systems with non-instantaneous nonlinearity (as due to the thermal relaxation time of the oil in our system) have been predicted to display cascades of bifurcations where the period of stable limit cycles changes [33]. Thus, similar behavior can be expected in our more complex system.

Figure 3.8(b) also displays a surprising behavior: no correlation between the two diffracted intensities by the -1 and $+1$ diffraction orders. The time window in Fig. 3.8(b) is shortly after the one in Fig. 3.8(a). Thus, a small change in input power (related to time) leads to qualitatively different behavior. We believe that the random and uncorrelated dynamics in Fig. 3.8(b) are due to chaos. While we currently have no formal way to distinguish between chaos and ‘just noise’ in these short time traces which are certainly influenced by noise, the fact that they emerge between two regimes of stable limit cycles is a strong indication that they are due to chaos. Indeed, it is well known that nonlinear dynamical systems can undergo cascades of period-doubling bifurcations leading to chaos. Conversely, period-halving bifurcations can lead a system from chaos to stable limit cycles, i.e., order emerges from disorder through small parameter changes. Indeed, the series of measurements in Fig. 3.8 demonstrate how order can emerge from disorder and viceversa upon small changes in driving power. Further experimental and theoretical research is needed to establish the exact nature of these various dynamical regimes.

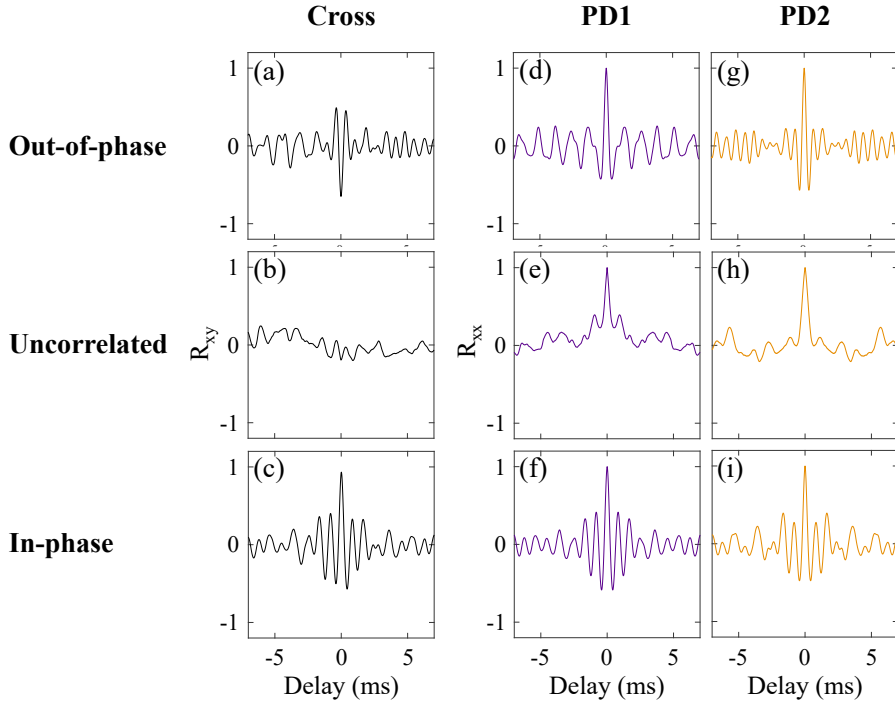


Figure 3.9: Cross-correlation functions as a function of delay based on data in Fig. 3.8 for (a) out-of-phase, (b) uncorrelated, and (c) in-phase regimes. Auto-correlation functions as a function of time delay for -1 and $+1$ signals for (d,g) out-of-phase, (e,h) uncorrelated, and (f,i) in-phase regimes. We use a normalization method such that the value 1 (-1) correspond to correlation (anti-correlation). Based on this method, a value of 1 is always obtained for all auto-correlation functions in (d-i).

In Fig. 3.9 we present a more detailed analysis of the data in Fig. 3.8. We calculate normalized cross- and auto-correlation functions for the diffracted intensities by the -1 and $+1$ diffraction orders. We choose a normalization method such that the value 1 (-1) corresponds to perfect correlation (anti-correlation). Details on the algorithm for calculating the cross- and auto-correlation functions can be found in Appendix 3.9.1. Figures 3.9(a-c) show the cross-correlation functions R_{xy} as a function of time delay for the in-phase, uncorrelated and out-of-phase regimes corresponding to Fig. 3.8(a-c) respectively. As expected, we observe: (i) a pronounced dip at zero time delay in Fig. 3.9(a), indicating anti-correlation; (ii) no obvious peaks or valleys at any time delay in Fig. 3.9(b), indicating no correlation; (iii) a strong peak at zero time delay in Fig. 3.9(c), indicating correlation. Figures 3.9(a,c) also show oscillatory behavior with decaying envelopes. The peaks (valleys) at small delays in Figs. 3.9(a,c) correspond to delays of a multiple or half-multiple of oscillation periods for the in-phase and out-of-phase regimes respectively. The decaying envelopes suggest that the similarity between the two compared data vanishes for long time delays.

Figures 3.9(d-f) and Figs. 3.9(g-i) show auto-correlation functions R_{xx} as a function of the time delay for -1 and $+1$ signals for the in-phase, uncorrelated and out-of-phase regimes. The same color code for the -1 and $+1$ signals as in Fig. 3.7 and Fig. 3.8 are used. Due to the normalization method, a value of 1 is always obtained at zero time delay for these plots. Also, note that a positive time delay is equivalent to the counterpart negative time delay with the same absolute value when calculating the R_{xx} . Therefore, all auto-correlation functions are mirror-symmetric around zero time delays. For the out-of-phase and in-phase regimes, the auto-correlation functions in Figs. 3.9(d,g,f,i) also display oscillations as in Figs. 3.9(a,c) for the same aforementioned reason. For the uncorrelated regime, Figs 3.9(e,h) show single narrow peaks at zero time delays and the auto-correlation functions quickly decay within ~ 0.3 ms; this is the expected behavior for delta-correlated signals.

Finally, we provide some interpretations on the diffracted intensities by the -1 and $+1$ diffraction orders. As mentioned in Section 3.3, it is not clear how these bright dots in real space image are related to the guided modes in the oil layer. However, based on the observed effects and basic setup information presented in this section, we can propose plausible interpretations. First, note that a thick waveguide ($30 \mu\text{m}$) was used in the measurements. For this thickness, the total number of modes supported by the waveguide is roughly 75 for one polarization (our laser is polarized). As a result, one may expect excitation of many modes, according to the momentum distribution of the incident laser. Based on this expectation, one might believe that the bright dots are due to the superposition of many modes in real space. However, our observation of the sinusoidal limit cycles makes that interpretation very unlikely. In Fig. 3.8 we observed nearly perfect sinusoidal oscillations for isolated single dots. If those single dots corresponded to superpositions of many guided modes, one would expect a complex non-sinusoidal waveform due to the beating of many modes. Another interpretation, albeit a highly unlikely one in our view, is that many (orthogonal) modes

all spontaneously begin to oscillate sinusoidally and in phase. Thus, based on our observations in this section, it seems to us that the most plausible explanation is that the dots correspond to single modes. Nonetheless, further research is needed to establish the exact nature of the dots.

3.7 Spontaneous oscillations

The results in the previous section motivated us to investigate the dynamics of our system for various waveguide thicknesses and laser powers. Unfortunately, variations in laser power induced slow changes (on the time scale of several minutes or longer) in the oil layer, which we could not control despite our best efforts. These slow changes prevented us from getting an extensive and consistent data set across a wide parameter range. Nonetheless, in this section we present results obtained for a waveguide thickness of $50\ \mu\text{m}$ when ramping the laser power up and then parking it at a constant large value. Our aim in presenting these results is simply to illustrate the fascinating nonlinear dynamics that can emerge in our oil-covered grating in certain cases. To the best of our knowledge, the phenomena here reported have never been observed in any plasmonic system or diffraction grating.

Figure 3.10(a) shows time traces of the transmittance and diffracted intensities by the -1 and $+1$ diffraction orders, using the same color code as in Fig. 3.7 and Fig. 3.8. Black and purple curves are vertically displaced for clarity. These measurements were obtained by increasing the laser power from 0 to 129 mW in 1.3 s, and keeping it at 129 mW for the rest of the measurement. Notice in Fig. 3.10(a) that, at 4.45 s which is more than 3 s after the end of our protocol, the transmittance spontaneously switches to a lower value. A similar transmittance switch was observed in the previous section, and associated with the threshold for accessing the bistable regime. Here, however, we observe a relatively long waiting time for the switch to occur after the mean laser power and transmittance are fixed. We think that this waiting time is due to the laser power being very close, but not quite enough, for the system to deterministically change state. Hence, the system needs to wait (a random time) for a fluctuation in the absorbed laser power to trigger the switch.

Immediately after the switch, the transmittance remains at a constant value. This is similar to what we observed in Figs. 3.5(a,c) and Fig. 3.7(a). However, after a second random waiting time, a fluctuation occurs and all three observables start to oscillate shortly after. The fluctuation triggering these oscillations can be observed in the zoom-in view presented in Fig. 3.10(b); see the transmittance slightly before 5.16 s. After this fluctuation, the transmittance gradually increases until it starts to spontaneously oscillate with a sawtooth waveform around 5.183 s. Concomitantly, the diffracted intensities by the -1 and $+1$ diffraction orders begin to display periodic spikes in synchrony with the transmittance minima. This spike train is qualitatively different from the sinusoidal oscillations shown in Fig. 3.8(c) in the previous section. We are unsure of the origin of the spikes. However, it is worth mentioning that similar

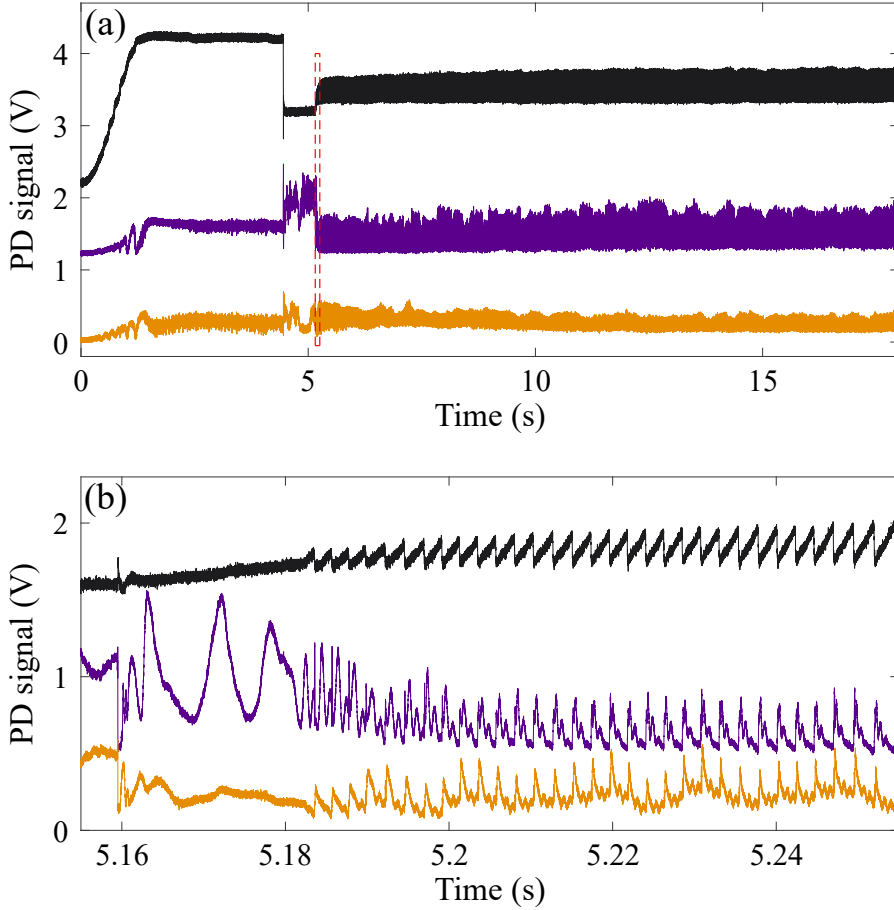


Figure 3.10: (a) Time traces for the laser transmittance (black), and diffracted intensities by the -1 (purple) and $+1$ diffraction orders (orange) as indicated by the white dashed circles in Fig. 3.5(e). Black and purple curves are displaced vertically for clarity. The driving protocol consists of increasing the laser power from 0 to 129 mW in 1.3 s, and keeping the power constant at 129 mW thereafter. (b) Zoom into (a), centered around 5.2 s. Notice the tiny perturbation in the transmittance around 5.16 s, after which the transmittance gradually grows. After this growth time, all three observables begin to oscillate. The incident laser power is unmodulated during the entire time of the oscillations, meaning that these are self-sustained oscillations.

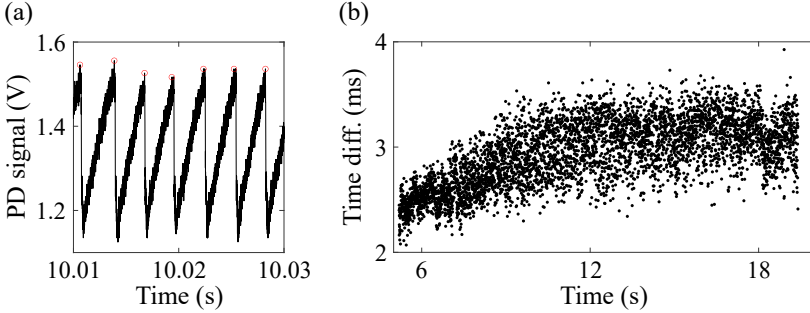


Figure 3.11: (a) A zoom-in view of the transmittance time trace in Fig. 3.10(a). The red circles indicate peaks of all displayed cycles, which are determined by the standard peak-finding algorithm in MATLAB. (b) Time difference between consecutive peaks as a function of time.

spiking behavior is characteristic of excitable systems such as neurons. It has therefore occurred to us that the oil-grating system may have a narrow regime of excitability above the bistability. Unlike bistability, excitability is associated with a single stable state. Periodic spikes emerge when the system is excited, and makes excursions in phase space across an unstable point.

Interesting aspects of the observed self-sustained oscillations are their duration and robust period. We have observed such oscillations for more than 30 s, while the period is ~ 3 ms. Since the observation time was simply limited by the memory of our electronics, we suspect that the oscillations may continue for even longer time than our measurement limit. In Fig. 3.11, we analyze the robustness of the period in more detail. Figure 3.11(a) shows a zoom-in view of the transmittance time trace, with red circles indicating the peak of each cycle. The peaks were identified using a standard peak finding algorithm in MATLAB. In Fig. 3.11(b) we plot the time difference between consecutive peaks as a function of time. Each black dot corresponds to one cycle, and its position in time is mid-way between consecutive peaks. The data in Fig. 3.11(b) can be regarded as a running histogram or probability density function. Within a reasonably large time bin (e.g., ~ 0.5 s), regions with a high density of black dots correspond to the running average of the periods. Interestingly, Fig. 3.11(b) shows that the oscillations have a build-up time (of unknown origin) of about 7 seconds. During this time, the period grows from ~ 2.3 to ~ 3.2 ms. After the build-up time, the period stabilizes at ~ 3.2 ms and the oscillations persist indefinitely.

Finally, we would like to comment on the reproducibility of the experiments in Fig. 3.10 and Fig. 3.11. We performed these experiments many times, using nominally identical ramps and a fixed grating-waveguide system. However, the oscillations emerged some of the times only. When the oscillations emerged, the shape of all three waveforms and the period were practically the same as here reported. We strongly

believe that the limited reproducibility of this behavior is due to an intrinsic feature of nonlinear dynamical systems. In particular, nonlinear systems display an extreme sensitivity to parameter changes within bifurcation cascades [192]. Changing the value of one parameter (e.g., laser power or waveguide thickness) by less than 0.1% can result in major qualitative changes to the phase space structure. Indeed, systems can transition between limit cycles and chaos within extremely narrow parameter changes, even in simple low-dimensional (e.g., three degrees of freedom) nonlinear systems. This extreme sensitivity to parameter changes, combined with experimental imperfections, may be the reason for which we could only reproduce the same behavior in some but not all measurements. Nonetheless, we think it is important to report this fascinating behavior which may appear in other systems or parameter regimes in a more controlled fashion. Excitable behavior could open the door to using oil-covered extended systems, like gratings or metasurfaces, for neuromorphic computing or information processing. Indeed, the ability to display self-sustained oscillations is one of the key features of many information-processing systems.

3.8 Conclusion

In summary, we demonstrated various dynamical regimes in the nonlinear response of an oil-covered metallic grating driven by a continuous-wave laser. Our first result was the observation of optical bistability in the laser transmission through the grating. The most surprising results were found after crossing the bistability threshold. Monitoring the diffracted intensities at opposite angles from the normal to the plane of the grating, we discovered self-sustained oscillations wherein the diffracted intensities by the -1 and $+1$ diffraction orders can oscillate in-phase or out-of-phase. We also found regimes in which the diffracted intensities by the -1 and $+1$ diffraction orders are uncorrelated. Given that our symmetric system (by design) is driven symmetrically ($k_{in} = 0$), out-of-phase and uncorrelated dynamics by the -1 and $+1$ diffraction orders indicate the breaking of a mirror symmetry for the diffraction efficiency. The regime of uncorrelated dynamics observed between two stable limit cycle regimes is likely associated with chaos. Indeed, the co-existence of intermittent periodic windows and chaos is common within bifurcation cascades. Finally, in another regime we discovered periodic spikes emerging spontaneously in the diffracted intensities by the -1 and $+1$ diffraction orders. These spike trains emerge concomitantly with periodic saw-tooth oscillations in the transmission.

Further experimental and theoretical studies are needed to establish the origin of the various dynamical regimes evidenced in this chapter, and to possibly identify new dynamical regimes through a more thorough scan of parameters. On the experimental side, there is room for improvement in the level of control over the system. A better control would enable a more careful characterization of the cascades of bifurcations leading to the emergence and termination of limit cycles with different periods. To achieve this, a more robust/reliable mechanical architecture for controlling the wave-

uide thickness would be helpful. In addition, a feedback-based control system for reducing laser noise could also help. Despite these possible improvements, our results have demonstrated the potential of oil-covered gratings as a new platform to study nonlinear dynamics. The nonlinearity-grating scheme used in this chapter is readily adaptable to other plasmonic/metasurface systems, which paves the way to study more complex phenomena emerging from the interplay of nonlinearity and geometry. We believe that such complex systems could be applied to realize intensity-controlled wavefront shaping, or as neural networks for pattern recognition or other machine learning tasks.

3.9 Appendices

3.9.1 Details on the algorithm for calculating cross- and auto-correlation functions

Given two real one-dimensional data vectors, X and Y , of the same length M , we calculate the raw cross-correlation function as a function of index delay m without any normalization as:

$$R_{xy,raw}(m) = \begin{cases} \sum_{n=0}^{M-m-1} [X(n+m) - \bar{X}] * [Y(n) - \bar{Y}], & \text{for } m \geq 0, \\ R_{yx,raw}(-m), & \text{for } m < 0. \end{cases} \quad (3.1)$$

Note that in this definition of cross-correlation we subtract the mean values, \bar{X} and \bar{Y} , of the two vectors from $X(n+m)$ and $Y(n)$, respectively, before the multiplication. This definition is more generally referred to as cross-covariance. In signal processing, the two terms, i.e., cross-correlation and cross-covariance, are interchangeable.

The raw auto-correlation function is acquired by setting $Y = X$ in Eq. (3.1). Also, if the signals are time series, the time delay is computed by multiplying the index delay m by the time step used in the measurement.

As mentioned in Section 3.6, we use a normalization method such that the auto-correlation function at zero time delay is always 1. This is achieved by applying a normalization factor to the raw cross-correlation functions:

$$R_{xy}(m) = \sqrt{\frac{1}{R_{xx,raw}(0) * R_{yy,raw}(0)}} * R_{xy,raw}(m). \quad (3.2)$$

Chapter 4

Fano lineshapes and mode splittings: Can they be artificially generated or obscured by the numerical aperture?

Fano resonances and Rabi splittings are routinely reported in the scientific literature. Asymmetric resonance lineshapes are usually associated with Fano resonances, and two split peaks in the spectrum are often attributed to a Rabi splitting. True Fano resonances and Rabi splittings are unequivocal signatures of coherent coupling between subsystems. However, can the same spectral lineshapes characterizing Fano resonances and Rabi splittings arise from a purely incoherent sum of intensities? Here we answer this question through experiments with a tunable Fabry-Pérot cavity containing a CsPbBr₃ perovskite crystal. By measuring the transmission and photoluminescence of this system using microscope objectives with different numerical aperture (NA), we find that even a modest $NA = 0.4$ can artificially generate Fano resonances and Rabi splittings. We furthermore show that this modest NA can obscure the anti-crossing of a bona fide strongly coupled light-matter system. Through transfer matrix calculations we confirm that these spectral artefacts are due to the incoherent sum of transmitted intensities at different angles captured by the NA . Our results are relevant to the wide nanophotonic community characterizing dispersive optical systems with high numerical aperture microscope objectives. We conclude with general guidelines to avoid pitfalls in the characterization of such optical systems.

4.1 Introduction

4.1.1 Exciton-polaritons in a cavity with CsPbBr₃

Metal halide perovskites (MHPs) are a promising class of materials for many optoelectronic applications thanks to their unique properties. In particular, MHPs can have strong optical absorption [193], high quantum yield [194] and tunable bandgap [195]. Furthermore, MHPs can be fabricated relatively easily and inexpensively [196]. These and other features have generated much interest in MHPs for photovoltaics [197] and light-emitting devices [198] mainly, but applications to lasers [199] and photo-/X-ray detectors [200, 201] are also being investigated. Very recently, MHPs have also attracted interest for fundamental research in strong light-matter coupling and nonlinear optics. The formation of polaritons (i.e., strongly coupled excitons and photons) [202, 203] and their condensation [26, 78, 125, 204, 205] have been observed in various photonic resonators containing different types of MHPs. Experiments under pulsed excitation have revealed strong mutual interactions between MHP polaritons, resulting in highly nonlinear phenomena even at room temperature [206]. However, nonlinear effects have not been realized under continuous wave driving simply because MHPs degrade under intense laser illumination before displaying optical nonlinearity. In this vein, we decided to investigate the optical response of MHP polaritons in our tunable cavity setup, first at room temperature and eventually at cryogenic temperatures. We chose to work with CsPbBr₃ since it is a stable MHP with bandgap around 532 nm, which is the wavelength of our laser and the reflectivity maximum of our dielectric mirrors.

This chapter reports results of optical experiments with a tunable cavity containing a CsPbBr₃ crystal at room temperature. To evidence strong exciton-photon coupling, we measured transmittance and photoluminescence spectra as a function of the cavity length. We decided to investigate these spectra using microscope objectives with different numerical apertures. Surprisingly, we found certain spectral features resembling Fano resonances and Rabi splittings — signatures of coherent light-matter coupling — for some microscope objectives but not for others. In view of these findings, we conducted a systematic study of how the numerical apertures of the microscope objectives influence these measured spectra of tunable cavity systems. This chapter presents the results of that study.

4.1.2 Fano resonance and Rabi splitting

Fano resonances and Rabi splittings have inspired countless efforts in photonics research [207–210]. These two effects were discovered in quantum frameworks, yet their essence can be easily recognized in classical models of coupled harmonic oscillators [211–213]. When the oscillators are detuned and one is much more damped than the other, interference effects lead to an asymmetric Fano-like resonance in the

spectrum of the heavily damped oscillator [212]. Conversely, when the two oscillators are strongly coupled, weakly damped, and tuned in resonance, the total energy is split between two new eigenmodes at different frequencies [211, 213]. This is the so-called normal mode splitting or Rabi splitting. Within the classical framework, the main difference between the two effects sits in the ratio of the frequency detuning to the total loss rates of the oscillators. This ratio is large for a Fano resonance and close to zero for a Rabi splitting. The common aspect is the need for coherent coupling between two oscillators. Without this key ingredient, the bare oscillators simply display Lorentzian lineshapes around their resonance frequencies.

Interest in Fano resonances and Rabi splittings is so large that a complete list of references in photonics only is beyond our reach. Nonetheless, we can highlight a few scenarios where Fano resonances are relevant: sensing [214, 215], switching [216], directional scattering [208, 217, 218], spontaneous emission [219], lasing [220], and non-reciprocity [221]. Meanwhile, Rabi splittings have attracted interest for enhancing or modifying chemical landscapes [222, 223], optical nonlinearities [29], electrical conductivities [224, 225], biological processes [226], lasing [78, 227], and quantum light emission [36, 37]. Key to progress in all these directions is the correct identification of Fano resonances and Rabi splittings based on optical measurements. A first challenge in this endeavor arises because the transmittance (T), reflectance (R), absorbance (A), and photoluminescence (PL), of a fixed light-matter system generally display different features [228]. In particular, Rabi splittings observed in T , R , A , and PL are in general all different. The differences can be so large that some observables display a well-resolved Rabi splitting while other observables display no splitting at all. This effect has been discussed in the literature [229, 230], and coupled oscillator analogs can shed some light into its origin [231]. Here, we consider a second challenge in the identification of Fano resonances and Rabi splittings — one that appears to have never been considered, yet is highly relevant to experiments. In particular, we ask: Can the numerical aperture(s) of the measuring instrument artificially generate or obscure Fano resonances and Rabi splittings? To address this question, we performed experiments with the simplest and most widely used optical resonator: a Fabry-Pérot cavity. Our cavity contains a perovskite crystal of contemporary interest, namely CsPbBr_3 [125, 232]. Our coupled oscillator system is therefore one that comprises cavity photons and semiconductor excitons. As we will show, the choice of numerical aperture(s) used to probe this system conveys a number of surprises and spectral artefacts which can lead to misleading conclusions when not properly considered.

4.2 Artificially generated Fano lineshape and Rabi splitting by a moderately large NA

Figure 4.1(a) illustrates our experimental system: a tunable Fabry-Pérot cavity with a CsPbBr_3 crystal inside. CsPbBr_3 crystals were synthesized on a mica substrate

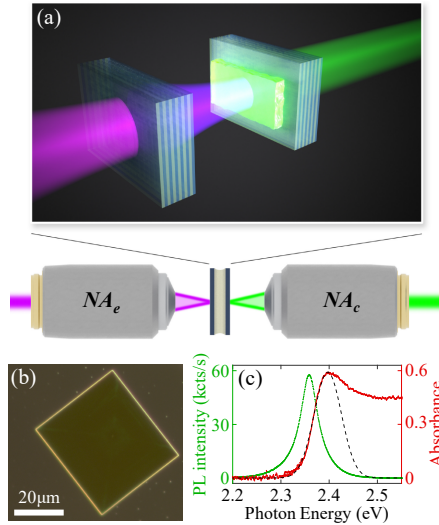


Figure 4.1: (a) Tunable cavity with a CsPbBr₃ crystal inside. The excitation light is coupled into the cavity through a microscope objective with numerical aperture NA_e and light is collected through a different objective with numerical aperture NA_c . (b) Dark-field microscope image of a typical CsPbBr₃ crystal on a glass substrate. (c) Absorbance and photoluminescence spectra of the CsPbBr₃ crystal used for the experiments in Fig. 4.2, Fig. 4.3, and Fig. 4.5. The excitonic peak in the absorbance spectrum is fitted with a Gaussian distribution centered at 2.397 ± 0.002 eV and a standard deviation of 66 meV. The photoluminescence is fitted with a Lorentzian lineshape centered at 2.358 ± 0.002 eV and with a 44 meV linewidth.

via chemical vapor deposition [233]. Using thermal release tape, the crystals were subsequently transferred onto a glass substrate for characterization, or onto a mirror for experiments. Figure 4.1(b) shows a dark-field image of a typical CsPbBr₃ crystal on a glass substrate. Figure 4.1(c) shows the absorbance and *PL* spectrum of the CsPbBr₃ crystal used in all our experiments discussed below. The absorbance spectrum has an excitonic peak at 2.397 ± 0.002 eV with a 66 meV linewidth, estimated via the Gaussian fit shown in Fig. 4.1(c). The *PL* spectrum is fitted with a Lorentzian lineshape centered at 2.358 ± 0.002 eV and with 44 meV linewidth. We placed this crystal in our cavity, which is made by two distributed Bragg reflectors (DBRs) with a peak reflectance of 99.9% at 530 nm. The position and orientation of one of the cavity mirrors are controlled with a six degree-of-freedom piezoelectric actuator. The other mirror, coated with the CsPbBr₃ crystal, is mounted on three piezoelectric actuators. Two of the actuators are used to place the CsPbBr₃ crystal along the optical axis; the

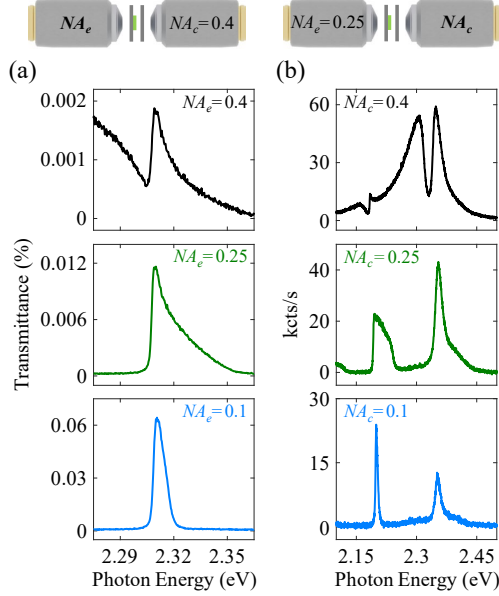


Figure 4.2: (a) Transmittance and (b) photoluminescence spectra of the CsPbBr₃-cavity system. In (a) we vary the excitation numerical aperture NA_e while keeping the collection numerical aperture $NA_c = 0.4$ constant. In (b) we vary NA_c while keeping $NA_e = 0.25$ constant. The cavity length is $L = 3440$ nm in (a), and $L = 3360$ nm in (b).

other actuator serves to finely adjust the cavity length. Using this setup, we measured the T and PL spectrum as a function of the cavity length. We use an incoherent white light source for T measurements, and a 405 nm laser for PL measurements. Optical excitation and collection were achieved through microscope objectives with numerical aperture as specified for each figure below. We refer to the excitation NA as NA_e , and to the collection NA as NA_c . For T measurements, we varied NA_e while keeping $NA_c = 0.4$ constant. For PL measurements, we varied NA_c while keeping $NA_e = 0.25$ constant. In the PL case, the choice $NA_e = 0.25$ is not so relevant because the incident laser is filtered out and we only collect the luminescence. Moreover, the laser power for all PL measurements is sufficiently low (40 μ W at the excitation objective) to avoid nonlinear effects and crystal degradation.

Figure 4.2(a) shows T spectra of the CsPbBr₃-cavity system at a cavity length $L = 3440$ nm, for three different NA_e . For $NA_e = 0.1$, we observe a nearly-symmetric resonance peak on a flat background. The same optical resonance acquires a high-energy tail when NA_e increases to 0.25. Then, an asymmetric lineshape resembling a Fano resonance appears for $NA_e = 0.4$. This lineshape is not the result of Fano

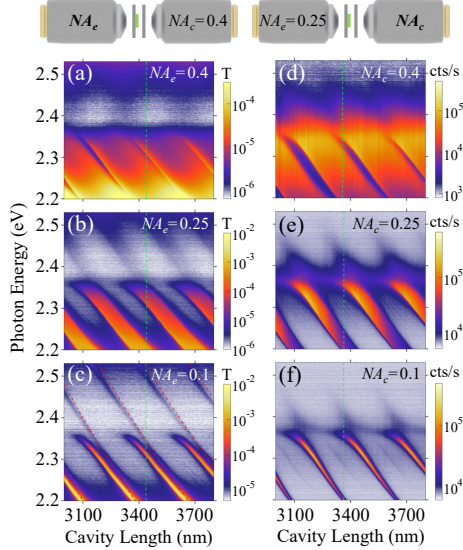


Figure 4.3: (a)-(c) Transmittance and (d)-(f) photoluminescence spectra of the CsPbBr₃-cavity system as a function of the cavity length. In (a)-(c) we vary the excitation numerical aperture NA_e while keeping the collection numerical aperture $NA_c = 0.4$ constant. In (a)-(c) we vary NA_c while keeping $NA_e = 0.25$ constant. The bright bands in all measurements correspond to cavity resonances associated with different longitudinal mode numbers. The resonances are blurred at high energies by the bandgap absorption of CsPbBr₃. For reference, (c) shows empty cavity modes as red dashed lines. Green dashed lines in (a)-(c) and (d)-(f) indicate the cavity lengths inspected in Fig. 4.2(a) and Fig. 4.2(b), respectively.

interference. Instead, it is an artefact of the large NA_e . As demonstrated ahead, the asymmetric lineshape is due to the incoherent sum of intensities transmitted through the cavity at different angles.

Figure 4.2(b) shows *PL* spectra of the same CsPbBr₃-cavity system, for a slightly different cavity length $L = 3360$ nm. For $NA_c = 0.1$, we observe two nearly-symmetric resonance peaks on a flat background. Each of these peaks corresponds to a cavity resonance. For $NA_c = 0.25$, the peaks acquire a high-energy tail. For $NA_c = 0.4$, the measured spectrum displays two remarkable features: a feature resembling a normal mode splitting appears around 2.32 eV, and a Fano-like resonance appears around 2.18 eV. These spectral features, which only appear for a sufficiently large NA_c , are artefacts. They are due to the incoherent sum of the cavity-enhanced perovskite emission at different angles. The apparent normal mode splitting in Fig. 4.2(b), around

2.33 eV, is suspiciously close to the bare exciton energy at 2.397 eV. However, this proximity is only a coincidence. In order to elucidate the origin of all these artefacts, we proceed to inspect spectra across a wide range of cavity lengths.

Figure 4.3 shows T and PL spectra as a function of cavity length for the same configurations considered in Fig. 4.2. For reference, the vertical green dashed lines in Figs. 4.3(a-c) [respectively, Figs. 4.3(d-f)] indicate the cavity length considered in Fig. 4.2(a) [respectively, Fig. 4.2(b)]. Each bright band in the color plot corresponds to a resonance associated with a particular longitudinal mode of the cavity. The longitudinal modes of the empty cavity are shown as red dashed lines in Fig. 4.3(c). Their resonance frequency satisfies $f = qc/(2L)$, with q the longitudinal mode number, c the speed of light, and L the cavity length.

We first analyze the T spectra in Figs. 4.3(a-c). Notice how, as NA_e increases, all resonances broaden in energy. For $NA_e = 0.4$, shown in Fig. 4.3(a), the transmission from consecutive longitudinal modes nearly overlap. Only a narrow transmission dip between resonances remains. This is the Fano-like dip observed in Fig. 4.2(a). The results in Figs. 4.3(a-c) already reveal the origin of the transmission dip: as NA_e increases, transmission bands associated with consecutive q increasingly approach each other in energy and eventually overlap. As Figs. 4.3(d-f) show, similar behavior arises in the PL measurements when NA_c increases. For $NA_c = 0.4$, shown in Fig. 4.3(d), the emission from consecutive longitudinal modes nearly overlap in energy. The emission dip between bands with consecutive q , at fixed cavity length, results in features that can resemble Fano resonances or mode splittings but are neither.

4.3 Empty cavity transmittance measurements and transfer matrix calculations

Our measurements clearly demonstrate that even a moderately large NA can generate spectral features reminiscent of coherently coupled systems. Two important questions remain. First, are these spectral features due to the presence of an excitonic material in our cavity? Second, are interference effects responsible for these spectral features in any way? In the following, we will demonstrate that the answer to both of these questions is negative. We will analyze T spectra for an empty Fabry-Pérot cavity, in experiments and theory. While this analysis is necessarily restricted to T (there is no PL in an empty cavity), the insights obtained from it are general.

Figure 4.4(a) shows experimental T spectra for the same three NA_e considered in Fig. 4.2 and Fig. 4.3, and at a cavity length $L = 3430$ nm. As NA_e increases, we again observe a broadening of the resonance and the emergence of a Fano-like lineshape. This demonstrates how increasing NA_e generates a Fano-like lineshape even in the absence of an excitonic material. To identify the mechanism underlying this effect, we use a transfer matrix model to calculate the transmission of an empty cavity. Our goal is to determine whether the incoherent sum of transmitted intensities over a finite

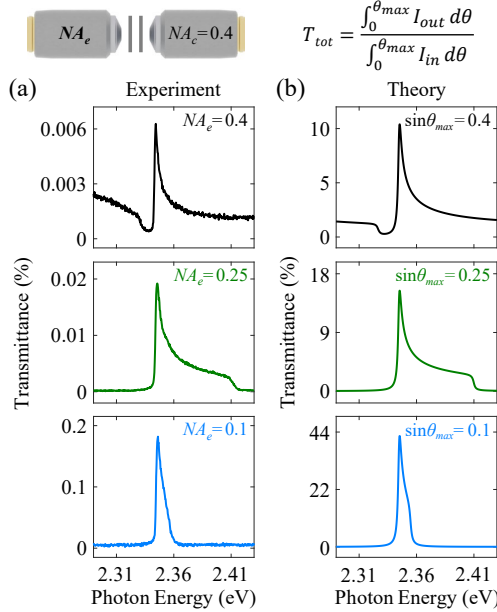


Figure 4.4: (a) Experimental transmittance spectra of an empty cavity for three different NA_e . (b) Transfer matrix calculations of transmittance spectra averaged over an angular range corresponding to the experimental NA_e . The averaged transmittance is given by the incoherent sum of transmitted intensities at different angles, divided by the incident intensity over the same angular range. The cavity length is $L = 3430$ nm in both experiments and calculations.

angular range can lead to Fano-like lineshapes.

Our transfer matrix calculations are done for a DBR-vacuum-DBR cavity. We model each DBR as a stack of 6 pairs of layers with refractive indices $n_1 = 1.45$ and $n_2 = 2.3$. These refractive index values correspond, within the frequency range of interest, to our experimental DBRs made of silica and Ta_2O_5 . While the experimental DBR has 9 pairs of layers, we implemented 6 pairs in the calculations to avoid dealing with unnecessarily small linewidths and long computation times. This change does not affect any of the results presented in this chapter, since the spectral lineshapes we will show have linewidths that are dominated by the angular ranges over which the transmitted intensities are averaged.

We calculate the transmittance (i.e., transmitted power normalized to the incident power) when the cavity is illuminated by a single plane wave, and we vary the angle of incidence in steps of 0.005 degrees. Then, we average the transmittance over the angular range corresponding to the NA_e of interest. We also sum the contributions of the two orthogonal polarizations, in correspondence to our experiments which were

done using unpolarized light.

Figure 4.4(b) shows transfer matrix calculations results obtained as described above, for the same cavity length considered in Fig. 4.4(a). Notice how the experimentally-observed Fano-like lineshapes are reproduced in the calculations. This demonstrates that the sum of transmitted intensities at different incident angles suffices to generate Fano-like lineshapes. Since we are adding intensities and not field amplitudes, we are neglecting interference effects due to different plane waves. Hence, by reproducing the experimentally-observed lineshapes in this way, we can conclude that the measured lineshapes are not due to Fano interference. We therefore call these Fano-like lineshapes “artefacts”. While our calculations qualitatively reproduce the experimental lineshapes very well, the value of T is much lower in experiments. We attribute this difference to an imperfect alignment of the cavity mirrors, which leads to very significant optical losses through the sides of the cavity. Scattering losses may also reduce the value of T in experiments, but we suspect this contribution is smaller given the uncertainty we have in the angular alignment (~ 5 millidegrees).

4.4 Obscured Rabi splitting by a moderately large NA

Having shown that using a moderately large NA can generate spectral lineshapes resembling those characterizing coherently coupled systems, we turn our attention to the complementary question: Can the NA obscure spectral features of bona fide coherently coupled systems? To answer this question, we inspect T and PL spectra of our perovskite-cavity system for shorter cavity lengths than considered in Fig. 4.2 and Fig. 4.3. Figures 4.5(a-c) show measurements in a parameter range where the $q = 7$ cavity mode crosses the exciton energy. The energies of the bare cavity mode and exciton are shown as dashed black lines in all panels in Fig. 4.5.

Let us first consider the results for the smallest NA_e shown in Fig. 4.5(c). Notice how, as the cavity length decreases, the resonance peak bends away from the empty cavity mode and does not cross the exciton energy (2.397 eV). This anti-crossing behavior is characteristic of strong coupling. A simple and intuitive way to estimate the coupling regime (weak vs strong) of our system is by fitting the measured resonances with the eigenvalues of a 2×2 Hamiltonian describing our exciton-photon coupled system. The diagonal terms of the Hamiltonian contain the exciton and cavity photon energies. We know the bare exciton energy from A measurements in Fig. 4.1(c), and the bare cavity photon energy from the relation $f = qc/(2L)$. The off-diagonal term of the Hamiltonian, i.e., the coupling strength, is the only fit parameter in our model. By fitting the low-energy eigenvalue of the Hamiltonian to the resonance observed in the Fig. 4.5(c) measurements we estimate a Rabi splitting of 150 meV. This value is well above the sum of the exciton and cavity photon linewidths, which are 66 meV and 0.5 meV, respectively. Therefore, our exciton-photon system is in the strong coupling regime and the observed resonances correspond to exciton-polaritons. This is not a surprising result. Indeed, strong exciton-photon coupling was recently shown in similar

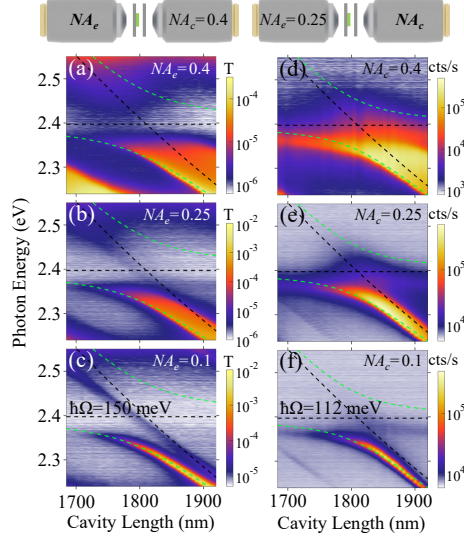


Figure 4.5: (a)-(b) Transmittance and (c)-(d) photoluminescence spectra of the CsPbBr₃-cavity system as a function of the cavity length, for a shorter cavity than in Fig. 4.2 and Fig. 4.3. The horizontal dashed black line indicates the exciton energy, and the tilted dashed black line indicates the energy of the $q = 7$ longitudinal cavity mode. The green dashed lines in all panel are the eigenvalues of a 2×2 Hamiltonian representing the exciton-photon coupled system. The coupling constant is the only fit parameter, and the result is shown in (c) and (f) for transmittance and photoluminescence measurements, respectively. The coupling was not changed for measurements with different NA .

Fabry-Pérot cavities filled with the same perovskite semiconductor. [125, 232]. The interesting new observation, enabled by our tunable cavity system, is that the polariton band is so broadened for $NA_e = 0.4$ that its central energy appears to coincide with the bare cavity mode. Measuring spectra with a single moderately large NA_e only, as done in many works, can lead to the erroneous conclusion that there is no strong coupling. The same holds for the *PL* measurements shown in Figs. 4.5(d-f). These results clearly demonstrate how a moderately large NA can obscure the spectral signature of a bona fide strongly coupled system.

The measurements in Fig. 4.5 display features which require clarification. First, the Rabi splitting observed in *PL* (112 meV) is smaller than the one observed in *T* (150 meV). This is consistent with previous calculations [228] and many experimental observations of polariton systems [229]. Second, the upper polariton is not visible in Fig. 4.5 because of above-bandgap absorption. This can be understood in light of the

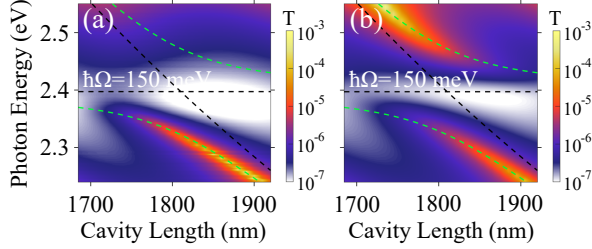


Figure 4.6: Transmittance, calculated using the transfer matrix method, for a tunable cavity containing a layer representing (a) CsPbBr₃, or (b) a material with optical response determined by a single Lorentzian oscillator with the same frequency, line width, and oscillator strength, as the exciton in CsPbBr₃. The frequency-dependent complex refractive indices of both systems are shown in Appendix 4.6.1. Green and black dashed lines are exactly the same as in Fig. 4.5. The Rabi splitting obtained empirically from the upper-lower polariton splitting in (b) is equal to the one deduced from fitting to the lower polariton in Fig. 4.5(c).

absorbance measurements in Fig. 4.1(c). There one can see that absorbance is much greater at energies above the exciton energy, where the upper polariton may be expected but the bandgap absorption sets in. Indeed, previous works reporting exciton-polaritons in optical cavities filled with the same perovskite semiconductor also did not observe the upper polariton [26]. The energy splitting between upper and lower polaritons at zero detuning (i.e., the Rabi splitting) is the usual indicator of strong coupling. Since the upper polariton is absent in our data, the accuracy of the coupling constant we determined by fitting to the lower polariton only could be doubtful. We would now like to dissipate this doubt by calculating transmittance spectra as a function of the cavity length for two systems at normal incidence. The calculations are done using the transfer matrix method, and details are provided in Appendix 4.6.1. System I is a cavity with CsPbBr₃, as in our experiments. The complex refractive index of CsPbBr₃ was obtained by applying the Beer-Lambert law to our experimental absorbance data in Fig. 4.1, and then using the Kramers-Kronig relations. This leads to refractive index values that are consistent with previous ones obtained via ellipsometry measurements of CsPbBr₃ crystals similar to ours. System II is the same cavity, with CsPbBr₃ replaced by a hypothetical material with a single Lorentzian oscillator response. The frequency, linewidth, and amplitude of that oscillator were chosen such that the resultant complex refractive index matches the one of CsPbBr₃ at low energies, where the excitonic response dominates over the bandgap absorption. Comparing these two systems is fair because strong coupling is determined by the excitonic frequency, linewidth, and oscillator strength, and we are keeping these quantities constant. In Appendix 4.6.1 we show the frequency-dependent complex refractive indices of both systems.

Figure 4.6 shows calculation results for systems I and II as described above. Figure 4.6(a) reproduces our experimental observations from Fig. 4.5(c), where the upper polariton is absent. The upper polariton reveals itself when the above-bandgap absorption is removed and the excitonic response is retained, as Fig. 4.6(b) shows. More importantly, notice that the lower polariton dispersion is practically the same in the two systems. For reference, we superimposed (not fitted) the Hamiltonian eigenvalues from Fig. 4.5(c) on Fig. 4.6. Notice the excellent agreement between the eigenvalues and the lower polariton energies in both transfer matrix calculations. Moreover, the coupling constant obtained from the fitting (150 meV) exactly reproduces the Rabi splitting which can be empirically (i.e., without any fitting) determined in Fig. 4.6(b). This demonstrates the accuracy of the coupling constant deduced from the fitting.

4.5 Conclusion

In conclusion, we have shown that a moderately large numerical aperture can artificially generate and obscure spectral features associated with coherently coupled systems. In particular, we have seen Fano-like resonances and apparent normal mode splittings entirely due to the incoherent sum of transmitted intensities at different angles collected by the NA . Moreover, we have seen how the spectral signature of bona fide strongly coupled system, the Rabi splitting, can be obscured in measurements with a large NA . While these results were obtained using a tunable Fabry-Pérot cavity, we believe that the spectral artefacts we report can also be found in other dispersive nanophotonic systems of contemporary interest, such as plasmonic gratings and metasurfaces. In general, Fano-like lineshapes can be artificially generated whenever the resonance frequency of an optical mode is not constant across the angular range of the measurement. Meanwhile, spectral features resembling normal mode splittings can emerge whenever the frequency separation between two (orthogonal) modes is smaller than the apparent linewidths which are artificially broadened by the numerical aperture. These spectral artefacts can be avoided by measuring with the smallest possible NA , such that the resonance frequency is constant over the limited angular range of the NA . Alternatively, angle-resolved measurements can also avoid pitfalls. We recognize that these recommendations may be difficult to implement when measuring the transmission of small samples, as often the case in nanophotonics research. In that case, a full energy-angle-resolved theoretical study reproducing the measured lineshapes with good accuracy seems to be the only way to assess the true nature of Fano-like lineshapes and Rabi-like splittings. In any case, the mere experimental observation of spectral lineshapes resembling Fano resonances or normal mode splittings cannot by itself be taken as solid evidence of coherent optical phenomena.

4.6 Appendices

4.6.1 Details on transfer matrix calculation

Here we provide details on the transfer matrix calculations presented in Fig. 4.6. The calculations involve a Fabry-Pérot cavity made by two distributed Bragg reflectors (DBRs). As in the experiments, each DBR in the calculations consists of 9 pairs of layers with refractive indices $n_1 = 1.45$ and $n_2 = 2.3$, corresponding to silica and tantalum pentoxide in the frequency range of interest. The thicknesses of the layers with $n_1 = 1.45$ and $n_2 = 2.3$ are 91 nm and 58 nm, respectively. The resultant DBR has a photonic stop-band centered at $\lambda = 530$ nm.

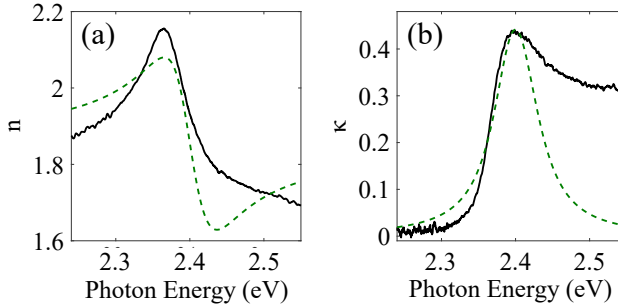


Figure 4.7: (a) Refractive indices n , and (b) extinction coefficients κ , used for the transfer matrix calculations giving the results in Fig. 4.6. Black solid lines correspond to the CsPbBr₃ crystal, i.e., System I. Green dashed lines correspond to the hypothetical material with n and κ fixed by a single Lorentzian oscillator, i.e., System II.

Figure 4.6(a) shows results when the cavity contains a material with refractive index n and extinction coefficient κ corresponding to the one of CsPbBr₃; we call this System I. The value of κ was derived from our absorbance measurement [Fig. 4.1(c)]. Using this value, the index n was calculated via the Kramers-Kronig relations. We added a background index of 0.68, in agreement with previously reported ellipsometric data for the same material (see Ref. [234]). The thickness of the crystal used in the calculation is 150 ± 30 nm, which agrees with our profilometer measurement.

Figure 4.6(b) shows results when the cavity contains a hypothetical material with n and κ fixed by a single Lorentzian oscillator, instead of the CsPbBr₃ layer; we call this System II. The frequency, linewidth, and amplitude of that oscillator were chosen such that the resultant n and κ match the one of CsPbBr₃ at low energies, where the excitonic response dominates over the bandgap absorption. The layer thickness is also 150 nm. Figure 4.7 shows the values of n and κ used to produce the results in Fig. 4.6 for Systems I and II.

Chapter 5

Open access tunable cavity in a closed-cycle cryostat

In this chapter we describe the construction and characterization of a tunable cavity setup in a closed-cycle cryostat, as well as the utilization of this setup for probing the nonlinear optical response of a CsPbBr_3 perovskite semiconductor. The characterization we perform focuses on the mechanical stability of the cavity, and it is done by measuring the transmitted intensity of a laser. Our results reveal that, due to the influence of mechanical fluctuations, the setup can currently be used for meaningful cavity experiments only if the cryo-cooler is OFF, or if the cryo-cooler is ON but the measurement is performed fast enough to avoid the effects of slow mechanical fluctuations. Using the latter approach, we discover a highly nonlinear response in a plano-concave cavity containing a CsPbBr_3 perovskite crystal. This strong nonlinearity is evidenced by the first observation of optical bistability in any perovskite system.

5.1 Introduction

Over the past decades, there have been many efforts in the physics community to realize solid-state optical cavities with strong Kerr-type nonlinearity [127, 235, 236]. Such highly nonlinear cavities are desired for fundamental physics research as well as technological applications. For instance, a single-mode cavity with single-photon nonlinearity could convert classical laser light into anti-bunched light via the photon blockade effect [36, 37]. Moreover, arrays of highly-nonlinear cavities could be used to simulate strongly-correlated states of quantum systems, and to solve hard optimization problems programmed in the interactions between cavities [41, 42, 67, 68].

As discussed in Chapter 1, one approach to realize a strong Kerr-type nonlinearity is by leveraging polariton-polariton interactions in semiconductor cavities. While there has been impressive progress in this direction with III-V and II-VI semiconductor cavities [22, 27, 237–241], a single-photon nonlinearity (single-particle interaction energy commensurate with resonance linewidth) under continuous-wave laser illumination has never been realized. Very recently, there was an impressive demonstration of single-photon nonlinearity with room-temperature organic polaritons under pulsed excitation [128]. However, single-photon nonlinearity in the technologically-relevant continuous-wave driving regime has never been realized.

Important challenges to address in this context are the weak nonlinear response of most commonly used excitonic materials [242, 243], as well as the difficulty in integrating new materials with standard cavity architectures. In view of these challenges, many groups (including us) have been investigating open-access tunable cavity systems. These open-access cavities can easily incorporate new materials which are promising to realize strong nonlinearities. In this vein, we have identified cuprous oxide and CsPbBr_3 perovskite semiconductors as two promising candidates for realizing highly nonlinear regimes. Both materials have been reported to possess Rydberg excitons at cryogenic temperatures [204, 244]. With the perspective of incorporating these materials in our cavity and probing them at low temperatures, we constructed a new tunable-cavity system operating in a closed-cycle cryostat.

Up to date, two types of cryostats have been widely used for tunable cavity setups: Helium bath [18, 81] and closed-cycle cryostat [91, 245]. We chose a closed-cycle cryostat because it does not require constantly buying Helium, which is an advantage in view of the current worldwide Helium shortage. However, conventional closed-cycle cryostats have the disadvantage that the periodic compressing motion of the Helium cycle exerts strong mechanical vibrations which compromise the stability of the cavity. Moreover, closed-cycle cryostats typically have small sample space volumes. This is not a problem for small monolithic photonic samples made via nanolithography with probing optics placed outside of the cryostat. But in our case, an ample sample space is compulsory to host cavity mirrors and the mounting piezoelectric stages. Thanks to a growing need to tackle these issues and recent technical developments, a novel closed-cycle cryostat was brought to market a few years ago by Montana instruments.

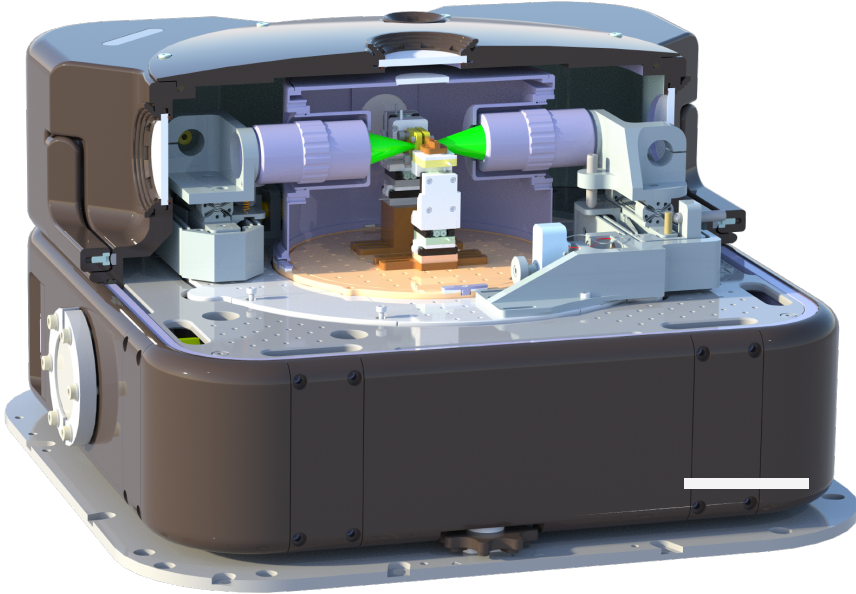


Figure 5.1: 3D illustration of our tunable cavity setup inside a novel closed-cycle cryostat. The vacuum lid and the cold shield are half-cut to give an inside view of the setup. The scale bar is 10 cm.

We developed our cryogenic tunable cavity setup based on that cryostat.

Figure 5.1 shows a 3D illustration of our cryogenic optical setup. The big black box is the cryostat featuring a big inner space equipped with a floating platform for active mechanical damping to suppress environmental noises. On top of the platform we mount two stacks of piezoelectric actuators for displacing and aligning cavity mirrors, microscope objectives for coupling light into and out of the cavity, custom-made actuators for the objectives, and a customized cold shield. All these parts are discussed in more detail in the next section. Although the floating platform provides a stable foundation for our tunable cavity architecture, the final cavity stability is also determined by the stability of the piezo stacks and the mirror mount design. Therefore, we conducted a series of optical measurements to characterize the mechanical stability of our cavity setup. The results of this characterization are the main part of this chapter. Finally, we will also present transmittance measurements obtained in a CsPbBr_3 -cavity system at cryogenic temperature, and report the first observation of optical bistability in any semiconductor perovskite system.

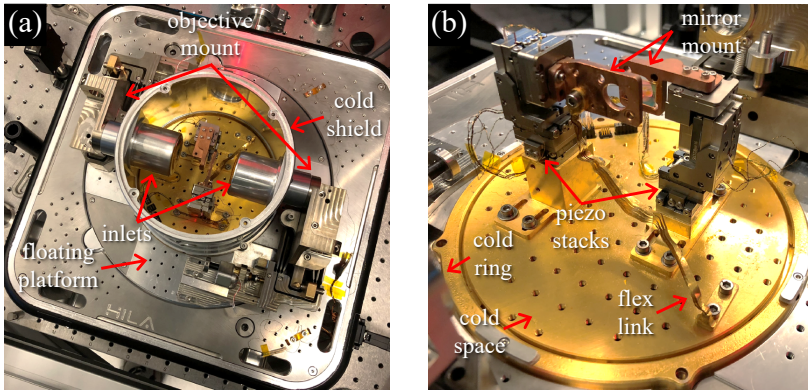


Figure 5.2: (a) Top-view photograph of the setup we built for probing the optical response of a tunable cavity in a closed-cycle cryostat (see text for details). The lid of the cold shield was removed for showing the cold space. (b) Inclined and close-up view photograph of the cold space in the cryostat. The cold shield was removed for illustration purposes.

5.2 Open-access tunable cavity in a closed-cycle cryostat

At the heart of our low-temperature optical experiment is a Gifford-McMahon two-stage closed-cycle cryostat. The cryostat is named HILA, standing for High Inertia Low Acceleration. It is manufactured by Montana Instruments for applications demanding high mechanical stability. Our group acquired the first HILA in Europe, and one of the first HILAs in the world. Figure 5.2(a) shows a photo of the HILA vacuum chamber. The most distinctive feature of the HILA is its large floating platform. This platform is a disk with 25 cm diameter, providing ample space for mounting our experiment. The platform floats on three electromagnetic springs evenly distributed along the perimeter, continuously actuating the platform's levelling position. As a result, mechanical vibrations from the environment can be effectively damped. The platform is also designed to have a large mass. Thanks to the active damping and high inertia of the platform, the mechanical stability is designed to be significantly better than in conventional cryostats.

The HILA platform has three parts: a cold space, a cold ring, and a peripheral ring. The peripheral ring is indicated in Fig. 5.2(a), while the cold space and cold ring are indicated in the closed-up view in Fig. 5.2(b). The cold space is the golden central area, which has a 14 cm diameter. The base of the cold space is thermally connected to a cold finger, and reaches a temperature of 5 K at maximum cooling power. Next

to, and thermally separated from, the cold space is the cold ring. On top of the cold ring there is a metallic cold shield, which serves to isolate the cold space from external thermal radiation. The lid of the cold shield is removed in Fig. 5.2(a) for showing the cold space. The cold ring and the cold shield stay at 30 K when the base of the cold space reaches 5 K. We designed the cold shield, which was manufactured by Montana Instruments, in order to have two cylindrical inlets each accommodating a microscope objective. Glass windows are glued (using thermal grease and GE varnish) at the ends of the inlets to minimize heat transfer to the cold space while retaining optical access. In this way, we can measure the transmission through our cold sample using standard microscope objectives, i.e., usable at ambient temperature and pressure. The remainder of the platform is the peripheral ring. This area is thermally separated from the cryogenic area and no cryo-cooling power is delivered there. The peripheral ring supports our custom-made mechanical actuators for controlling the alignment and position of the two microscope objectives. All mechanical parts for these actuators were designed and manufactured at AMOLF, except the piezoelectric actuators for controlling the focus of the objective which were purchased from Newport. Finally, the peripheral ring also supports extra weights which compensate for the unbalanced mass distribution due to the objectives and their mechanical actuators.

Figure 5.2(b) shows two stacks of four piezoelectric actuators. These are open-loop stick-slip piezoelectric positioners. Each stack has three linear translation stages (xyz) on the bottom, and one rotary stage (either tip or tilt) on top. Custom-made mirror mounts made of copper are directly bolted on the rotary stages. The cavity mirrors are directly glued on the copper mounts with thermal grease and GE varnish. The two piezo stacks stand on two custom-made golden pedestals, which elevate the center of the mirrors to the optical axis passing through the center of the HILA windows. Cooling power is delivered from the base of the cold space to the mirror mounts via flex links, as indicated in Fig. 5.2(b), manufactured by Montana Instruments. The piezo stacks are connected to an external control unit via electrical wires through the sockets integrated in the base. All electrical wires entering the cold space are thermally lagged in the cold ring for minimizing thermal disturbances.

We follow three main steps to prepare our tunable cavity in a closed-cycle cryostat for an optical experiment: coarse cavity alignment, vacuum pumping, and cryo-cooling. A coarse cavity alignment is necessary at room temperature because the travel range of the actuators is limited at low temperature; this is due to the decreased flexibility of the flex link at low temperatures. Additionally, at room temperature the cavity mirrors can be directly seen and this facilitates the alignment process. The cavity mirrors are aligned parallel to each other by tuning the tip and tilt angles while inspecting Fabry-Pérot fringes under narrowband LED illumination; larger fringes correspond to more parallel mirrors. Once the cavity is coarsely aligned, we seal the chamber and pump the vacuum. A cascade of a roughing pump and a turbo pump is used for this purpose, providing a 10^{-4} mbar vacuum at room temperature. Besides, a cryotrap is integrated in the cryostat to further pump the vacuum to 10^{-7} mbar at cryogenic

temperatures. The final step is the cryo-cooling. Due to the large area of the cold space and the thermal load in our experiments, it takes ~ 16 hours for the base plate of the cold space to reach the lowest temperature.

5.3 Characterization of the cavity mechanical stability

5.3.1 Approach

We devised and implemented an optical method to characterize the mechanical stability of our cryogenic cavity system. Figure 5.3(a) shows the setup we built for this purpose. The main idea is to measure changes in the cavity length by monitoring the intensity of a laser I_c transmitted through the cavity. The cavity used in the measurement is made of two planar distributed Bragg reflectors (DBRs), whose layering parameters are the same as those in Chapter 4 [see Appendix 4.6.1]. We also measure a reference intensity I_r . By analyzing the ratio I_c/I_r instead of just I_c , we avoid ascribing intensity fluctuations from the laser to cavity length fluctuations.

Our experimental protocol is as follows. First, for calibration purposes, we measure I_c/I_r as a function of time while scanning the cavity length at a constant speed. Figure 5.3(b) show a typical result. The time axis has been converted to a cavity length variation using the distance between two consecutive optical modes as a ruler. The cavity resonances in Fig. 5.3(b) are broad because we used a HeNe laser emitting at 632 nm. Since this wavelength is outside the stopband of the DBRs comprising our cavity [see Fig. 5.3(c)], the DBRs make a very poor cavity. This allows us to measure cavity length variations across a wide dynamic range of ± 30 nm. Had we used a laser with emission wavelength within the DBR stopband, the dynamic range would be limited to ~ 0.1 nm by the narrow resonance linewidths in that spectral range.

In Fig. 5.3(b) we highlight with a red line the left side of the first resonance, where $I_c/I_r \sim 1$. On this slope, the transmitted intensity is linearly proportional to the cavity length; this is the regime in which we want to operate. Therefore, we park the cavity length at the center of this linear region, and then record long time traces of I_c and I_r using a sampling rate of 2.5 M/s. Finally, using these time traces and the relation between I_c and the change in cavity length ΔL , we assess the fluctuations in the cavity length as shown in the next subsection.

Beyond the laser noise whose effects we suppress via the reference measurement, our method is also affected by detection noise. In order to quantify the detection noise, we performed a control experiment with the laser passing through our entire setup except the cavity. In this way, we found that intrinsic/detection noise in the system results in apparent Gaussian fluctuations in ΔL with standard deviation 0.16 nm. This 0.16 nm can be regarded as the noise added by our entire detection system, and/or as a detection threshold. It is the smallest instantaneous change (given our sampling rate) in cavity length we can reliably detect. The detection threshold can be increased by using a laser wavelength at which the DBRs have larger reflectance, thus resulting in larger

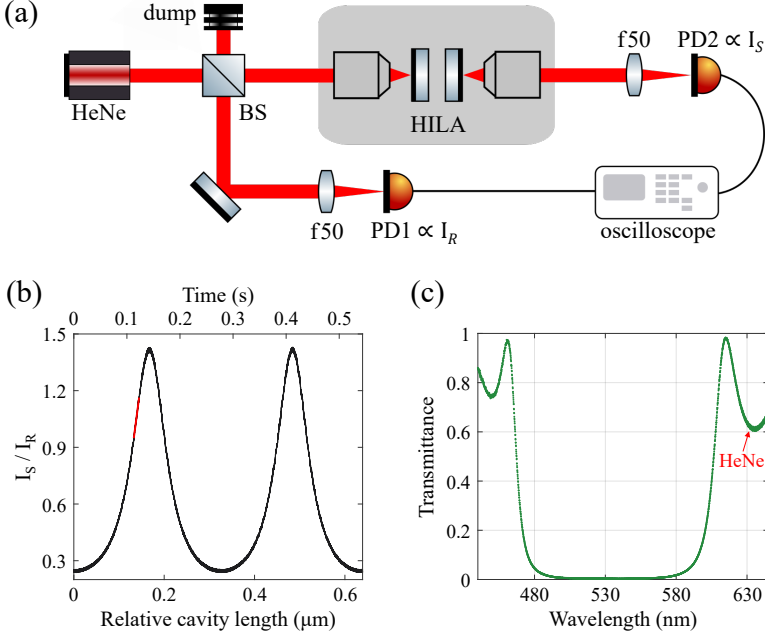


Figure 5.3: (a) Schematic of the optical setup we built for characterizing the stability of our tunable cavity. (b) For a linear ramp of the cavity length, we plot the intensity transmitted through the cavity I_c divided by the reference intensity I_r , as a function of the change in cavity length. The red line highlights a region where I_c/I_r is approximately linear with the cavity length. This is the regime in which the results presented in Fig. 5.4 and Fig. 5.5 were obtained. (c) Transmittance spectrum of the distributed Bragg reflectors making our cavity. The wavelength of the HeNe laser used for the measurements in (b) is indicated by the red dashed line.

sensitivity (intensity change per displacement). However, this is not necessary for our system because typical fluctuations in our cavity turn out to be much greater than the detection threshold.

5.3.2 Results

We characterized the mechanical stability of our empty cavity in two situations: cryo-cooler OFF and cryo-cooler ON. Figure 5.4 summarizes the results when the cryo-cooler is off. Figure 5.4(a) shows the change in cavity length ΔL during a 5 s measurement. Figure 5.4(b) shows a 50 ms section of that time trace, indicated by red dashed lines in Fig. 5.4(a). In this shorter time window, we observe several oscil-

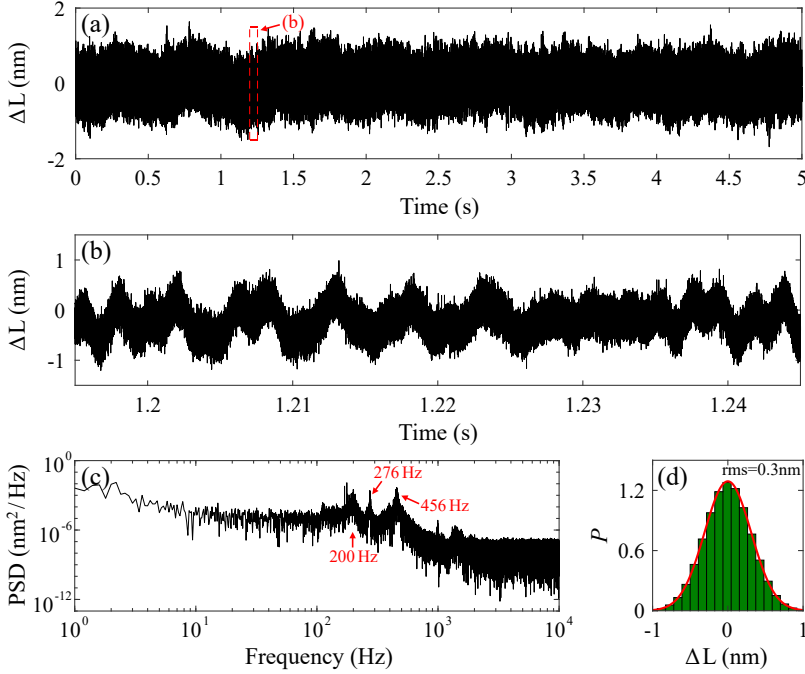


Figure 5.4: Experimental characterization of the tunable cavity stability when the cryo-cooler is off. (a) Cavity length fluctuation (ΔL) as a function of time. (b) Zoom in the red dashed rectangle in (a). (c) Power spectral density of ΔL , and (d) probability density function of ΔL , both calculated using the data in (a). The red curve in (d) is a Gaussian distribution fitted to the data, from which we extract a standard deviation of 0.3 nm.

lations. Figure 5.4(c) shows the power spectral density (PSD) of ΔL , obtained by Fourier transforming the data in Fig. 5.4(a). The PSD reveals three clear peaks at 200 Hz, 276 Hz and 456 Hz, which correspond to the oscillations observed in the time domain. We believe that these oscillations correspond to mechanical vibrations of certain components of the cavity architecture.

The cavity architecture consists of three main mechanical parts: floating platform, piezo stacks, and mirror mounts. First, the floating platform can be ruled out due to its low resonance frequency (~ 0.5 Hz). Second, the mirror mounts alone are unlikely to give rise to oscillations at hundreds of Hz. They are monolithic and firmly bolted on the rotary stages. Besides, the mirror mounts are made of copper and are small. The combination of the high Young's modulus of copper and small dimensions is unlikely to result in structural vibrations at hundreds of Hz. Thus, we think that the piezo stacks are most likely responsible for the observed oscillations and peaks in the PSD. The

piezo stages are based on the stick-slip mechanism and their mechanical structures are not rigid. Moreover, the many-stage stacking can also explain the presence of multiple resonance frequencies. In addition, the design of the mirror mounts employs a cantilever structure to physically separate the two stacks and thereby avoid blocking optical access to the cavity. This design causes a non-normal loading of the mirror mounts on the rotary stages, potentially making the stacks more susceptible to external driving forces and a greater torque.

In Fig. 5.4(d), above 456 Hz, the PSD shows a decay towards a flat plateau starting at 2 kHz. This corresponds to the noise floor of our measurement as extracted from the control experiment. On top of this decaying trend, a small peak at 1 kHz followed by a series of bumps between 1 kHz and 2 kHz are observed. The exact origin of these peaks is unclear.

Finally, to characterize the strength of the cavity length fluctuations, we plot a probability density function (PDF) of ΔL as shown in Fig. 5.4(d). A Gaussian is fitted to the PDF, from which we extract a standard deviation of 0.3 nm for ΔL . Note that the detection noise of the experimental system partly contributes to this number. Assuming that the two Gaussian processes are independent and additive, we conclude a standard deviation of 0.25 nm for the real cavity length fluctuation when the cryo-cooler is off.

Figure 5.5 presents a similar analysis to the one in Fig. 5.4, but for the cryo-cooler ON situation. Figure 5.5(a) shows a 5 s time trace of ΔL , where we observe periodic pulses at 1.4 Hz. These pulses are caused by the mechanical motion of the cryo-cooler. Within each period, one high-amplitude and a few low-amplitude pulses are present. Figure 5.5(b) shows a 50 ms time section within the high-amplitude region indicated in Fig. 5.5(a). Surprisingly, we observe a nearly perfect sinusoidal modulation at 200 Hz and with a 20 nm amplitude. This suggests that the 200 Hz noise component previously observed in Fig. 5.4(d) is the dominant one for the entire cavity system. Figure 5.5(c) illustrates a 50 ms time section of the low-amplitude region indicated in Fig. 5.5(a). The low-amplitude regions are the time sections between the pulses of the cryo-cooler motion. In that time range we can observe a complex waveform comprising several frequency components, and an amplitude bounded within ± 5 nm.

Figure 5.5(d) shows the PSD based on the data in Fig. 5.5(a). As in the cryo-cooler OFF situation, the PSD reaches the noise floor above 2 kHz. Consistent with our observation in Fig. 5.5(a), we observe a strong peak at 200 Hz in the PSD. The peaks at 400 Hz and 276 Hz previously observed also show up. Another peak at 1.4 Hz can also be observed, corresponding to the low-frequency pulsed periodic modulation. We highlight the peaks at 200 Hz and 1.4 Hz in Fig. 5.5(d) as they are the strongest when the cryo-cooler is on. Finally, we build a PDF for the cavity length fluctuation as shown in Fig. 5.5(e). The PDF has a standard deviation of 6.4 nm. The contribution from the detection noise is much smaller than 6.4 nm and can be effectively neglected. In contrast to Fig. 5.4(d), the data with the cryo-cooler ON is not well fitted by a Gaussian distribution [red curve in Fig. 5.5(e)]. This is not surprising because the cavity is not influenced by white noise in the presence of the strong pulsed motion of the cryo-cooler.

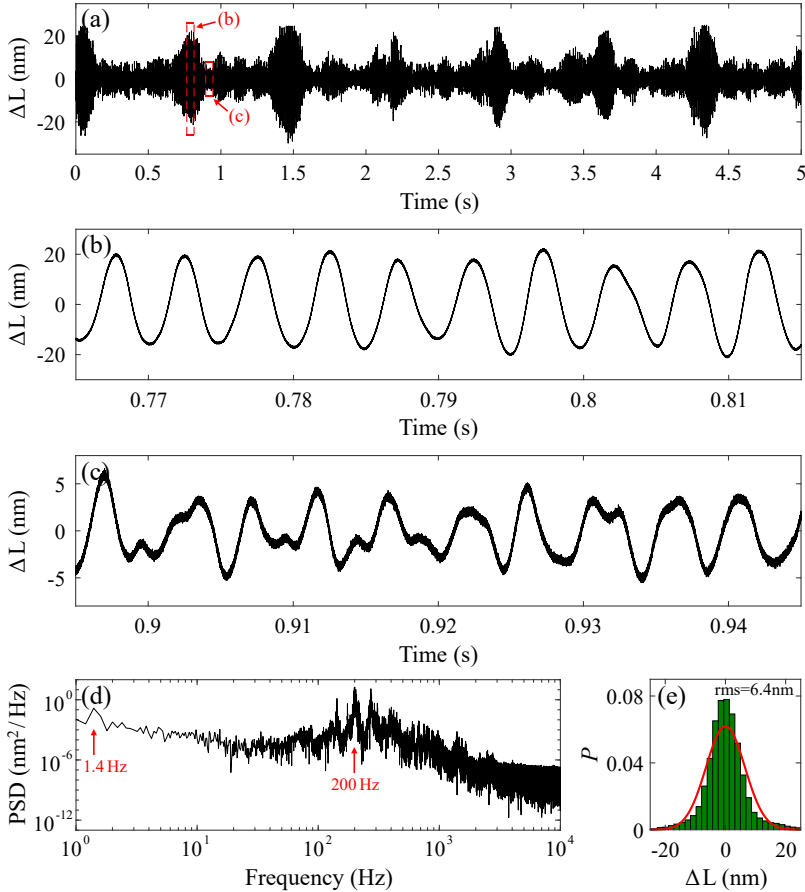


Figure 5.5: Experimental characterization of the tunable cavity stability when the cryo-cooler is on. Everything is the same as in Fig. 5.4, except that we present two zoom-in views in (b,c) of the data in (a) instead of just one. We include the Gaussian fit in (e) for reference, even though the experimental distribution clearly deviates from a Gaussian due to the presence of colored noise.

Based on the above analysis, we conclude that the cryo-cooler has a dramatic influence on the cavity setup, reducing the cavity stability by a factor of 40.

The results above suggest that a better design is needed to improve the mechanical stability of our cavity. This is particularly important for measurements lasting more than a second since the pulse of the cryo-cooler leads to major fluctuations in cavity length. An improved design, while very much necessary, is unfortunately beyond the scope of this thesis due to time constraints. Our group will pursue such a design in the future. In the following, we focus on assessing the performance of our system in the type of optical experiments for which we build it. In particular, we perform transmittance measurements under white light and laser excitation.

5.3.3 Transmittance measurement of a CsPbBr₃-cavity system at cryogenic temperature

In this section we present white light transmittance measurements through our tunable cavity containing a CsPbBr₃ crystal. This is the same system studied in Chapter 4. We perform experiments with the cryo-cooler ON and OFF. In the latter case, we measure the transmittance immediately after switching off the cryo-cooler in order to have approximately the same temperature as with the cryo-cooler ON situation. The purpose of these measurements was two-fold. First, we wanted to test a newly developed measurement automation system involving one of our piezoelectric linear translation stages, a home-built software, and a spectrometer. Second, we wanted to see the effect of cavity length fluctuations on the transmittance.

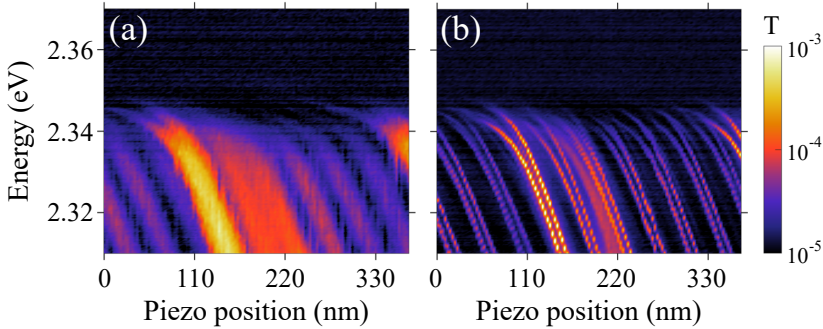


Figure 5.6: Transmittance spectra of our plano-concave tunable cavity in a closed-cycle cryostat containing a CsPbBr₃ crystal, as described in the text. Spectra are plotted as a function of the cavity length, with the zero value being arbitrary. The cryo-cooler is on for the measurements in (a), and off in (b).

The cavity used in this experiment consists of a planar DBR coated with CsPbBr₃ crystals and a concave DBR with 12 μm radius of curvature. Both DBRs have the

same transmittance profile as shown in Fig. 5.3(c). Figure 5.6(a) and Fig. 5.6(b) show measured transmittance spectra for the cryo-cooler ON and OFF, respectively, as a function of the cavity length. An integration time of 100 ms is used for each spectrum. The cavity length is scanned by applying a voltage to one of our linear translation piezoelectric actuators. The applied voltage is converted to a piezo position by scanning over two longitudinal cavity modes and using their separation as a reference distance.

Figures 5.6(a,b) cover the same cavity length range, containing a full series of transverse modes of the same longitudinal number and the start of the next longitudinal mode series. Clearly, the optical resonances in Fig. 5.6(a) are blurred by the vibrations introduced by the cryo-cooler. The counterpart measurement in Fig. 5.6(b) demonstrates a good cavity stability when the cryo-cooler is off. We also observe fine splittings of all optical resonances, due to the ellipticity of the concave mirror. Despite the different linewidths of the resonances in Figs. 5.6(a,b), all resonances bend towards a constant energy without crossing it when reducing the piezo position. This avoided-crossing is characteristic of strong light-matter coupling. Moreover, the apparent discontinuity of each resonance (dotted-like curves) in Fig. 5.6(b) is due to a relatively large step in scanning the cavity length. In this measurement, we used a step of 150 mV to scan the piezo voltage; this corresponds to a 3 nm step for the cavity length, approximately. The minimum step specified by the hardware is 1.5 mV, so there is plenty of room to improve the data quality. However, we also note that linear drifts (~ 5 nm/s) or sudden stepwise changes (~ 5 nm) of the cavity length occasionally occur during the automated spectrum acquisitions in the cryo-cooler OFF situation. This is because when the cryo-cooler is switched off the base temperature of the cold space will rapidly rise, resulting in a thermal strain change in the piezo stacks. In this regard, a trade-off between using a smaller scan step and reducing total measurement time should be carefully considered.

5.4 Optical bistability in a cavity with CsPbBr₃ at cryogenic temperature

Finally, we present preliminary results on nonlinear dynamics of light in a CsPbBr₃-cavity system at 5 K. We use a plano-concave cavity consisting of a planar DBR with CsPbBr₃ crystals on it and a concave DBR with 25 μm radius of curvature. We measured the transmitted intensity of a 532 nm laser through the cavity while modulating the cavity length, similar to our experiments with olive oil in Chapter 2. The cavity length was modulated via controlling the piezo voltage. As the piezo controller does not have a direct analog port to feed a modulation signal, the piezo voltage was modulated with a home-built software that allows us to specify the frequency and the amplitude. In our measurement, we used a 130 Hz triangular waveform scanning across several cavity modes. Since the frequency difference between consecutive transverse modes is much larger than the resonance linewidths due to the lateral confinement of

the concave DBR, we can effectively probe single modes in narrow ranges within the scan. This is true even in the nonlinear regime, as long as the laser power is not so large that it induces a resonance frequency shift that is commensurate with the frequency difference between consecutive resonances.

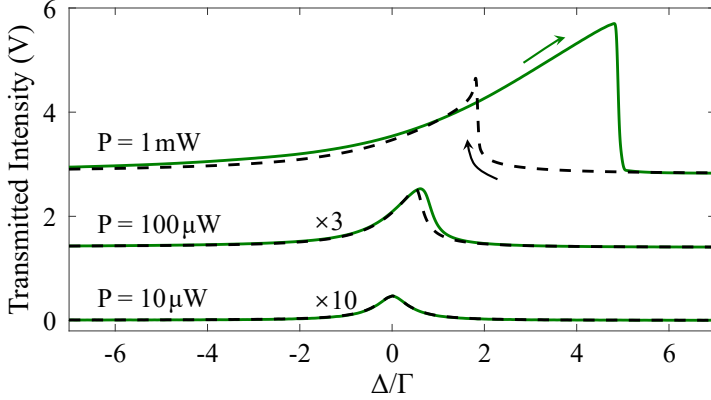


Figure 5.7: Transmitted intensity of a 532 nm laser through the same CsPbBr₃-cavity system considered in Fig. 5.6 while scanning the cavity length. Data is presented for three powers P of the incident laser. The cavity length has been converted to Δ/Γ , i.e., laser-cavity detuning divided by the loss rate of the optical mode, using the linewidth at the lowest power. Green solid and black dashed curves correspond to forward and backward scans of the cavity length, respectively, as indicated by the arrows. For clarity, data for $P = 100 \mu\text{W}$ and $P = 10 \mu\text{W}$ are multiplied by a factor of 3 and 10, respectively; data for $P = 100 \mu\text{W}$ and $P = 1 \text{ mW}$ are displaced vertically. The measurements evidence the emergence of optical hysteresis and bistability as the laser power increases.

Figure 5.7 shows the transmitted intensity through the CsPbBr₃-cavity system as a function of detuning Δ in units of the linewidth Γ . Data is presented for three input powers. All curves are averaged over 80 cycles, and data for the two largest powers are vertically displaced for clarity. For ease of comparison, data for $P = 100 \mu\text{W}$ and $P = 10 \mu\text{W}$ are multiplied by a factor of 3 and 10, respectively. Green solid and black dashed curves correspond to forward and backward scans, respectively. For a low power of $P = 10 \mu\text{W}$, the transmission shows a linear Lorentzian profile. The Lorentzian linewidth of this measurement is used to calibrate the horizontal axis of Fig. 5.7 in units of Γ . For a medium power of $P = 100 \mu\text{W}$, we observe a tilted resonance lineshape towards positive detuning and a small hysteresis area around $\Delta/\Gamma = 0.8$. While the system is not in the bistable regime yet for this power (albeit it is very close), the observed optical hysteresis evidences the presence of optical nonlinearity. For a higher

power of $P = 1$ mW, optical bistability manifests as a strong tilting of the resonance lineshape and a large hysteresis area. As mentioned in the introduction of this chapter, many nonlinear phenomena on perovskite cavities have been observed under pulsed excitation. To the best of our knowledge, this is the first observation of optical bistability under continuous-wave driving in any cavity system with perovskite.

The exact origin of the nonlinearity in our system is still under investigation. Previous studies on CsPbBr₃ at room temperature [127] suggest that the nonlinearity is due to exciton-exciton interactions. This is promising for probing ultrafast nonlinear phenomena, since exciton-exciton interactions are effectively instantaneous. However, our data is not yet sufficient to ascribe the nonlinearity to exciton-exciton interactions. In Fig. 5.7 we observe a small overshoot observed for the $P = 1$ mW data at $\Delta/\Gamma = 1.8$. This overshoot is much smaller than the one observed in Chapter 2 and Chapter 3 where the origin of the nonlinearity was thermal. Nonetheless, it may be indicative of a slow relaxation process for the nonlinearity. Further research is needed to reveal the origin of the dominant nonlinearity in our experiments with CsPbBr₃.

5.5 Conclusion

In summary, we characterized the mechanical stability of our newly built tunable cavity setup in a closed-cycle cryostat. We measured the transmitted intensity of a laser, and from variations in that intensity we deduced the fluctuations in the cavity length. The cavity stability was characterized in two situations: cryo-cooler OFF and ON. In the former situation, our cavity architecture displayed sub-nanometer stability based on our 5 s measurement time window. In the latter situation, we find that the cavity stability is significantly reduced by vibrations from the cryo-cooler. We then investigated the cavity stability in two practical experimental settings. First we measured white light transmittance spectra of a CsPbBr₃-cavity system as a function of the cavity length for the cryo-cooler OFF and ON situations. The measured spectra displayed strongly blurred resonances due to the cryo-cooler motion. Second we measured the transmission of a laser while modulating the length of a CsPbBr₃-containing cavity at relatively high speed (~ 140 Hz). There we observed very clear resonance lineshapes, as expected for a single-mode nonlinear cavity minimally influenced by fluctuations. Overall, our measurements reveal that the current cavity architecture works well with the cryo-cooler OFF, or in fast measurements with cryo-cooler ON. However, further improvements are needed for prolonged and/or slow measurements with cryo-cooler ON. Finally we note that, beyond the construction of the new setup, our result on optical bistability in a CsPbBr₃-cavity system offers exciting perspectives for future physics research. To the best of our knowledge, this is the first observation of optical bistability in any perovskite system. Previous studies on CsPbBr₃ under pulsed excitation indicated the presence of optical nonlinearity due to excitonic interactions. However, in our experiments we also observed a small overshoot which could be indicative of a slow relaxation process. Further research is

thus needed to determine the true origin of the dominant nonlinearity in CsPbBr₃ under continuous-wave illumination.

References

- [1] D. E. Chang, V. Vuletić, and M. D. Lukin, “Quantum nonlinear optics—photon by photon,” *Nat. Photonics* **8**, 685 (2014).
- [2] R. W. Boyd, *Nonlinear Optics*, Fourth Edition (Academic Press, 2020).
- [3] D. Cotter, R. J. Manning, K. J. Blow, A. D. Ellis, A. E. Kelly, D. Nesses, I. D. Phillips, A. J. Poustie, and D. C. Rogers, “Nonlinear Optics for High-Speed Digital Information Processing,” *Science* **286**, 1523 (1999).
- [4] M. Z. Alam, S. A. Schulz, J. Upham, I. De Leon, and R. W. Boyd, “Large optical nonlinearity of nanoantennas coupled to an epsilon-near-zero material,” *Nat. Photonics* **12**, 79 (2018).
- [5] X. Luo, Z. Li, Y. Guo, J. Yao, and W. Yicheng, “Recent progress on new infrared nonlinear optical materials with application prospect,” *J. Solid State Chem.* **270**, 674 (2019).
- [6] D. Ballarini, A. Gianfrate, R. Panico, A. Opala, S. Ghosh, L. Dominici, V. Ardizzone, M. De Giorgi, G. Lerario, G. Gigli, T. C. H. Liew, M. Matuszewski, and D. Sanvitto, “Polaritonic Neuromorphic Computing Outperforms Linear Classifiers,” *Nano Lett.* **20**, 3506 (2020).
- [7] C. Huang, V. J. Sorger, M. Miscuglio, M. Al-Qadasi, A. Mukherjee, L. Lampe, M. Nichols, A. N. Tait, T. Ferreira de Lima, B. A. Marquez, J. Wang, L. Chrostowski, M. P. Fok, D. Brunner, S. Fan, S. Shekhar, P. R. Prucnal, and B. J. Shastri, “Prospects and applications of photonic neural networks,” *Adv. Phys.: X* **7**, 1981155 (2022).
- [8] M. Kauranen and A. V. Zayats, “Nonlinear plasmonics,” *Nat. Photonics* **6**, 737 (2012).
- [9] A. F. Koenderink, A. Alù, and A. Polman, “Nanophotonics: Shrinking light-based technology,” *Science* **348**, 516 (2015).
- [10] M. Z. Alam, I. De Leon, and R. W. Boyd, “Large optical nonlinearity of indium tin oxide in its epsilon-near-zero region,” *Science* **352**, 795 (2016).
- [11] L. Caspani, R. P. M. Kaipurath, M. Clerici, M. Ferrera, T. Roger, J. Kim, N. Kinsey, M. Pietrzyk, A. Di Falco, V. M. Shalaev, A. Boltasseva, and D. Faccio, “Enhanced Nonlinear Refractive Index in ϵ -Near-Zero Materials,” *Phys. Rev. Lett.* **116**, 233901 (2016).
- [12] J. P. Lourdesamy, A. F. J. Runge, T. J. Alexander, D. D. Hudson, A. Blanco-Redondo, and C. M. de Sterke, “Spectrally periodic pulses for enhancement of optical nonlinear effects,” *Nat. Phys.*, 59 (2021).

- [13] K. J. Vahala, "Optical microcavities," *Nature* **424**, 839 (2003).
- [14] R. Albrecht, A. Bommer, C. Deutsch, J. Reichel, and C. Becher, "Coupling of a Single Nitrogen-Vacancy Center in Diamond to a Fiber-Based Microcavity," *Phys. Rev. Lett.* **110**, 243602 (2013).
- [15] P. Lodahl, S. Mahmoodian, and S. Stobbe, "Interfacing single photons and single quantum dots with photonic nanostructures," *Rev. Mod. Phys.* **87**, 347 (2015).
- [16] H. M. Doeleman, E. Verhagen, and A. F. Koenderink, "Antenna–Cavity Hybrids: Matching Polar Opposites for Purcell Enhancements at Any Linewidth," *ACS Photonics* **3**, 1943 (2016).
- [17] A. V. Kavokin, J. J. Baumberg, G. Malpuech, and F. P. Laussy, *Microcavities*, Second Edition (Oxford University Press, 2017).
- [18] D. Wang, H. Kelkar, D. Martin-Cano, D. Rattenbacher, A. Shkarin, T. Utikal, S. Götzinger, and V. Sandoghdar, "Turning a molecule into a coherent two-level quantum system," *Nat. Phys.* **15**, 483 (2019).
- [19] H. M. Gibbs, S. L. McCall, and T. N. C. Venkatesan, "Differential Gain and Bistability Using a Sodium-Filled Fabry-Pérot Interferometer," *Phys. Rev. Lett.* **36**, 1135 (1976).
- [20] H. M. Gibbs, S. L. McCall, T. N. C. Venkatesan, A. C. Gossard, A. Passner, and W. Wiegmann, "Optical bistability in semiconductors," *Appl. Phys. Lett.* **35**, 451 (1979).
- [21] I. Carusotto and C. Ciuti, "Probing Microcavity Polariton Superfluidity through Resonant Rayleigh Scattering," *Phys. Rev. Lett.* **93**, 166401 (2004).
- [22] A. Amo, J. Lefrère, S. Pigeon, C. Adrados, C. Ciuti, I. Carusotto, R. Houdré, E. Giacobino, and A. Bramati, "Superfluidity of polaritons in semiconductor microcavities," *Nat. Phys.* **5**, 805 (2009).
- [23] M. Sich, D. N. Krizhanovskii, M. S. Skolnick, A. V. Gorbach, R. Hartley, D. V. Skryabin, E. A. Cerda-Méndez, K. Biermann, R. Hey, and P. V. Santos, "Observation of bright polariton solitons in a semiconductor microcavity," *Nat. Photonics* **6**, 50 (2012).
- [24] K. S. Daskalakis, S. A. Maier, R. Murray, and S. Kéna-Cohen, "Nonlinear interactions in an organic polariton condensate," *Nat. Mater.* **13**, 271 (2014).
- [25] G. Lerario, A. Fieramosca, F. Barachati, D. Ballarini, K. S. Daskalakis, L. Dominici, M. De Giorgi, S. A. Maier, G. Gigli, S. Kéna-Cohen, and D. Sanvitto, "Room-temperature superfluidity in a polariton condensate," *Nat. Phys.* **13**, 837 (2017).
- [26] R. Su, J. Wang, J. Zhao, J. Xing, W. Zhao, C. Diederichs, T. C. H. Liew, and Q. Xiong, "Room temperature long-range coherent exciton polariton condensate flow in lead halide perovskites," *Sci. Adv.* **4**, eaau0244 (2018).

-
- [27] D. Bajoni, P. Senellart, E. Wertz, I. Sagnes, A. Miard, A. Lemaître, and J. Bloch, “Polariton Laser Using Single Micropillar GaAs–GaAlAs Semiconductor Cavities,” *Phys. Rev. Lett.* **100**, 047401 (2008).
- [28] W. Casteels, F. Storme, A. Le Boité, and C. Ciuti, “Power laws in the dynamic hysteresis of quantum nonlinear photonic resonators,” *Phys. Rev. A* **93**, 033824 (2016).
- [29] S. R. K. Rodriguez, W. Casteels, F. Storme, N. Carlon Zambon, I. Sagnes, L. Le Gratiet, E. Galopin, A. Lemaître, A. Amo, C. Ciuti, and J. Bloch, “Probing a Dissipative Phase Transition via Dynamical Optical Hysteresis,” *Phys. Rev. Lett.* **118**, 247402 (2017).
- [30] W. Casteels, R. Fazio, and C. Ciuti, “Critical dynamical properties of a first-order dissipative phase transition,” *Phys. Rev. A* **95**, 012128 (2017).
- [31] T. L. Heugel, M. Biondi, O. Zilberberg, and R. Chitra, “Quantum Transducer Using a Parametric Driven-Dissipative Phase Transition,” *Phys. Rev. Lett.* **123**, 173601 (2019).
- [32] S. R. K. Rodriguez, “Enhancing the Speed and Sensitivity of a Nonlinear Optical Sensor with Noise,” *Phys. Rev. Applied* **13**, 024032 (2020).
- [33] K. J. H. Peters and S. R. K. Rodriguez, “Limit Cycles and Chaos Induced by a Nonlinearity with Memory,” *Eur. Phys. J. Spec. Top.* (2022).
- [34] X. H. H. Zhang and H. U. Baranger, “Driven-dissipative phase transition in a Kerr oscillator: From semiclassical $\mathcal{P}\mathcal{T}$ symmetry to quantum fluctuations,” *Phys. Rev. A* **103**, 033711 (2021).
- [35] T. Fink, A. Schade, S. Höfling, C. Schneider, and A. İmamoğlu, “Signatures of a dissipative phase transition in photon correlation measurements,” *Nat. Phys.* **14**, 365 (2018).
- [36] G. Muñoz-Matutano, A. Wood, M. Johnsson, X. Vidal, B. Q. Baragiola, A. Reinhard, A. Lemaître, J. Bloch, A. Amo, G. Nogues, B. Besga, M. Richard, and T. Volz, “Emergence of quantum correlations from interacting fibre-cavity polaritons,” *Nat. Mater.* **18**, 213 (2019).
- [37] A. Delteil, T. Fink, A. Schade, S. Höfling, C. Schneider, and A. Ataç İmamoğlu, “Towards polariton blockade of confined exciton–polaritons,” *Nat. Mater.* **18**, 219 (2019).
- [38] T. Jacqmin, I. Carusotto, I. Sagnes, M. Abbarchi, D. D. Solnyshkov, G. Malpuech, E. Galopin, A. Lemaître, J. Bloch, and A. Amo, “Direct Observation of Dirac Cones and a Flatband in a Honeycomb Lattice for Polaritons,” *Phys. Rev. Lett.* **112**, 116402 (2014).

- [39] F. Baboux, L. Ge, T. Jacqmin, M. Biondi, E. Galopin, A. Lemaître, L. Le Gratiet, I. Sagnes, S. Schmidt, H. E. Türeci, A. Amo, and J. Bloch, “Bosonic Condensation and Disorder-Induced Localization in a Flat Band,” *Phys. Rev. Lett.* **116**, 066402 (2016).
- [40] R. M. Wilson, K. W. Mahmud, A. Hu, A. V. Gorshkov, M. Hafezi, and M. Foss-Feig, “Collective phases of strongly interacting cavity photons,” *Phys. Rev. A* **94**, 033801 (2016).
- [41] M. Foss-Feig, P. Niroula, J. T. Young, M. Hafezi, A. V. Gorshkov, R. M. Wilson, and M. F. Maghrebi, “Emergent equilibrium in many-body optical bistability,” *Phys. Rev. A* **95**, 043826 (2017).
- [42] O. Kyriienko, H. Sigurdsson, and T. C. H. Liew, “Probabilistic solving of *NP*-hard problems with bistable nonlinear optical networks,” *Phys. Rev. B* **99**, 195301 (2019).
- [43] F. Leo, S. Coen, P. Kockaert, S.-P. Gorza, P. Emplit, and M. Haelterman, “Temporal cavity solitons in one-dimensional Kerr media as bits in an all-optical buffer,” *Nat. Photonics* **4**, 471 (2010).
- [44] M. Anderson, Y. Wang, F. Leo, S. Coen, M. Erkintalo, and S. G. Murdoch, “Coexistence of Multiple Nonlinear States in a Tristable Passive Kerr Resonator,” *Phys. Rev. X* **7**, 031031 (2017).
- [45] H. M. Gibbs, *Optical Bistability: Controlling Light with Light* (Academic Press, 1985).
- [46] M. Notomi, S. Akihiko, S. Mitsugi, G. Kira, E. Kuramochi, and T. Tanabe, “Optical bistable switching action of Si high-Q photonic-crystal nanocavities,” *Opt. Express* **13**, 2678 (2005).
- [47] M. Notomi, T. Tanabe, A. Shinya, E. Kuramochi, and H. Taniyama, “On-Chip All-Optical Switching and Memory by Silicon Photonic Crystal Nanocavities,” *Adv. Opt. Technol.* (2008).
- [48] L.-D. Haret, T. Tanabe, E. Kuramochi, and M. Notomi, “Extremely low power optical bistability in silicon demonstrated using 1D photonic crystal nanocavity,” *Opt. Express* **17**, 21108 (2009).
- [49] K. Nozaki, T. Tanabe, A. Shinya, S. Matsuo, T. Sato, H. Taniyama, and M. Notomi, “Sub-femtojoule all-optical switching using a photonic-crystal nanocavity,” *Nat. Photonics* **4**, 477 (2010).
- [50] G. Moille, S. Combrié, L. Morgenroth, G. Lehoucq, F. Neuilly, B. Hu, D. Decoster, and A. de Rossi, “Integrated all-optical switch with 10 ps time resolution enabled by ALD,” *Laser Photonics Rev.* **10**, 409 (2016).
- [51] Y. Yu, W. Xue, H. Hu, L. K. Oxenløwe, K. Yvind, and J. Mørk, “All-optical switching improvement using photonic-crystal Fano structures,” *IEEE Photon. J.* **8**, 1 (2016).

-
- [52] T. Tanabe, M. Notomi, S. Mitsugi, A. Shinya, and E. Kuramochi, “Fast bistable all-optical switch and memory on a silicon photonic crystal on-chip,” *Opt. Lett.* **30**, 2575 (2005).
- [53] L. Liu, R. Kumar, K. Huybrechts, T. Spuesens, G. Roelkens, E.-J. Geluk, T. De Vries, P. Regreny, D. Van Thourhout, R. Baets, and G. Morthier, “An ultra-small, low-power, all-optical flip-flop memory on a silicon chip,” *Nat. Photonics* **4**, 182 (2010).
- [54] R. Cerna, Y. Léger, T. K. Paraíso, M. Wouters, F. Morier-Genoud, M. T. Portella-Oberli, and B. Deveaud, “Ultrafast tristable spin memory of a coherent polariton gas,” *Nat. Commun.* **4**, 1 (2013).
- [55] T. C. H. Liew, A. V. Kavokin, T. Ostatnický, M. Kaliteevski, I. A. Shelykh, and R. A. Abram, “Exciton-polariton integrated circuits,” *Phys. Rev. B* **82**, 033302 (2010).
- [56] D. Ballarini, M. De Giorgi, E. Cancellieri, R. Houdré, E. Giacobino, R. Cingolani, A. Bramati, G. Gigli, and D. Sanvitto, “All-optical polariton transistor,” *Nat. Commun.* **4**, 1 (2013).
- [57] C. Antón, T. C. H. Liew, D. Sarkar, M. D. Martín, Z. Hatzopoulos, P. S. Eldridge, P. G. Savvidis, and L. Viña, “Operation speed of polariton condensate switches gated by excitons,” *Phys. Rev. B* **89**, 235312 (2014).
- [58] F. Marsault, H. S. Nguyen, D. Tanese, A. Lemaître, E. Galopin, I. Sagnes, A. Amo, and J. Bloch, “Realization of an all optical exciton-polariton router,” *Appl. Phys. Lett.* **107**, 201115 (2015).
- [59] H. Suchomel, S. Brodbeck, T. C. H. Liew, M. Amthor, M. Klaas, S. Klemmt, M. Kamp, S. Höfling, and C. Schneider, “Prototype of a bistable polariton field-effect transistor switch,” *Sci. Rep.* **7**, 1 (2017).
- [60] D. R. Solli and B. Jalali, “Analog optical computing,” *Nat. Photonics* **9**, 704 (2015).
- [61] I. Carusotto and C. Ciuti, “Quantum fluids of light,” *Rev. Mod. Phys.* **85**, 299 (2013).
- [62] T. Boulier, M. Bamba, A. Amo, C. Adrados, A. Lemaitre, E. Galopin, I. Sagnes, J. Bloch, C. Ciuti, E. Giacobino, and A. Bramati, “Polariton-generated intensity squeezing in semiconductor micropillars,” *Nat. Commun.* **5**, 3260 (2014).
- [63] T. Peyronel, O. Firstenberg, Q.-Y. Liang, S. Hofferberth, A. V. Gorshkov, T. Pohl, M. D. Lukin, and V. Vuletić, “Quantum nonlinear optics with single photons enabled by strongly interacting atoms,” *Nature* **488**, 57 (2012).
- [64] C. Noh and D. G. Angelakis, “Quantum simulations and many-body physics with light,” *Rep. Prog. Phys.* **80**, 016401 (2016).
- [65] M. J. Hartmann, “Quantum simulation with interacting photons,” *J. Opt.* **18**, 104005 (2016).

- [66] M. J. Hartmann, F. G. S. L. Brandao, and M. B. Plenio, “Strongly interacting polaritons in coupled arrays of cavities,” *Nat. Phys.* **2**, 849 (2006).
- [67] A. Le Boité, G. Orso, and C. Ciuti, “Steady-State Phases and Tunneling-Induced Instabilities in the Driven Dissipative Bose-Hubbard Model,” *Phys. Rev. Lett.* **110**, 233601 (2013).
- [68] F. Vicentini, F. Minganti, R. Rota, G. Orso, and C. Ciuti, “Critical slowing down in driven-dissipative Bose-Hubbard lattices,” *Phys. Rev. A* **97**, 013853 (2018).
- [69] R. Ma, B. Saxberg, C. Owens, N. Leung, Y. Lu, J. Simon, and D. I. Schuster, “A dissipatively stabilized Mott insulator of photons,” *Nature* **566**, 51 (2019).
- [70] N. G. Berloff, M. Silva, K. Kalinin, A. Askitopoulos, J. D. Töpfer, P. Cilibrizzi, W. Langbein, and P. G. Lagoudakis, “Realizing the classical XY Hamiltonian in polariton simulators,” *Nat. Mater.* **16**, 1120 (2017).
- [71] K. P. Kalinin and N. G. Berloff, “Simulating Ising and n -State Planar Potts Models and External Fields with Nonequilibrium Condensates,” *Phys. Rev. Lett.* **121**, 235302 (2018).
- [72] K. P. Kalinin and N. G. Berloff, “Polaritonic network as a paradigm for dynamics of coupled oscillators,” *Phys. Rev. B* **100**, 245306 (2019).
- [73] K. P. Kalinin, A. Amo, J. Bloch, and N. G. Berloff, “Polaritonic XY-Ising machine,” *Nanophotonics* **9**, 4127 (2020).
- [74] A. Lucas, “Ising formulations of many NP problems,” *Front. Phys.* **2** (2014).
- [75] A. Opala, S. Ghosh, T. C. Liew, and M. Matuszewski, “Neuromorphic Computing in Ginzburg-Landau Polariton-Lattice Systems,” *Phys. Rev. Applied* **11**, 064029 (2019).
- [76] X. Liu, T. Galfsky, Z. Sun, F. Xia, E.-c. Lin, Y.-H. Lee, S. Kéna-Cohen, and V. M. Menon, “Strong light-matter coupling in two-dimensional atomic crystals,” *Nat. Photonics* **9**, 30 (2015).
- [77] C. P. Dietrich, A. Fiore, M. G. Thompson, M. Kamp, and S. Höfling, “GaAs integrated quantum photonics: Towards compact and multi-functional quantum photonic integrated circuits,” *Laser Photonics Rev.* **10**, 870 (2016).
- [78] R. Su, C. Diederichs, J. Wang, T. C. H. Liew, J. Zhao, S. Liu, W. Xu, Z. Chen, and Q. Xiong, “Room-Temperature Polariton Lasing in All-Inorganic Perovskite Nanoplatelets,” *Nano Lett.* **17**, 3982 (2017).
- [79] N. Carlon Zambon, P. St-Jean, M. Milićević, A. Lemaître, A. Harouri, L. Le Gratiet, O. Bleu, D. D. Solnyshkov, G. Malpuech, I. Sagnes, S. Ravets, A. Amo, and J. Bloch, “Optically controlling the emission chirality of microlasers,” *Nat. Photonics* **13**, 283 (2019).
- [80] D. Hunger, T. Steinmetz, Y. Colombe, C. Deutsch, T. W. Hänsch, and J. Reichel, “A fiber Fabry-Pérot cavity with high finesse,” *New J. Phys.* **12**, 065038 (2010).

-
- [81] S. Dufferwiel, S. Schwarz, F. Withers, A. A. P. Trichet, F. Li, M. Sich, O. Del Pozo-Zamudio, C. Clark, A. Nalitov, D. D. Solnyshkov, G. Malpuech, K. S. Novoselov, J. M. Smith, M. S. Skolnick, D. N. Krizhanovskii, and A. I. Tartakovskii, “Exciton–polaritons in van der Waals heterostructures embedded in tunable microcavities,” *Nat. Commun.* **6**, 8579 (2015).
- [82] H. Kaupp, T. Hümmer, M. Mader, B. Schlederer, J. Benedikter, P. Haeusser, H.-C. Chang, H. Fedder, T. W. Hänsch, and D. Hunger, “Purcell-Enhanced Single-Photon Emission from Nitrogen-Vacancy Centers Coupled to a Tunable Microcavity,” *Phys. Rev. Applied* **6**, 054010 (2016).
- [83] D. Wang, H. Kelkar, D. Martin-Cano, T. Utikal, S. Götzinger, and V. Sandoghdar, “Coherent Coupling of a Single Molecule to a Scanning Fabry-Pérot Microcavity,” *Phys. Rev. X* **7**, 021014 (2017).
- [84] S. Dufferwiel, T. P. Lyons, D. D. Solnyshkov, A. A. P. Trichet, F. Withers, S. Schwarz, G. Malpuech, J. M. Smith, K. S. Novoselov, M. S. Skolnick, D. N. Krizhanovskii, and A. I. Tartakovskii, “Valley-addressable polaritons in atomically thin semiconductors,” *Nat. Photonics* **11**, 497 (2017).
- [85] J. Benedikter, H. Kaupp, T. Hümmer, Y. Liang, A. Bommer, C. Becher, A. Krueger, J. M. Smith, T. W. Hänsch, and D. Hunger, “Cavity-Enhanced Single-Photon Source Based on the Silicon-Vacancy Center in Diamond,” *Phys. Rev. Applied* **7**, 024031 (2017).
- [86] D. Najer, I. Söllner, P. Sekatski, V. Dolique, M. C. Löbl, D. Riedel, R. Schott, S. Starosielec, S. R. Valentin, A. D. Wieck, N. Sangouard, A. Ludwig, and R. J. Warburton, “A gated quantum dot strongly coupled to an optical microcavity,” *Nature* **575**, 622 (2019).
- [87] H. A. Fernandez, F. Withers, S. Russo, and W. L. Barnes, “Electrically tuneable exciton energy exchange between spatially separated 2-dimensional semiconductors in a microcavity,” *Appl. Phys. Lett.* **115**, 071103 (2019).
- [88] H. A. Fernandez, F. Withers, S. Russo, and W. L. Barnes, “Electrically Tuneable Exciton-Polaritons through Free Electron Doping in Monolayer WS₂ Microcavities,” *Adv. Opt. Mater.* **7**, 1900484 (2019).
- [89] M. Vretenar, C. Toebes, and J. Klaers, “Modified Bose-Einstein condensation in an optical quantum gas,” *Nat. Commun.* **12**, 5749 (2021).
- [90] L. Lackner, M. Dusel, O. A. Egorov, B. Han, H. Knopf, F. Eilenberger, S. Schröder, K. Watanabe, T. Taniguchi, S. Tongay, C. Anton-Solanas, and C. Höfling S. Schneider, “Tunable exciton-polaritons emerging from WS₂ monolayer excitons in a photonic lattice at room temperature,” *Nat. Commun.* **12**, 4933 (2021).
- [91] M. Ruf, M. Weaver, S. van Dam, and R. Hanson, “Resonant Excitation and Purcell Enhancement of Coherent Nitrogen-Vacancy Centers Coupled to a Fabry-Pérot Microcavity,” *Phys. Rev. Applied* **15**, 024049 (2021).

- [92] A. A. P. Trichet, P. R. Dolan, D. M. Coles, G. M. Hughes, and J. M. Smith, "Topographic control of open-access microcavities at the nanometer scale," *Opt. Express* **23**, 17205 (2015).
- [93] P. D. Drummond and D. F. Walls, "Quantum theory of optical bistability. I. Nonlinear polarisability model," *J. Phys. A* **13**, 725 (1980).
- [94] H. Risken, C. Savage, F. Haake, and D. F. Walls, "Quantum tunneling in dispersive optical bistability," *Phys. Rev. A* **35**, 1729 (1987).
- [95] H. A. Haus, *Waves and Fields in Optoelectronics*. (Prentice-Hall, Englewood Cliffs, NJ, 1984).
- [96] E. P. Gross, "Structure of a quantized vortex in boson systems," *Nuovo Cimento (1955-1965)* **20**, 454 (1961).
- [97] L. Pitaevskii, "Vortex lines in an imperfect Bose gas," *Sov. Phys. JETP* **13**, 451 (1961).
- [98] G. Duffing, *Erzwungene schwingungen bei veränderlicher eigenfrequenz und ihre technische bedeutung* (F. Vieweg u. Sohn, Braunschweig, 1918).
- [99] A. H. Nayfeh and D. T. Mook, *Nonlinear Oscillations* (John Wiley & Sons, Ltd, 1995).
- [100] I. Kovacic and M. J. Brennan, *The Duffing Equation: Nonlinear Oscillators and their Behaviour* (John Wiley & Sons, Ltd, 2011).
- [101] D. Sarchi, I. Carusotto, M. Wouters, and V. Savona, "Coherent dynamics and parametric instabilities of microcavity polaritons in double-well systems," *Phys. Rev. B* **77**, 125324 (2008).
- [102] C. W. Gardiner and M. J. Collett, "Input and output in damped quantum systems: Quantum stochastic differential equations and the master equation," *Phys. Rev. A* **31**, 3761 (1985).
- [103] C. Gardiner and P. Zoller, *Quantum Noise* (Springer, Berlin, 2004).
- [104] N. Peyghambarian, H. M. Gibbs, M. C. Rushford, and D. A. Weinberger, "Observation of Biexcitonic Optical Bistability and Optical Limiting in CuCl," *Phys. Rev. Lett.* **51**, 1692 (1983).
- [105] V. R. Almeida and M. Lipson, "Optical bistability on a silicon chip," *Opt. Lett.* **29**, 2387 (2004).
- [106] K. Perrier, S. Greveling, H. Wouters, S. R. K. Rodriguez, G. Lehoucq, S. Combr  , A. de Rossi, S. Faez, and A. P. Mosk, "Thermo-optical dynamics of a nonlinear GaInP photonic crystal nanocavity depend on the optical mode profile," *OSA Continuum* **3**, 1879 (2020).
- [107] T. Carmon, L. Yang, and K. J. Vahala, "Dynamical thermal behavior and thermal self-stability of microcavities," *Opt. Express* **12**, 4742 (2004).

- [108] H. Rokhsari and K. J. Vahala, "Observation of Kerr nonlinearity in microcavities at room temperature," *Opt. Lett.* **30**, 427 (2005).
- [109] I. Grudinin, H. Lee, T. Chen, and K. J. Vahala, "Compensation of thermal nonlinearity effect in optical resonators," *Opt. Express* **19**, 7365 (2011).
- [110] D. Hohlfeld and H. Zappe, "An all-dielectric tunable optical filter based on the thermo-optic effect," *J. Opt. A: Pure Appl. Opt.* **6**, 504 (2004).
- [111] K. Cui, Q. Zhao, X. Feng, Y. Huang, Y. Li, D. Wang, and W. Zhang, "Thermo-optic switch based on transmission-dip shifting in a double-slot photonic crystal waveguide," *Appl. Phys. Lett.* **100**, 201102 (2012).
- [112] M. Radhouene, M. Najjar, M. K. Chhipa, S. Robinson, and B. Suthar, "Design and analysis a thermo-optic switch based on photonic crystal ring resonator," *Optik* **172**, 924 (2018).
- [113] Y. Tanaka, H. Kawashima, N. Ikeda, Y. Sugimoto, H. Kuwatsuka, T. Hasama, and H. Ishikawa, "Optical Bistable Operations in AlGaAs-Based Photonic Crystal Slab Microcavity at Telecommunication Wavelengths," *IEEE Photon. Technol. Lett.* **18**, 1996 (2006).
- [114] A. de Rossi, M. Lauritano, S. Combri , Q. V. Tran, and C. Husko, "Interplay of plasma-induced and fast thermal nonlinearities in a GaAs-based photonic crystal nanocavity," *Phys. Rev. A* **79**, 043818 (2009).
- [115] F. Ramiro-Manzano, N. Prtljaga, L. Pavesi, G. Pucker, and M. Ghulinyan, "Thermo-optical bistability with Si nanocrystals in a whispering gallery mode resonator," *Opt. Lett.* **38**, 3562 (2013).
- [116] L. Zhang, Y. Fei, Y. Cao, X. Lei, and S. Chen, "Experimental observations of thermo-optical bistability and self-pulsation in silicon microring resonators," *J. Opt. Soc. Am. B* **31**, 201 (2014).
- [117] R. F. Souza, M. A. Alencar, M. R. Meneghetti, and J. M. Hickmann, "Large nonlocal nonlinear optical response of castor oil," *Opt. Mater.* **31**, 1591 (2009).
- [118] A. Garc a, S. Valbuena, R. Sarmiento, and F. Racedo, "Measurement of the nonlinear optical properties of olive oil using Z-scan," *Opt. Pura Apl.* **48**, 55 (2015).
- [119] O. D. Marbello, S. Valbuena, and F. J. Racedo, "Study of the nonlinear optical response and thermal stability of edible oils using the Z-scan technique," *Talanta* **206**, 120226 (2020).
- [120] S. J. Sheldon, L. V. Knight, and J. M. Thorne, "Laser-induced thermal lens effect: a new theoretical model," *Appl. Opt.* **21**, 1663 (1982).
- [121] J. Bernal-Alvarado, A. M. Mansanares, E. C. da Silva, and S. G. C. Moreira, "Thermal diffusivity measurements in vegetable oils with thermal lens technique," *Rev. Sci. Instrum.* **74**, 697 (2003).

- [122] R. M. Stevenson, V. N. Astratov, M. S. Skolnick, D. M. Whittaker, M. Emam-Ismael, A. I. Tartakovskii, P. G. Savvidis, J. J. Baumberg, and J. S. Roberts, “Continuous Wave Observation of Massive Polariton Redistribution by Stimulated Scattering in Semiconductor Microcavities,” *Phys. Rev. Lett.* **85**, 3680 (2000).
- [123] H. Deng, G. Weihs, C. Santori, J. Bloch, and Y. Yamamoto, “Condensation of Semiconductor Microcavity Exciton Polaritons,” *Science* **298**, 199 (2002).
- [124] H. Deng, H. Haug, and Y. Yamamoto, “Exciton-polariton Bose-Einstein condensation,” *Rev. Mod. Phys.* **82**, 1489 (2010).
- [125] R. Su, S. Ghosh, J. Wang, S. Liu, C. Diederichs, T. C. H. Liew, and Q. Xiong, “Observation of exciton polariton condensation in a perovskite lattice at room temperature,” *Nat. Phys.* **16**, 301 (2020).
- [126] D. Bajoni, E. Semenova, A. Lemaître, S. Bouchoule, E. Wertz, P. Senellart, S. Barbay, R. Kuszelewicz, and J. Bloch, “Optical Bistability in a GaAs-Based Polariton Diode,” *Phys. Rev. Lett.* **101**, 266402 (2008).
- [127] R. Su, A. Fieramosca, Q. Zhang, H. S. Nguyen, E. Deleporte, Z. Chen, D. Sanvitto, T. C. H. Liew, and Q. Xiong, “Perovskite semiconductors for room-temperature exciton-polaritonics,” *Nat. Mater.* **20**, 1315 (2021).
- [128] A. V. Zasedatelev, A. V. Baranikov, D. Sannikov, D. Urbonas, F. Scafirimuto, V. Y. Shishkov, E. S. Andrianov, Y. E. Lozovik, U. Scherf, T. Stöferle, R. F. Mahrt, and P. G. Lagoudakis, “Single-photon nonlinearity at room temperature,” *Nature* **597**, 493 (2021).
- [129] R. Graham and H. Haken, “Laserlight—first example of a second-order phase transition far away from thermal equilibrium,” *Z. Phys.* **237**, 31 (1970).
- [130] R. Roy and L. Mandel, “Optical bistability and first order phase transition in a ring dye laser,” *Opt. Commun.* **34**, 133 (1980).
- [131] M. O. Scully, “Condensation of N Bosons and the Laser Phase Transition Analogy,” *Phys. Rev. Lett.* **82**, 3927 (1999).
- [132] H. J. Carmichael, “Breakdown of Photon Blockade: A Dissipative Quantum Phase Transition in Zero Dimensions,” *Phys. Rev. X* **5**, 031028 (2015).
- [133] J. J. Mendoza-Arenas, S. R. Clark, S. Felicetti, G. Romero, E. Solano, D. G. Angelakis, and D. Jaksch, “Beyond mean-field bistability in driven-dissipative lattices: Bunching-antibunching transition and quantum simulation,” *Phys. Rev. A* **93**, 023821 (2016).
- [134] M. Fitzpatrick, N. M. Sundaresan, A. C. Y. Li, J. Koch, and A. A. Houck, “Observation of a Dissipative Phase Transition in a One-Dimensional Circuit QED Lattice,” *Phys. Rev. X* **7**, 011016 (2017).

-
- [135] J. M. Fink, A. Dombi, A. Vukics, A. Wallraff, and P. Domokos, “Observation of the Photon-Blockade Breakdown Phase Transition,” *Phys. Rev. X* **7**, 011012 (2017).
- [136] M. Biondi, G. Blatter, H. E. Türeci, and S. Schmidt, “Nonequilibrium gas-liquid transition in the driven-dissipative photonic lattice,” *Phys. Rev. A* **96**, 043809 (2017).
- [137] A. Angerer, S. Putz, D. O. Krimer, T. Astner, M. Zens, R. Glattauer, K. Streltsov, W. J. Munro, K. Nemoto, S. Rotter, J. Schmiedmayer, and J. Majer, “Ultralong relaxation times in bistable hybrid quantum systems,” *Sci. Adv.* **3**, e1701626 (2017).
- [138] D. O. Krimer and M. Pletyukhov, “Few-Mode Geometric Description of a Driven-Dissipative Phase Transition in an Open Quantum System,” *Phys. Rev. Lett.* **123**, 110604 (2019).
- [139] S. Finazzi, A. Le Boité, F. Storme, A. Baksic, and C. Ciuti, “Corner-Space Renormalization Method for Driven-Dissipative Two-Dimensional Correlated Systems,” *Phys. Rev. Lett.* **115**, 080604 (2015).
- [140] L. M. Sieberer, M. Buchhold, and S. Diehl, “Keldysh field theory for driven open quantum systems,” *Rep. Prog. Phys.* **79**, 096001 (2016).
- [141] M. J. Hartmann, “Quantum simulation with interacting photons,” *J. Opt.* **18**, 104005 (2016).
- [142] T. Leleu, Y. Yamamoto, S. Utsunomiya, and K. Aihara, “Combinatorial optimization using dynamical phase transitions in driven-dissipative systems,” *Phys. Rev. E* **95**, 022118 (2017).
- [143] T. Leleu, Y. Yamamoto, P. L. McMahon, and K. Aihara, “Destabilization of Local Minima in Analog Spin Systems by Correction of Amplitude Heterogeneity,” *Phys. Rev. Lett.* **122**, 040607 (2019).
- [144] F. Dalfovo, S. Giorgini, L. P. Pitaevskii, and S. Stringari, “Theory of Bose-Einstein condensation in trapped gases,” *Rev. Mod. Phys.* **71**, 463 (1999).
- [145] V. L. Ginzburg and L. D. Landau, “On the Theory of Superconductivity,” in *On Superconductivity and Superfluidity: A Scientific Autobiography* (Springer Berlin Heidelberg, 2009), pp. 113–137.
- [146] L. A. Lugiato and R. Lefever, “Spatial Dissipative Structures in Passive Optical Systems,” *Phys. Rev. Lett.* **58**, 2209 (1987).
- [147] J. Goldstone, “Field theories with « Superconductor » solutions,” *Nuovo Cimento (1955-1965)* **19**, 154 (1961).
- [148] G. Priem, D. P. B. W., T. D. Van, G. Morthier, and R. Baets, “Optical bistability and pulsating behaviour in Silicon-On-Insulator ring resonator structures,” *Opt. Express* **13**, 9623 (2005).

- [149] Y. Shi, X. Chen, F. Lou, Y. Chen, M. Yan, L. Wosinski, and M. Qiu, "All-optical switching of silicon disk resonator based on photothermal effect in metal-insulator-metal absorber," *Opt. Lett.* **39**, 4431 (2014).
- [150] M. Brunstein, R. Braive, R. Hostein, A. Beveratos, I. Robert-Philip, I. Sagnes, T. J. Karle, A. M. Yacomotti, J. A. Levenson, V. Moreau, G. Tessier, and Y. D. Wilde, "Thermo-optical dynamics in an optically pumped photonic crystal nano-cavity," *Opt. Express* **17**, 17118 (2009).
- [151] M. Sodagar, M. Miri, A. A. Eftekhar, and A. Adibi, "Optical bistability in a one-dimensional photonic crystal resonator using a reverse-biased pn-junction," *Opt. Express* **23**, 2676 (2015).
- [152] K. P. Kalinin and N. G. Berloff, "Simulating Ising and n -State Planar Potts Models and External Fields with Nonequilibrium Condensates," *Phys. Rev. Lett.* **121**, 235302 (2018).
- [153] P. Jung, G. Gray, R. Roy, and P. Mandel, "Scaling Law for Dynamical Hysteresis," *Phys. Rev. Lett.* **65**, 1873 (1990).
- [154] L. Pickup, K. Kalinin, A. Askitopoulos, Z. Hatzopoulos, P. G. Savvidis, N. G. Berloff, and P. G. Lagoudakis, "Optical Bistability under Nonresonant Excitation in Spinor Polariton Condensates," *Phys. Rev. Lett.* **120**, 225301 (2018).
- [155] S. Johnson, "The Coupling of Nitrogen-Vacancy Centres in Diamond to tunable Open-Microcavities," PhD thesis (University of Oxford) (2015).
- [156] A. Dreischuh, D. N. Neshev, D. E. Petersen, O. Bang, and W. Krolikowski, "Observation of Attraction between Dark Solitons," *Phys. Rev. Lett.* **96**, 043901 (2006).
- [157] H. Abbaspour, G. Sallen, S. Trebaol, F. Morier-Genoud, M. T. Portella-Oberli, and B. Deveaud, "Effect of a noisy driving field on a bistable polariton system," *Phys. Rev. B* **92**, 165303 (2015).
- [158] S. A. Khodier, "Refractive index of standard oils as a function of wavelength and temperature," *Opt. Laser Technol.* **34**, 125 (2002).
- [159] H. Mori, "Transport, collective motion, and Brownian motion," *Prog. Theor. Phys.* **33**, 423 (1965).
- [160] P. Hänggi, "Correlation functions and masterequations of generalized (non-Markovian) Langevin equations," *Z. Phys. B* **31**, 407 (1978).
- [161] A. Hohl, H. J. C. van der Linden, R. Roy, G. Goldsztein, F. Broner, and S. H. Strogatz, "Scaling Laws for Dynamical Hysteresis in a Multidimensional Laser System," *Phys. Rev. Lett.* **74**, 2220 (1995).
- [162] I. Goychuk and P. Hänggi, "Non-Markovian Stochastic Resonance," *Phys. Rev. Lett.* **91**, 070601 (2003).
- [163] P. Hänggi and F. Mojtabai, "Thermally activated escape rate in presence of long-time memory," *Phys. Rev. A* **26**, 1168 (1982).

-
- [164] A. V. Mokshin, R. M. Yulmetyev, and P. Hänggi, “Simple Measure of Memory for Dynamical Processes Described by a Generalized Langevin Equation,” *Phys. Rev. Lett.* **95**, 200601 (2005).
- [165] R. L. S. Farias, R. O. Ramos, and L. A. da Silva, “Numerical solutions for non-Markovian stochastic equations of motion,” *Comput. Phys. Commun.* **180**, 574 (2009).
- [166] R. L. S. Farias, R. O. Ramos, and L. A. da Silva, “Stochastic Langevin equations: Markovian and non-Markovian dynamics,” *Phys. Rev. E* **80**, 031143 (2009).
- [167] D. Nagy and P. Domokos, “Nonequilibrium Quantum Criticality and Non-Markovian Environment: Critical Exponent of a Quantum Phase Transition,” *Phys. Rev. Lett.* **115**, 043601 (2015).
- [168] J. Marino and S. Diehl, “Driven Markovian Quantum Criticality,” *Phys. Rev. Lett.* **116**, 070407 (2016).
- [169] T. Speck and U. Seifert, “The Jarzynski relation, fluctuation theorems, and stochastic thermodynamics for non-Markovian processes,” *J. Stat. Mech.* **2007**, L09002 (2007).
- [170] A. Kutvonen, T. Ala-Nissila, and J. Pekola, “Entropy production in a non-Markovian environment,” *Phys. Rev. E* **92**, 012107 (2015).
- [171] S. Deffner and E. Lutz, “Quantum Speed Limit for Non-Markovian Dynamics,” *Phys. Rev. Lett.* **111**, 010402 (2013).
- [172] S. Dufferwiel, F. Li, A. A. P. Trichet, L. Giriunas, P. M. Walker, I. Farrer, D. A. Ritchie, J. M. Smith, M. S. Skolnick, and D. N. Krizhanovskii, “Tunable polaritonic molecules in an open microcavity system,” *Appl. Phys. Lett.* **107**, 201106 (2015).
- [173] W. L. Barnes, A. Dereux, and T. W. Ebbesen, “Surface plasmon subwavelength optics,” *Nature* **424**, 824 (2003).
- [174] G. Deka, C. Sun, K. Fujita, and S. Chu, “Nonlinear plasmonic imaging techniques and their biological applications,” *Nanophotonics* **6**, 31 (2017).
- [175] S. Chen, G. Li, F. Zeuner, W. Wong, E. Y. B. Pun, T. Zentgraf, K. W. Cheah, and S. Zhang, “Symmetry-Selective Third-Harmonic Generation from Plasmonic Metacrystals,” *Phys. Rev. Lett.* **113**, 033901 (2014).
- [176] J. Butet, P. F. Brevet, and O. J. F. Martin, “Optical Second Harmonic Generation in Plasmonic Nanostructures: From Fundamental Principles to Advanced Applications,” *ACS Nano* **9**, 10545 (2015).
- [177] P. Ghenuche, S. Cherukulappurath, T. H. Taminiau, N. F. van Hulst, and R. Quidant, “Spectroscopic Mode Mapping of Resonant Plasmon Nanoantennas,” *Phys. Rev. Lett.* **101**, 116805 (2008).

- [178] S. Palomba and L. Novotny, “Nonlinear Excitation of Surface Plasmon Polaritons by Four-Wave Mixing,” *Phys. Rev. Lett.* **101**, 056802 (2008).
- [179] M. Mutlu, J. Kang, S. Raza, D. Schoen, X. Zheng, P. G. Kik, and M. L. Brongersma, “Thermoplasmonic Ignition of Metal Nanoparticles,” *Nano Lett.* **18**, 1699 (2018).
- [180] D. L. Sounas and A. Alù, “Fundamental bounds on the operation of Fano nonlinear isolators,” *Phys. Rev. B* **97**, 115431 (2018).
- [181] T. W. Hughes, I. A. D. Williamson, M. Minkov, and S. Fan, “Wave physics as an analog recurrent neural network,” *Sci. Adv.* **5**, eaay6946 (2019).
- [182] G. A. Wurtz, R. Pollard, and A. V. Zayats, “Optical Bistability in Nonlinear Surface-Plasmon Polaritonic Crystals,” *Phys. Rev. Lett.* **97**, 057402 (2006).
- [183] J. Li, X. Lü, J. Luo, and Q. Huang, “Optical bistability and multistability via atomic coherence in an N -type atomic medium,” *Phys. Rev. A* **74**, 035801 (2006).
- [184] A. V. Malyshev and V. A. Malyshev, “Optical bistability and hysteresis of a hybrid metal-semiconductor nanodimer,” *Phys. Rev. B* **84**, 035314 (2011).
- [185] N. M. R. Peres, Y. V. Bludov, J. E. Santos, A.-P. Jauho, and M. I. Vasilevskiy, “Optical bistability of graphene in the terahertz range,” *Phys. Rev. B* **90**, 125425 (2014).
- [186] D. N. Maksimov, A. A. Bogdanov, and E. N. Bulgakov, “Optical bistability with bound states in the continuum in dielectric gratings,” *Phys. Rev. A* **102**, 033511 (2020).
- [187] J. A. Porto, L. Martín-Moreno, and F. J. García-Vidal, “Optical bistability in subwavelength slit apertures containing nonlinear media,” *Phys. Rev. B* **70**, 081402 (2004).
- [188] X. Wang, H. Jiang, J. Chen, P. Wang, Y. Lu, and H. Ming, “Optical bistability effect in plasmonic racetrack resonator with high extinction ratio,” *Opt. Express* **19**, 19415 (2011).
- [189] T. Christensen, W. Yan, A. P. Jauho, M. Wubs, and N. A. Mortensen, “Kerr nonlinearity and plasmonic bistability in graphene nanoribbons,” *Phys. Rev. B* **92**, 121407 (2015).
- [190] X. C. Jiang, Y. W. Zhou, D. L. Gao, Y. Huang, and L. Gao, “Realizing optical bistability and tristability in plasmonic coated nanoparticles with radial-anisotropy and kerr-nonlinearity,” *Opt. Express* **28**, 17384 (2020).
- [191] F. Broner, G. H. Goldsztein, and S. H. Strogatz, “Dynamical Hysteresis without Static Hysteresis: Scaling Laws and Asymptotic Expansions,” *SIAM J. Appl. Math.* **57**, 1163 (1997).
- [192] S. Lynch, *Dynamical Systems with Applications using MATLAB®*, Second Edition (Birkhäuser, Cham, 2014).

- [193] B. Shi, L. Duan, Y. Zhao, J. Luo, and X. Zhang, "Semitransparent Perovskite Solar Cells: From Materials and Devices to Applications," *Adv. Mater.* **32**, 1806474 (2020).
- [194] X. Li, Y. Wu, S. Zhang, B. Cai, Y. Gu, J. Song, and H. Zeng, "CsPbX₃ Quantum Dots for Lighting and Displays: Room-Temperature Synthesis, Photoluminescence Superiorities, Underlying Origins and White Light-Emitting Diodes," *Adv. Funct. Mater.* **26**, 2435 (2016).
- [195] L. Protesescu, S. Yakunin, M. I. Bodnarchuk, F. Krieg, R. Caputo, C. H. Hendon, R. X. Yang, A. Walsh, and M. V. Kovalenko, "Nanocrystals of Cesium Lead Halide Perovskites (CsPbX₃, X = Cl, Br, and I): Novel Optoelectronic Materials Showing Bright Emission with Wide Color Gamut," *Nano Lett.* **15**, 3692 (2015).
- [196] X. Hu, X. Zhang, L. Liang, J. Bao, S. Li, W. Yang, and Y. Xie, "High-Performance Flexible Broadband Photodetector Based on Organolead Halide Perovskite," *Adv. Funct. Mater.* **24**, 7373 (2014).
- [197] Photovoltaic Research, "Best Research-Cell Efficiency Chart," NREL (2021).
- [198] M. Yuan, L. N. Quan, R. Comin, G. Walters, R. Sabatini, O. Voznyy, S. Hoogland, Y. Zhao, E. M. Beauregard, P. Kanjanaboos, Z. Lu, D. H. Kim, and E. H. Sargent, "Perovskite energy funnels for efficient light-emitting diodes," *Nat. Nanotechnol.* **11**, 872 (2016).
- [199] C. Huang, W. Sun, Y. Fan, Y. Wang, Y. Gao, N. Zhang, K. Wang, S. Liu, S. Wang, S. Xiao, and Q. Song, "Formation of Lead Halide Perovskite Based Plasmonic Nanolasers and Nanolaser Arrays by Tailoring the Substrate," *ACS Nano* **12**, 3865 (2018).
- [200] L. Dou, Y. Yang, J. You, Z. Hong, W.-H. Chang, G. Li, and Y. Yang, "Solution-processed hybrid perovskite photodetectors with high detectivity," *Nat. Commun.* **5**, 5404 (2014).
- [201] H. Wei, Y. Fang, P. Mulligan, W. Chuirazzi, H.-H. Fang, C. Wang, B. R. Ecker, Y. Gao, M. A. Loi, L. Cao, and J. Huang, "Sensitive X-ray detectors made of methylammonium lead tribromide perovskite single crystals," *Nat. Photonics* **10**, 333 (2016).
- [202] A. Brehier, R. Parashkov, J. S. Lauret, and E. Deleporte, "Strong exciton-photon coupling in a microcavity containing layered perovskite semiconductors," *Appl. Phys. Lett.* **89**, 171110 (2006).
- [203] Q. Shang, S. Zhang, Z. Liu, J. Chen, P. Yang, C. Li, W. Li, Y. Zhang, Q. Xiong, X. Liu, and Q. Zhang, "Surface Plasmon Enhanced Strong Exciton-Photon Coupling in Hybrid Inorganic-Organic Perovskite Nanowires," *Nano Lett.* **18**, 3335 (2018).

- [204] W. Bao, X. Liu, F. Xue, F. Zheng, R. Tao, S. Wang, Y. Xia, M. Zhao, J. Kim, S. Yang, Q. Li, Y. Wang, Y. Wang, L.-W. Wang, A. H. MacDonald, and X. Zhang, "Observation of Rydberg exciton polaritons and their condensate in a perovskite cavity," *PNAS* **116**, 20274 (2019).
- [205] L. Polimeno, A. Fieramosca, G. Lerario, M. Cinquino, M. De Giorgi, D. Ballarini, F. Todisco, L. Dominici, V. Ardizzone, M. Pugliese, C. T. Prontera, V. Maiorano, G. Gigli, L. De Marco, and D. Sanvitto, "Observation of Two Thresholds Leading to Polariton Condensation in 2D Hybrid Perovskites," *Adv. Opt. Mater.* **8**, 2000176 (2020).
- [206] A. Fieramosca, L. Polimeno, V. Ardizzone, L. De Marco, M. Pugliese, V. Maiorano, M. De Giorgi, L. Dominici, G. Gigli, D. Gerace, D. Ballarini, and D. Sanvitto, "Two-dimensional hybrid perovskites sustaining strong polariton interactions at room temperature," *Sci. Adv.* **5**, eaav9967 (2019).
- [207] A. E. Miroshnichenko, S. Flach, and Y. S. Kivshar, "Fano resonances in nanoscale structures," *Rev. Mod. Phys.* **82**, 2257 (2010).
- [208] B. Luk'yanchuk, N. I. Zheludev, S. A. Maier, N. J. Halas, P. Nordlander, H. Giessen, and C. T. Chong, "The Fano resonance in plasmonic nanostructures and metamaterials," *Nat. Mater.* **9**, 707 (2010).
- [209] P. Törma and W. L. Barnes, "Strong coupling between surface plasmon polaritons and emitters: a review," *Rep. Prog. Phys.* **78**, 013901 (2014).
- [210] M. F. Limonov, M. V. Rybin, A. N. Poddubny, and Y. S. Kivshar, "Fano resonances in photonics," *Nat. Photonics* **11**, 543 (2017).
- [211] C. L. Garrido Alzar, M. A. G. Martinez, and P. Nussenzevig, "Classical analog of electromagnetically induced transparency," *Am. J. Phys.* **70**, 37 (2002).
- [212] Y. S. Joe, A. M. Satanin, and C. S. Kim, "Classical analogy of Fano resonances," *Phys. Scr.* **74**, 259 (2006).
- [213] S. R. K. Rodriguez, "Classical and quantum distinctions between weak and strong coupling," *Eur. J. Phys.* **37**, 025802 (2016).
- [214] F. Hao, Y. Sonnefraud, P. V. Dorpe, S. A. Maier, N. J. Halas, and P. Nordlander, "Symmetry Breaking in Plasmonic Nanocavities: Subradiant LSPR Sensing and a Tunable Fano Resonance," *Nano Lett.* **8**, 3983 (2008).
- [215] P. Offermans, M. C. Schaafsma, S. R. K. Rodriguez, Y. Zhang, M. Crego-Calama, S. H. Brongersma, and J. Gómez Rivas, "Universal Scaling of the Figure of Merit of Plasmonic Sensors," *ACS Nano* **5**, 5151 (2011).
- [216] Y. Yu, M. Heuck, H. Hu, W. Xue, C. Peucheret, Y. Chen, L. K. Oxenløwe, K. Yvind, and J. Mørk, "Fano resonance control in a photonic crystal structure and its application to ultrafast switching," *Appl. Phys. Lett.* **105**, 061117 (2014).

- [217] S. N. Sheikholeslami, A. García-Etxarri, and J. A. Dionne, “Controlling the Interplay of Electric and Magnetic Modes via Fano-like Plasmon Resonances,” *Nano Lett.* **11**, 3927 (2011).
- [218] C. Yan, K. Y. Yang, and O. J. F. Martin, “Fano-resonance-assisted metasurface for color routing,” *Light Sci. Appl.* **6**, e17017 (2017).
- [219] H. M. Doeleman, C. D. Dieleman, C. Mennes, B. Ehrler, and A. F. Koenderink, “Observation of Cooperative Purcell Enhancements in Antenna–Cavity Hybrids,” *ACS Nano* **14**, 12027 (2020).
- [220] Y. Yu, W. Xue, E. Semenova, K. Yvind, and J. Mørk, “Demonstration of a self-pulsing photonic crystal Fano laser,” *Nat. Photonics* **11**, 81 (2017).
- [221] K. Y. Yang, J. Skarda, M. Cotrufo, A. Dutt, G. H. Ahn, M. Sawaby, D. Ver-cruyse, A. Arbabian, S. Fan, A. Alù, and J. Vučković, “Inverse-designed non-reciprocal pulse router for chip-based lidar,” *Nat. Photonics* **14**, 369 (2020).
- [222] J. A. Hutchison, T. Schwartz, C. Genet, E. Devaux, and T. W. Ebbesen, “Modifying Chemical Landscapes by Coupling to Vacuum Fields,” *Angew. Chem. Int. Ed* **51**, 1592 (2012).
- [223] J. Feist, J. Galego, and F. J. Garcia-Vidal, “Polaritonic Chemistry with Organic Molecules,” *ACS Photonics* **5**, 205 (2018).
- [224] F. P. Laussy, A. V. Kavokin, and I. A. Shelykh, “Exciton-Polariton Mediated Superconductivity,” *Phys. Rev. Lett.* **104**, 106402 (2010).
- [225] E. Orgiu, J. George, J. A. Hutchison, E. Devaux, J. F. Dayen, B. Doudin, F. Stellacci, C. Genet, J. Schachenmayer, C. Genes, G. Pupillo, P. Samorí, and T. W. Ebbesen, “Conductivity in organic semiconductors hybridized with the vacuum field,” *Nat. Mater.* **14**, 1123 (2015).
- [226] D. M. Coles, Y. Yang, Y. Wang, R. T. Grant, R. A. Taylor, S. K. Saikin, A. Aspuru-Guzik, D. G. Lidzey, J. K.-H. Tang, and J. M. Smith, “Strong coupling between chlorosomes of photosynthetic bacteria and a confined optical cavity mode,” *Nat. Commun.* **5**, 5561 (2014).
- [227] M. Ramezani, A. Halpin, A. I. Fernández-Domínguez, J. Feist, S. R. K. Rodriguez, F. J. Garcia-Vidal, and J. Gómez Rivas, “Plasmon-exciton-polariton lasing,” *Optica* **4**, 31 (2017).
- [228] V. Savona, L. C. Andreani, P. Schwendimann, and A. Quattropani, “Quantum well excitons in semiconductor microcavities: Unified treatment of weak and strong coupling regimes,” *Solid State Commun.* **93**, 733 (1995).
- [229] T. Schwartz, J. A. Hutchison, C. Genet, and T. W. Ebbesen, “Reversible Switching of Ultrastrong Light-Molecule Coupling,” *Phys. Rev. Lett.* **106**, 196405 (2011).

- [230] D. Melnikau, R. Esteban, D. Savateeva, A. Sánchez-Iglesias, M. Grzelczak, M. K. Schmidt, L. M. Liz-Marzán, J. Aizpurua, and Y. P. Rakovich, “Rabi Splitting in Photoluminescence Spectra of Hybrid Systems of Gold Nanorods and J-Aggregates,” *J. Phys. Chem. Lett.* **7**, 354 (2016).
- [231] S. R. K. Rodriguez, S. Murai, M. A. Verschuuren, and J. Gómez Rivas, “Light-Emitting Waveguide-Plasmon Polaritons,” *Phys. Rev. Lett.* **109**, 166803 (2012).
- [232] W. Du, S. Zhang, J. Shi, J. Chen, Z. Wu, Y. Mi, Z. Liu, Y. Li, X. Sui, R. Wang, X. Qiu, T. Wu, Y. Xiao, Q. Zhang, and X. Liu, “Strong Exciton–Photon Coupling and Lasing Behavior in All-Inorganic CsPbBr₃ Micro/Nanowire Fabry-Pérot Cavity,” *ACS Photonics* **5**, 2051 (2018).
- [233] Q. Zhang, R. Su, X. Liu, J. Xing, T. C. Sum, and Q. Xiong, “High-Quality Whispering-Gallery-Mode Lasing from Cesium Lead Halide Perovskite Nanoplatelets,” *Adv. Funct. Mater.* **26**, 6238 (2016).
- [234] X. Chen, Y. Wang, J. Song, X. Li, J. Xu, H. Zeng, and H. Sun, “Temperature Dependent Reflectance and Ellipsometry Studies on a CsPbBr₃ Single Crystal,” *J. Phys. Chem. C* **123**, 10564 (2019).
- [235] H. Deng, H. Haug, and Y. Yamamoto, “Exciton-polariton Bose-Einstein condensation,” *Rev. Mod. Phys.* **82**, 1489 (2010).
- [236] T. Byrnes, N. Y. Kim, and Y. Yamamoto, “Exciton-polariton condensates,” *Nat. Phys.* **10**, 803 (2014).
- [237] S. R. K. Rodriguez, A. Amo, I. Sagnes, L. Le Gratiet, E. Galopin, A. Lemaître, and J. Bloch, “Interaction-induced hopping phase in driven-dissipative coupled photonic microcavities,” *Nat. Commun.* **7**, 11887 (2016).
- [238] J. Kasprzak, M. Richard, S. Kundermann, A. Baas, P. Jeambrun, J. M. J. Keeling, F. M. Marchetti, M. H. Szymańska, R. André, J. L. Staehli, V. Savona, P. B. Littlewood, B. Deveaud, and L. Dang, “Bose–Einstein condensation of exciton polaritons,” *Nature* **443**, 409 (2006).
- [239] J. Kasprzak, M. Richard, A. Baas, B. Deveaud, R. André, J. P. Poizat, and L. Dang, “Second-Order Time Correlations within a Polariton Bose-Einstein Condensate in a CdTe Microcavity,” *Phys. Rev. Lett.* **100**, 067402 (2008).
- [240] T. Guillet, M. Mexis, J. Levrat, G. Rossbach, C. Brimont, T. Bretagnon, B. Gil, R. Butté, N. Grandjean, L. Orosz, F. Réveret, J. Leymarie, J. Zúñiga-Pérez, M. Leroux, F. Semond, and S. Bouchoule, “Polariton lasing in a hybrid bulk ZnO microcavity,” *Appl. Phys. Lett.* **99**, 161104 (2011).
- [241] F. Li, L. Orosz, O. Kamoun, S. Bouchoule, C. Brimont, P. Disseix, T. Guillet, X. Lafosse, M. Leroux, J. Leymarie, M. Mexis, M. Mihailovic, G. Patriarche, F. Réveret, D. Solnyshkov, J. Zuniga-Perez, and G. Malpuech, “From Excitonic to Photonic Polariton Condensate in a ZnO-Based Microcavity,” *Phys. Rev. Lett.* **110**, 196406 (2013).

- [242] D. Sanvitto and S. Kéna-Cohen, “The road towards polaritonic devices,” *Nat. Mater.* **15**, 1061 (2016).
- [243] C. Ciuti, V. Savona, C. Piermarocchi, A. Quattropani, and P. Schwendimann, “Role of the exchange of carriers in elastic exciton-exciton scattering in quantum wells,” *Phys. Rev. B* **58**, 7926 (1998).
- [244] T. Kazimierczuk, D. Fröhlich, S. Scheel, H. Stolz, and M. Bayer, “Giant Rydberg excitons in the copper oxide Cu_2O ,” *Nature* **514**, 343 (2014).
- [245] Y. Fontana, R. Zifkin, E. Janitz, C. D. Rodríguez Rosenblueth, and L. Childress, “A mechanically stable and tunable cryogenic Fabry–Pérot microcavity,” *Rev. Sci. Instrum.* **92**, 053906 (2021).

Summary

Control and manipulation of light is key to many information and communication technologies. Despite the many impressive achievements in this direction, many information-processing functionalities are still missing in all-optical devices. These missing functionalities are mostly related to the fact that photons in linear media do not mutually interact. Consequently, in linear media light cannot generally be controlled with light. Nonlinear media offer a solution to this problem, by mediating effective photon-photon interactions. However, in weakly nonlinear media extreme excitation densities are required, while highly nonlinear media are often difficult (if not currently impossible) to integrate with other existing technologies like cavities or resonators. In this thesis, we explore ways to overcome these issues. We present experiments with open-access tunable cavities which allow easy integration of materials inside, while storing light for a long time so that it may interact with the material of choice. We focus on two particular nonlinear media, where the nonlinear response can have different origins. In Chapters 2 and 3 we couple resonators to oils. Oils provide a strong albeit slow room-temperature thermo-optical nonlinearity, which enabled us to discover novel behavior. In Chapters 4 and 5 we explore semiconductor cavities in the strong light-matter coupling regime. Therein, since the relevant quasi-particles are cavity polaritons formed by strong exciton-photon coupling, optical nonlinearity due to polariton-polariton interactions can emerge.

Chapter 1 introduces our motivation for studying the physics of tunable nonlinear optical cavities. We introduce a simple model to understand the behavior of light in a nonlinear optical cavity, and the phenomenon of optical bistability: two steady states at a single driving condition. We also discuss our two experimental approaches to get strong optical nonlinearity in experiments presented in subsequent chapters.

In Chapter 2 we experimentally and theoretically investigate the dynamics of a laser-driven oil-filled cavity with non-instantaneous nonlinearity. In measurements where the laser-cavity detuning is scanned at different speeds across the optical bistability, we find that the hysteresis area is a non-monotonic function of the scanning speed. In the fast-speed limit where the scanning time is comparable to the memory time of the nonlinearity, we discover that the hysteresis area decays following a universal scaling law with exponent -1 . Furthermore, we also discover signatures of non-Markovian dynamics emerging from the effects of memory and white noise.

Chapter 3 presents a series of experiments on a laser-driven metallic grating covered with an oil layer. For sufficiently large laser powers, we observe optical bistability in the laser transmission, and self-sustained oscillations in the diffracted intensities by the grating -1 and $+1$ diffraction orders. Also, the diffracted intensities display various dynamical regimes. These include regimes of spontaneous symmetry-breaking, where the diffracted intensities by the grating -1 and $+1$ diffraction orders are different even

though the system and the excitation are mirror-symmetric. Finally, we also discover spontaneous oscillations in all observables. These manifest as triangular waves in laser transmission, and as periodic spikes in the diffracted intensities, all in synchrony.

In Chapter 4 we study strong light-matter coupling in a tunable Fabry-Perot cavity containing a CsPbBr₃ perovskite crystal. We discover spectral lineshapes resembling Fano resonance and Rabi splittings (signatures of coherent coupling between subsystems), but which are neither. We find these effects in transmittance and photoluminescence measurements with objectives of different numerical aperture. Our measurements show that even a modest numerical aperture can result in spectral artefacts resembling Fano resonances and Rabi splittings. The results in this chapter reveal a possible systematic error that may have been overlooked in experiments where dispersive optical systems are characterized with high numerical aperture objectives. Finally, we provide a general guideline to avoid these pitfalls in the experiments involving such optical systems.

In Chapter 5 we present our efforts to construct and characterize a tunable cavity setup in a closed-cycle cryostat, and to use this setup to probe the nonlinear optical response of a CsPbBr₃ perovskite semiconductor. We focus on characterizing the mechanical stability of the cavity by measuring the transmitted intensity of a laser. We find that the presence of the mechanical fluctuations induced by the cryo-cooler motion strongly affects the cavity setup. We could nevertheless obtain meaningful experimental results either by performing fast measurements (avoiding the effects of the slow mechanical fluctuations), or by temporarily turning off the cryo-cooler. Through the former approach, we observe a highly nonlinear response of light in a plano-concave cavity with a CsPbBr₃ perovskite crystal inside. In fact, we demonstrate the first observation of optical bistability in any perovskite system.

Samenvatting

Beheersing en manipulatie van licht is essentieel voor vele informatie- en communicatietechnologieën. Ondanks de vele indrukwekkende successen in deze richting, missen er nog altijd veel functionaliteiten in het arsenaal van optische technologie om volledig optische informatieverwerking mogelijk te maken. Deze missende functionaliteiten zijn voornamelijk gerelateerd aan het feit dat fotonen in lineaire media geen interactie met elkaar hebben. Hierdoor kan licht in lineaire media niet gemanipuleerd worden met licht. Niet-lineaire media bieden een oplossing voor dit probleem door effectieve foton-foton interacties over te dragen. In zwakke niet-lineaire media zijn echter extreem intense lichtvelden nodig, terwijl zeer niet-lineaire media vaak moeilijk (zo niet onmogelijk) te integreren zijn met bestaande technologieën zoals optische trilholttes of resonatoren. In deze thesis onderzoeken we mogelijke oplossingen voor deze moeilijkheden. We laten experimenten zien met vrij-toegankelijke en verstembare trilholttes, waarin eenvoudig verschillende materialen geïntegreerd kunnen worden. Tegelijkertijd wordt het licht voor lange tijd in de holte gevangen, zodat de interactie met het materiaal naar keuze versterkt wordt. We richten ons specifiek op twee verschillende niet-lineaire media, waarbij de niet-lineaire respons een verschillende oorsprong heeft. In Hoofdstukken 2 en 3 koppelen we resonatoren aan olies. Olies bieden een sterke maar langzame thermo-optische niet-lineariteit op kamertemperatuur. In Hoofdstukken 4 en 5 onderzoeken we optische trilholttes met halfgeleiders in het regime van sterke licht-materie koppeling. De relevante quasideeltjes zijn polaritonen gevormd door een sterke exciton-foton koppeling. Hierdoor kan een optische niet-lineariteit worden verkregen door polariton-polariton interacties.

Hoofdstuk 1 beschrijft onze motivatie voor het bestuderen van de natuurkunde van verstembare niet-lineaire optische trilholttes. We beschrijven een eenvoudig model om het gedrag van licht in een niet-lineaire optische trilholte te begrijpen. Daarnaast introduceren we het concept van optische bistabiliteit: twee stabiele toestanden die tegelijk bestaan onder dezelfde excitatie omstandigheden. Ook behandelen we de technieken voor het verkrijgen van een sterke niet-lineariteit als omschreven in de volgende hoofdstukken.

In Hoofdstuk 2 onderzoeken we, zowel experimenteel als theoretisch, de dynamica van een optische trilholte gevuld met olie en geëxciteerd door een laser. Dit geeft een langzame niet-lineariteit. In metingen waarin de resonantiefrequentie van de trilholte met verschillende snelheden wordt gescand over het bereik van bistabiliteit, vinden we dat de oppervlakte van de hysteresislus een niet-monotone functie is van de scansnelheid. In de limiet van een hoge snelheid, waar de scantijd vergelijkbaar is met de geheugentijd van de niet-lineariteit, vinden we dat de hysteresislus in oppervlakte afneemt volgens een universele machtswet met exponent -1 . Daarnaast vinden we tekenen van niet-Markoviaanse dynamica, ontstaan door geheugeneffecten en witte

ruis.

Hoofdstuk 3 toont een serie metingen aan een laser-geëxciteerd metallisch rooster bedekt met een laag olie. Bij voldoende hoog laser vermogen zien we optische bistabiliteit in de transmissie en zelfoscillaties in de -1 en $+1$ diffractieordes door het rooster. Hieronder vallen gebieden met spontane breking van symmetrie, waarbij de intensiteit van de -1 en $+1$ diffractieordes verschillend zijn, ondanks dat het systeem en de excitatie symmetrisch zijn. Tot slot vinden we spontane oscillaties in alle observabelen. Deze laten zich zien als een zaagtand in de transmissie van de laser, en als periodieke pieken in de intensiteiten van de diffractie. Deze verschillende oscillaties zijn allen synchroon met elkaar.

In Hoofdstuk 4 onderzoeken we sterke koppeling tussen licht en materie in een verstembare Fabry-Pérot trilholte met een CsPbBr_3 perovskiet kristal. We vinden in optische metingen spectrale lijnvormen gelijkend aan Fano resonanties en Rabi splitsing (tekenen van een coherente koppeling tussen subsystemen), terwijl het systeem in werkelijkheid geen van beide eigenschappen bezit. We vinden deze effecten in transmissie en fotoluminescentie metingen met objectieven met verschillende numerieke apertuur. Onze metingen tonen aan dat zelfs een relatief klein numeriek apertuur kan resulteren in spectrale artefacten gelijkend op Fano resonanties en Rabi splitsingen. De resultaten in dit hoofdstuk onthullen een mogelijke systematische fout, welke over het hoofd kan zijn gezien in experimenten waarbij dispersieve optische systemen gekarakteriseerd worden door objectieven met hoog numeriek apertuur. Tot slot geven we een algemene richtlijn om deze valkuilen te vermijden bij experimenten met zulke optische systemen.

In Hoofdstuk 5 tonen we onze inspanningen tot het construeren en karakteriseren van een verstembare trilholte in een gesloten-cyclus cryostaat, en om deze opstelling te gebruiken om de niet-lineaire optische response van CsPbBr_3 perovskiet te onderzoeken. We zoomen in op de karakteristiek van de mechanische stabiliteit van de trilholte door de transmissie van een laser te meten. We vinden dat mechanische fluctuaties veroorzaakt door de beweging van de cryostaatpomp de werking van de opstelling sterk beïnvloeden. Desondanks waren we in staat zinvolle experimenten uit te voeren door snelle metingen te doen (zodoende omzeilen we de effecten van de langzame mechanische fluctuaties), of door de cryostaatpomp tijdelijk uit te zetten. Met de eerste methode vinden we een zeer niet-lineaire response van licht in een vlak-holle trilholte met een CsPbBr_3 perovskiet kristal erin. We demonstreren hiermee voor het eerst de observatie van optische bistabiliteit in een systeem van perovskiet.

List of Publications

Related to this thesis:

Z. Geng, K. J. H. Peters, A. A. P. Trichet, K. Malmir, R. Kolkowski, J. M. Smith, and S. R. K. Rodriguez, “Universal Scaling in the Dynamic Hysteresis, and Non-Markovian Dynamics, of a Tunable Optical Cavity”, *Phys. Rev. Lett.* **124**, 153603 (2020) (Chapter 2).

Z. Geng, J. Abad Arredondo, F. Bijloo, G. Keijsers, F. J. García-Vidal, A. I. Fernández-Domínguez, and S. R. K. Rodriguez, “Spontaneous symmetry breaking in the diffracted intensity by a bistable plasmonic grating”, in preparation (Chapter 3).

Z. Geng, J. Theenhaus, B. K. Patra, J. Zheng, J. Busink, E. C. Garnett, S. R. K. Rodriguez, “Fano lineshapes and Rabi splittings: Can they be artificially generated or obscured by the numerical aperture?”, *ACS Photonics* **8**, 1271 (2021) (Chapter 4).

G. Keijsers, K. J. H. Peters, **Z. Geng**, K. Malmir, J. M. Smith and S. R. K. Rodriguez, “Spin multistability and polarization switching in a perovskite semiconductor tunable cavity”, in preparation (Chapter 5).

Other:

K. J. H. Peters, **Z. Geng**, K. Malmir, J. M. Smith, S. R. K. Rodriguez, “Extremely Broadband Stochastic Resonance of Light and Enhanced Energy Harvesting Enabled by Memory Effects in the Nonlinear Response”, *Phys. Rev. Lett.* **126**, 213901 (2021).

G. Keijsers, **Z. Geng**, K. J. H. Peters, M. Wouters, S. R. K. Rodriguez, “Steady-state superfluidity of light in a tunable cavity at room temperature”, Submitted.

